KATHOLIEKE UNIVERSITEIT LEUVEN
FACULTEIT TOEGEPASTE WETENSCHAPPEN
DEPARTEMENT ELEKTROTECHNIEK (ESAT),
AFDELING PSI
Kasteelpark Arenberg 10, 3001 Leuven-Heverlee (Belgium)

FACULTEIT GENEESKUNDE
DEPARTEMENT MORFOLOGIE EN MEDISCHE
BEELDVORMING, AFDELING RADIOLOGIE
Herestraat 49, 3000 Leuven (Belgium)

Iterative Reconstruction for Reduction of Metal Artifacts in Computed Tomography

Promotoren:
Prof. dr. ir. J. Nuyts
Prof. dr. ir. P. Suetens

Proefschrift voorgedragen tot
het behalen van het doctoraat
in de toegepaste wetenschappen
door

Bruno DE MAN

21 mei 2001

KATHOLIEKE UNIVERSITEIT LEUVEN
FACULTEIT TOEGEPASTE WETENSCHAPPEN
DEPARTEMENT ELEKTROTECHNIEK (ESAT),
AFDELING PSI
Kasteelpark Arenberg 10, 3001 Leuven-Heverlee (Belgium)

FACULTEIT GENEESKUNDE
DEPARTEMENT MORFOLOGIE EN MEDISCHE
BEELDVORMING, AFDELING RADIOLOGIE
Herestraat 49, 3000 Leuven (Belgium)

Iterative Reconstruction for Reduction of Metal Artifacts in Computed Tomography

Leden van de jury:
Prof. dr. ir. E. Aernoudt (voorzitter)
Prof. dr. ir. J. Nuyts (promotor)
Prof. dr. ir. P. Suetens (promotor)
Prof. dr. sc. P. Dupont (assessor)
Prof. dr. ir. S. Van Huffel (assessor)
Prof. dr. G. Marchal
Prof. dr. ir. D. Van Dyck
(Universiteit Antwerpen)
Prof. dr. ir. M. Wevers

Proefschrift voorgedragen tot
het behalen van het doctoraat
in de toegepaste wetenschappen
door

Bruno DE MAN

U.D.C. 615.849

21 mei 2001

ISBN 90-5682-300-0
D/2001/7515/12

"The true logic of this world

is in the calculus of probabilities"

James Clerk Maxwell

Acknowledgements

I started doing research on iterative reconstruction and CT in February 1997. I had the feeling that I had a long, long journey to go. I knew that it wouldn't be easy, and that lots of coffee and CPU would have to be spent. Now, I am proud to be at the end of this journey. 51 months have flown by. This journey would have been impossible without all the help and support I received. Hence this word of thanks.

First of all, I would like to thank my promoters *prof. Paul Suetens* and *prof. Johan Nuyts*. Paul is the one who invited me to join his laboratory for medical image computing in August 1995. He gave me the opportunity to make a Ph.D. as his assistant, and he always believed in my potentials. He offered me the chance to attend courses, to teach, to write a book chapter, and to do many other things that made my work so much more diversified. Johan is undoubtedly the person that contributed most to this work. He initiated me in the worlds of IDL and iterative reconstruction. Many ideas contained in this thesis originate from his scientific brain. Whenever I got stuck, he pulled me back onto the right trail. He was more than a promoter should be. He helped me day after day. He was really a friend.

Secondly, I thank my assessors *prof. Patrick Dupont* and *prof. Sabine Van Huffel*. Patrick, a physicist in heart and soul, followed my work fairly closely. His constructive criticism was always pertinent. I thank prof. Van Huffel, a highly-esteemed scientist in the interface between medicine and engineering, for her kind cooperation. I am grateful that she found the time to give her valuable feedback on this thesis.

I would also like to thank all members of the *jury* for their interest in this thesis. In particular, I would like to thank *prof. Guy Marchal*, head of the department of radiology and of the laboratory for medical image computing, for putting his trust in me by allowing me to use the CT-scanners.

Special thanks goes to the people from Siemens Medical Systems: *Dr. Dietmar Hentschel, Dr. Klaus Klingenbeck-Regn, Dr. Stefan Schaller, Dr. Thomas Flohr, Dr. Karl Stierstorfer, Dr. Ernst Klotz, Dr. Martin Petersilka*, ... Without their information on CT-scanners, it would have been impossible to make this Ph.D. on CT reconstruction.

I thank the *Flemish Fund for Scientific Research* (FWO) for their financial support (grant number G.0106.98).

I owe many thanks to the staff of the department of radiology. *Raf Crick* and *Antoine Moens* helped me to uncover the mysteries behind the CT-scanners. *Willy Reviers* and *Guido Putseys* arranged a CT scanner for me whenever I needed one.

Frans Decock, Filip Vervloesem, Patrick Lievens, and all other CT-scanner operators were always willing to discuss CT questions and to help with my experiments. I could always count on the secretaries of the department of radiology and on the logistical support from *Guido Vansteenkiste*, who brings a ray of sunshine wherever he comes.

I am grateful to *Dr. Els Tijskens* and to the people from *biotechniek* for the production of the plexiglas phantoms, to *prof. A. Verbruggen* and *prof. G. Bormans* from the laboratory for radiopharmaceutical chemistry for their logistical support for the spectrum measurements, and to *Marc Gay* for the cartoons at the beginning of each chapter.

I also want to express my appreciation to the work of *Annitta De Messemaeker* and *Patricia Waege*, who have been indispensable at many occasions.

I want to thank in particular ALL my direct colleagues and ex-colleagues. Instead of giving an exhaustive list, which risks to be incomplete, I prefer to randomly quote a few of their names. Thank you to *Bart Bijnens* and *Jan D'hooge* for their team spirit during my research in echocardiography. Thank you to all *system managers*, for trying to keep the computer network running. Thank you to *Dominique Delaere* for his strong commitment to our group. Thank you to *Johan Michiels* and *Alex Maes*, our enthusiastic football-coaches. Thank you to my "buddies" *Jan D'hooge* and *Gert Behiels*, who shared my passion for windsurfing as well as some other non-professional activities. Thank you to *Koen Van Leemput* for his solidarity while also finishing his thesis. For a complete list of colleagues, I refer to our web-site "www.medicalimagecomputing.com", and even then, I would miss some of my colleagues from nuclear medicine, cardiology, radiology, radiopharmacy, geology, building physics, ESAT, ...

Vervolgens wil ik ook heel mijn familie bedanken. Oneindig veel dank aan mijn ouders. Zij boden mij een toffe thuis en een opvoeding waarvan ik hoop dat ik ze ook aan mijn kinderen kan bieden. Zij gaven mij de kans om te studeren en om maar te blijven studeren. Ik beschouw dit doctoraat als de kroon op mijn studies, die ik aan hen te danken heb. Niet minder dank gaat naar mijn broers en zussen, die mijn opvoeding niet alleen meegemaakt maar ook mee gemaakt hebben. Ik herinner me hoe mijn zussen hun veel jongere broertje schertsend om uitleg vroegen als ze een probleem hadden met een kursus. Alsof het gisteren was – ik moet een jaar of tien geweest zijn – herinner ik me Filip's uitleg dat alle dingen, ja zelfs de gordijnen (!), eigenlijk uit minnetjes en plusjes bestaan. Of hoe Benny me overtuigde om het humaniora-boekje van biologie in te ruilen voor zijn kursus gynaecologie. Door het opwekken van mijn wetenschappelijke interesse hebben zij allen een niet te onderschatten bijdrage geleverd aan dit doctoraat. Dank ook aan mijn schoonouders, schoonbroers en -zussen, neefjes en nichtjes. Geen van hen zou ik willen missen in mijn grote familie, die steeds een enorme steun betekend heeft.

Mijn laatste woorden van dank gaan naar jou, Akke. Dank om met mij in zee en overzee te willen gaan. Dank voor je dagelijkse inzet. Dank voor Ruben, de mooiste zoon die ik mij kon inbeelden, en voor het prachtige gezin dat we samen aan het maken zijn. Jullie gaven mij dagelijks de moed en de wil om dit werk tot een goed einde te brengen. Dank uit het diepst van mijn hart!

Bruno

Abstracts

Iterative reconstruction for reduction of metal artifacts in computed tomography

Metal artifacts are a major problem in computed tomography (CT). They are due to the presence of strongly attenuating objects in the scanning plane. Based on simulations and measurements, the most important causes of metal artifacts were determined: noise, beam hardening, the non-linear partial volume effect, and scatter. In order to develop new algorithms for reduction of metal artifacts, we hypothesize that artifacts are due to deviations of the acquisition model assumed by the reconstruction from the true acquisition process. Consequently, improving the acquisition model should reduce artifacts. We developed algorithms modeling noise, beam hardening, and the non-linear partial volume effect. Excellent results were obtained. The scatter model requires further research. All algorithms were combined resulting in one global approach for reduction of metal artifacts.

Iteratieve reconstructie voor reductie van metaalartefacten in computertomografie

Metaalartefacten vormen een belangrijk probleem in computertomografie (CT). Ze zijn het gevolg van de aanwezigheid van sterk attenuerende objecten in het gescande vlak. Aan de hand van simulaties en metingen werden de belangrijkste oorzaken van metaalartefacten bepaald: ruis, beam hardening, het niet-lineair partieel-volume effect en scatter. Voor de ontwikkeling van nieuwe algoritmes ter reductie van metaalartefacten vertrekken we van de hypothese dat artefacten het gevolg zijn van afwijkingen van het acquisitie-model gebruikt in de reconstructie ten opzichte van de werkelijke acquisitie. Bijgevolg moet een verbeterd acquisitie-model resulteren in verminderde artefacten. We ontwikkelden algoritmes met modellen voor ruis, beam hardening, en het niet-lineair partieel-volume effect. Uitstekende resultaten werden bekomen. Het model voor scatter vereist verder onderzoek. Alle modellen werden samengebracht resulterend in één globaal algoritme voor reductie van metaalartefacten.

Iteratieve Reconstructie voor Reductie van Metaalartefacten in Computertomografie

Computertomografie

De ontdekking van X-stralen door Wilhelm Conrad Röntgen in 1895 luidde een nieuw tijdperk in voor de geneeskunde: dit was het begin van de medische beeldvorming. Röntgen had aangetoond dat het mogelijk is om het skelet in beeld te brengen door de hand van zijn echtgenote te bestralen. Tot op heden blijft radiografie één van de belangrijkste medische beeldvormingsmodaliteiten. Inmiddels zijn een aantal nieuwere modaliteiten uitgevonden. In echografie gebruikt men ultrasone golven om de akoestische eigenschappen van het lichaam in beeld te brengen. In nucleaire geneeskunde wordt een radio-actieve stof ingespoten, en detecteert men de gamma-stralen uitgezonden binnenin het menselijk lichaam. In MRI gebruikt men magnetische pulsen om de verdeling van magnetische spins in het menselijk lichaam te bepalen. Computertomografie (CT) is gebaseerd op hetzelfde fysische principe als radiografie. Gebruikmakend van een externe Röntgen-buis meet men de attenuatie van X-stralen door weefsel. In tegenstelling tot radiografie laat CT toe om de attenuatie op iedere plaats in het lichaam afzonderlijk te bepalen. In radiografie wordt een volledig volume geprojecteerd op één beeld, en iedere pixel stelt de integraal van de attenuatie langs de overeenkomstige scan-lijn voor. In CT zorgt een reconstructie-algoritme ervoor dat men virtuele sneden van het menselijk lichaam kan maken.

Gefilterde terugprojectie

Kort na de uitvinding van de CT-scanner door Godfrey N. Hounsfield in 1972 [62] werd reconstructie op basis van gefilterde terugprojectie (FBP) – ontwikkeld

voor astrofysische toepassingen [4] – ingevoerd. Tot op heden blijft FBP veruit het meest gebruikte reconstructie-algoritme in CT. FBP is een zogenaamde transformatie-methode: ze gaat uit van de veronderstelling dat de metingen de Radon-transformatie [120] vormen van de verdeling van de lineaire attenuatiecoëfficiënt die men wenst te reconstrueren. Analytische inversie van de Radon transformatie geeft een directe oplossing voor het probleem. Toegepast op ideale projecties – d.w.z. een oneindig aantal metingen met een oneindig dunne bundelbreedte, zonder ruis, enz. – is deze oplossing ook de ideale oplossing.

Jammer genoeg is dit slechts bij benadering het geval. Ten eerste: een meting bestaat uit een eindig aantal waarden gemeten met een X-stralen-bundel met eindige breedte en gemeten over een eindig rotatie-interval. In de praktijk wordt FBP gediscretiseerd om toe te laten een discreet beeld te berekenen uit een eindig aantal projectie-metingen. Ten tweede: een Röntgen-buis zendt een continu spectrum uit, hetgeen resulteert in het fenomeen 'beam hardening'. Ten derde: de metingen zijn onderhevig aan ruis en strooistraling (scatter). Er zijn nog talrijke andere mogelijke verschilpunten tussen de Radon-transformatie en de eigenlijke data-acquisitie. Al deze effecten resulteren in artefacten[1] in de gereconstrueerde beelden. Gewoonlijk zijn de fouten door deze benaderingen relatief klein en levert FBP bevredigende resultaten. Maar onder extreme omstandigheden, bv. in de aanwezigheid van metalen, wordt de amplitude van de artefacten onaanvaardbaar en de corresponderende beelden onbruikbaar.

Indien men gebruikmaakt van FBP, worden artefacten gereduceerd door eerst de data te corrigeren en daarna FBP toe te passen (of omgekeerd). Ruis en aliasing worden meestal onderdrukt door een laagdoorlaatfilter toe te passen op de metingen. Scatter en beam hardening worden gecompenseerd door de overeenkomstige fout af te trekken van de metingen. Er bestaan ook een aantal algoritmes voor reductie van metaalartefacten. Metingen doorheen de metalen objecten worden hierin ofwel genegeerd ofwel vervangen door interpolatie tussen aanliggende metingen. Deze algoritmes resulteren in een sterke reductie van metaalartefacten, maar ze veroorzaken bepaalde nieuwe artefacten. Er heerst dus een grote vraag naar betere algoritmes voor reductie van metaalartefacten.

Iteratieve Reconstructie

Iteratieve reconstructie laat toe om expliciet rekening te houden met de ruiskarakteristieken van de meting en om het acquisitie-model uit te breiden bv. met een model voor scatter, een model voor beam hardening, enz. Men vertrekt meestal van een discrete voorstelling van reconstructie en metingen. Een beeld wordt voorgesteld door een set pixel-waarden $\{\mu_j\}_{j=1}^{J}$ genoteerd als vector $\vec{\mu}$, de metingen door de data-set $\{y_i\}_{i=1}^{I}$, sinogram genaamd. Op basis van deze voorstelling kan een discreet voorwaarts model van de acquisitie worden opgesteld. Gegeven een beeld $\vec{\mu}$,

[1] Een artefact is een kunstmatige verandering van uitzicht.

kan de verwachte waarde voor transmissie-meting i geschreven worden als

$$\hat{y}_i = b_i \cdot \exp(-\sum_{j=1}^{J} l_{ij}\mu_j), \tag{0.1}$$

waarbij b_i het aantal fotonen is dat gemeten zou worden zonder patiënt of object, en l_{ij} de effectieve weglengte van straal i doorheen pixel j.

Vervolgens wordt een criterium of kostfunctie gedefinieerd en probeert men een beeld te vinden dat zo goed mogelijk beantwoordt aan dit criterium. Een voorbeeld van zo een criterium is de maximum-likelihood benadering: zoek het meest waarschijnlijke beeld, gegeven de metingen. Naast een criterium, moet men ook een methode definiëren om dit criterium te optimaliseren, zoals bv. de methode van de steilste helling. Meestal resulteert dit in een iteratief schema zoals in figuur 4.1. Vertrekkende van een initiële schatting van het beeld wordt een sinogram berekend. Dit wordt vergeleken met het gemeten sinogram, een maat voor de fout wordt getransformeerd naar het beeld-domein, en het beeld wordt overeenkomstig aangepast. Vervolgens wordt opnieuw een sinogram berekend, vergeleken met het gemeten sinogram, enzovoort, totdat een goede reconstructie bekomen is.

Een gelijkaardige benadering is de maximum a posteriori (MAP) benadering. Hier wordt naast de meting (ML) ook de a-priori waarschijnlijkheid van een bepaalde verdeling $\vec{\mu}$ in rekening gebracht. Door gebruik te maken van Markov random velden en een Gibbs-prior kan men bv. eisen dat naburige pixels ook gelijkaardige attenuatie hebben, hetgeen ruis en andere artefacten onderdrukt.

Het grootste nadeel van iteratieve reconstructie is de lange rekentijd. Een mogelijke manier om de rekentijd te verlagen is de methode van ordered subsets. Elke iteratie wordt opgedeeld in een aantal sub-iteraties die telkens slechts een subset van alle metingen gebruiken. Indien deze subsets representatief gekozen worden, resulteert dit in een zeer sterke vermindering van de rekentijd.

ML-TR

In deze thesis gaan we uit van het ML-TR algoritme (maximum likelihood voor transmissie). Door de ML benadering toe te passen op CT (m.a.w. op transmissiemetingen) en uitgaande van een Poisson ruis-model, kan de volgende update-stap berekend worden:

$$\mu_j^{n+1} = \mu_j^n + \frac{\sum_{i=1}^{I} l_{ij} \cdot (\hat{y}_i - y_i)}{\sum_{i=1}^{I} l_{ij} \cdot \left[\sum_{h=1}^{J} l_{ih}\right] \cdot \hat{y}_i}. \tag{0.2}$$

De noemer bestaat uit de terugprojectie van het verschil tussen het berekende en het gemeten sinogram (zie figuur 4.1). De teller bevat de terugprojectie van het produkt van het berekende sinogram en de projectie van een beeld dat gelijk is aan 1 binnen de FOV en 0 elders. Het gebruikte acquisitie model kan eenvoudig

uitgebreid worden, bijvoorbeeld met een geschatte scatter-term S_i:

$$\hat{y}_i = b_i \cdot \exp(-\sum_{j=1}^{J} l_{ij}\mu_j) + S_i. \tag{0.3}$$

We willen in de eerste plaats onderzoeken of het mogelijk is bepaalde artefacten (en metaalartefacten in het bijzonder) te reduceren door het gebruikte acquisitiemodel te verbeteren. In een initiële studie werden verschillende reconstructiemethodes toegepast op spiraal-CT en op 2D-CT met en zonder sterk attenuerende objecten. Voor de iteratieve algoritmes werd het voorwaartse model uitgebreid naar spiraal-CT, rekening houdend met het helicoïdale traject van de Röntgen-buis. Het aantal vrijheidsgraden werd beperkt door gebruik te maken van Gaussiaanse axiale basisfuncties. Dit werd vergeleken met de klassieke methodes waarbij eerst een 2D data-set wordt geïnterpoleerd en vervolgens FBP toegepast. Uit deze studie bleek dat de gebruikte axiale basisfuncties leiden tot ontoelaatbare Gibbs-overshoots aan sterke axiale gradiënten. Mogelijk bieden niet-lineaire constraints zoals Gibbs-priors een betere oplossing. In de aanwezigheid van sterk attenuerende objecten resulteerden de iteratieve algoritmes in aanzienlijk verminderde artefacten. Dit vormde de aanleiding om het probleem van metaalartefacten meer in detail te onderzoeken.

Doelstellingen

Het doel van deze thesis is het probleem van metaalartefacten op fundamentele wijze te onderzoeken. Eerst willen we de belangrijkste oorzaken van metaalartefacten bepalen. Hiertoe ontwikkelden we een CT-simulator (hoofdstuk 3) en voerden we een aantal simulaties en metingen uit. Vervolgens willen we metaalartefacten reduceren (hoofdstuk 5), gebruik makende van iteratieve reconstructie (hoofdstuk 4) en door rekening te houden met die belangrijkste oorzaken van metaalartefacten.

Simulator

De simulator is bedoeld om zo nauwkeurig mogelijk een echte CT-scanner na te bootsen. De eindige breedte van de X-stralen-bundel wordt gesimuleerd door de focus op de Röntgen-buis en de detector-elementen te bemonsteren aan hoge resolutie. Ook de continue rotatie wordt in rekening gehouden door te bemonsteren aan hoge resolutie. Het continue spectrum van de Röntgen-buis wordt gemodelleerd door een aantal monochromatische simulaties op te tellen. Software-fantomen worden gedefinieerd als een superpositie van een aantal elementaire deelobjecten, elk met een eigen vorm, grootte, positie, resolutie en compositie. De simulator is beperkt tot een 2D fanbeam geometrie en gebruikt een sterk vereenvoudigde scattersimulatie. Validatie gebeurde op basis van metingen van de PSF van de acquisitie en op basis van fantoom-metingen. Zeer realistische simulaties zijn mogelijk, aangepast aan verschillende types CT-scanners. Zo wordt de simulator bv. ook gebruikt in andere onderzoeksgroepen voor het simuleren van micro-CT-scanners [12].

Oorzaken van metaalartefacten

In de literatuur vindt men vele mogelijke oorzaken van artefacten: ruis [34], beam hardening [33, 34, 72, 74, 100, 124], trans-axiaal niet-lineair partieel-volume (NLPV) effect [75], axiaal NLPV-effect [45], scatter [43, 76], beweging [46], te weinig detector-elementen [77] en te weinig views [73]. Om na te gaan welke van deze oorzaken van artefacten het meest relevant zijn voor metaalartefacten werden een aantal metingen en experimenten gedaan. Het grote voordeel van een CT-simulator is de mogelijkheid om bepaalde eigenschappen te veranderen die in een echte scanner moeilijk of onmogelijk te veranderen zijn. Meer in het bijzonder kan men alle mogelijke oorzaken van artefacten afzonderlijk aan- of afzetten om te kijken hoe de bijhorende artefacten eruitzien en wat hun belang is. We kwamen tot de bevinding dat de belangrijkste oorzaken van metaalartefacten de volgende zijn: ruis, beam hardening, het NLPV-effect en scatter.

Reductie van metaalartefacten: bestaande methodes

In de literatuur vindt men veel verschillende methodes voor reductie van metaalartefacten. De meest voordehandliggende oplossing is metaalartefacten te voorkomen door gebruik te maken van minder-attenuerende materialen (bv. titaan) of metalen objecten met een kleinere doorsnede [50, 126, 147]. Een tweede mogelijkheid is de acquisitie aan te passen. Ruis kan men reduceren door meer straling te gebruiken. Beam hardening kan men verminderen door de X-stralen-bundel hardware-matig te filteren om een smaller spectrum te bekomen. Haramati [50] toonde aan dat een hogere nominale bron-spanning geen substantiële artefactreductie oplevert. Het NLPV-effect kan men verminderen door smallere X-stralen-bundels te gebruiken. Aliasing artefacten kan men verminderen door een groter aantal detector-elementen en een groter aantal views te gebruiken. Jammer genoeg zijn al deze oplossingen in tegenstrijd met een aantal beperkingen zoals patiënt-dosis, levensduur van de bron, kostprijs, ... Robertson [125, 126] toonde aan dat het herberekenen van beelden in vlakken loodrecht of schuin op het scan-vlak een betere visualisatie van bot oplevert in aanwezigheid van metalen implantaten. Henrich [53] paste na reconstructie een beeldverbeteringsalgoritme toe om streaks te verwijderen. De meest succesvolle methodes bestaan evenwel uit een aangepast reconstructie-algoritme. Hierbij worden metalen voorwerpen gewoonlijk als ondoorlatend beschouwd, en metingen overeenkomend met scan-lijnen doorheen het metaal worden beschouwd als 'ontbrekend'. Deze methodes kan men onderverdelen in twee groepen:

- projectie-vervolledigingsmethodes: de ontbrekende metingen worden vervangen door waarden berekend op basis van naburige metingen, hetzij door lineaire of hogere-orde interpolatie [46, 61, 82, 91, 96, 101, 134, 135, 146], hetzij door patroonherkenning [102], hetzij m.b.v. lineaire-predictie methodes [121]. De meeste van deze methodes passen vooraf beam hardening correctie toe.
- iteratieve methodes: bestaande iteratieve algoritmes worden aangepast zodat ze de ontbrekende data negeren [117, 127, 148].

Reductie van metaalartefacten: bijdrage van dit werk

Wij vertrekken van de hypothese dat artefacten het gevolg zijn van de afwijkingen van het wiskundig acquisitie-model waar het reconstructie-algoritme op gebaseerd is, t.o.v. het werkelijke acquisitie-model. Indien men het wiskundig acquisitie-model verbetert, moeten bijgevolg ook de artefacten gereduceerd worden. De bedoeling is dus om – vertrekkende van ML-TR, waarvan we weten dat het een Poisson ruis-model omvat – algoritmes te ontwikkelen die een even goede beeldkwaliteit geven als FBP maar met gereduceerde metaalartefacten.

1. Eerst werd een MAP-algoritme ontwikkeld [25]. Door gebruik te maken van een Poisson ruis-model proberen we de ruis-artefacten te beperken. Dit ruis-model maakt het algoritme ook robuust tegen andere oorzaken van artefacten. Indien langs bepaalde scan-lijnen alle (of bijna alle) fotonen geabsorbeerd worden, zijn de projectiemetingen onvolledig. We voerden een Markov random veld Gibbs-prior in om deze ontbrekende informatie te compenseren. Daarnaast werd een verhoogd aantal reconstructie-pixels gebruikt om het aantal vrijheidsgraden op te drijven. Goede resultaten werden bekomen voor simulaties en metingen. Artefacten worden gereduceerd en kleine details blijven behouden. Dit MAP-algoritme werd vergeleken met de projectie-vervolledigingsmethode, en met iteratieve methodes die de 'ontbrekende' metingen negeren.

2. Vervolgens werd het acquisitie-model uitgebreid rekening houdend met het de polychromaticiteit van het spectrum, voor reductie van beam hardening artefacten [26]. Dit resulteerde in een nieuw iteratief maximum-likelihood polychromatisch algoritme voor CT (IMPACT). Uitstekende resultaten werden bekomen voor simulaties en metingen. Dit algoritme werd vergeleken met de bestaande post-reconstructie benadering, en de graad van artefact-reductie was vergelijkbaar voor beide algoritmes. In aanwezigheid van metalen voorwerpen scoort IMPACT duidelijk beter, dankzij het nauwkeurige ruis-model.

3. Er werden drie algoritmes ontwikkeld voor reductie van het NLPV-effect [27], rekening houdend zowel met de eindige rotatie-intervallen als met de grootte van de focus en de detector-elementen. De eerste methode bestaat uit een pre-correctie toegepast op de metingen, gecombineerd met bv. FBP. De twee andere methodes zijn uitbreidingen van ML-TR door het acquisitie-model aan te passen aan de eindige rotatie-intervallen en de eindige bundel-breedte. Goede resultaten werden bekomen voor simulaties en een meting. De drie methodes resulteren in een substantiële artefact-reductie. In aanwezigheid van metalen voorwerpen, zijn de iteratieve algoritmes weerom superieur.

4. Tenslotte leidden we een globaal algoritme af, waarin alle belangrijke oorzaken van metaalartefacten samen gemodelleerd worden. Alle voorgaande algoritmes worden herleid tot speciale gevallen van dit globale algoritme.

Suggesties voor verder onderzoek

Van de vier belangrijke oorzaken van metaalartefacten hebben we er drie grondig onderzocht: ruis, beam hardening en het NLPV-effect. Scatter, de vierde belangrijke oorzaak, vereist verder onderzoek. Een mogelijke aanpak bestaat erin de scatterbijdrage te schatten gebruik makende van een vereenvoudigde scatter-simulator. Deze schatting kan dan als input dienen van een iteratief algoritme dat een gekende scatter-term modelleert.

In deze thesis beperkten we ons tot 2D-simulaties en 2D-reconstructie-algoritmes. In een werkelijke CT-scanner mag men de derde dimensie niet zomaar verwaarlozen:

1. De eindige snede-dikte is essentieel voor het axiaal NLPV-effect. Correctie van het axiaal NLPV-effect vereist dan ook 3D iteratieve reconstructie, hetgeen resulteert in lange rekentijden. Anderzijds kan men het NLPV-effect ook beperken door een zo klein mogelijke snede-collimatie te gebruiken.

2. In spiraal-CT volgt de Röntgen-buis een helicoïdaal traject t.o.v. de patiënt. In de praktijk wordt een 3D-dataset herrekend tot een reeks 2D-datasets m.b.v. interpolatie. Een andere mogelijkheid bestaat erin iteratieve recontructie toe te passen uitgaande van een 3D-model van de acquisitie (sectie 4.9). Met de komst van multi-slice CT is de longitudinale resolutie echter niet langer een probleem.

3. De CT-scanner technologie evolueert zeer snel: binnen enkele jaren mag men reeds commerciële cone-beam CT-scanners op de markt verwachten. Er wordt momenteel veel onderzoek gedaan naar cone-beam reconstructie. Ook hier is 3D iteratieve reconstructie een mogelijke optie.

Op basis van voorgaande argumenten mag men concluderen dat zowel 3D als 2D iteratieve reconstructie mogelijke toepassingen hebben. In beide gevallen zijn de resultaten van deze thesis toepasbaar. Ruis, beam hardening, het NLPV-effect en scatter zijn immers inherente fysische verschijnselen die gelden voor alle types CT-scanners. In geval van 2D reconstructie kan men de algoritmes rechtstreeks toepassen. In geval van 3D reconstructie kunnen de algoritmes uitgebreid worden naar 3D.

Zodra het onderzoek naar scatter voltooid is, kan het globaal algoritme geïmplementeerd en gevalideerd worden. Eén aspect dat verdere aandacht zal vereisen is het bepalen van de prior parameters (gewicht, type, ...) die de beste resultaten geven. Voor toepassing in de klinische praktijk is nog een sterke vermindering van de rekentijd vereist. We hebben steeds gepoogd alle vraagstukken op een fundamentele manier op te lossen, veeleer dan ons te bekommeren om lange rekentijden. Alle in dit werk voorgestelde methodes zijn essentieel aanpassingen van de gebruikte kostfunctie, terwijl we ons steeds beperkt hebben tot één en dezelfde optimalisatie-stap. We zijn er van overtuigd dat andere optimalisatie-methodes, bijkomende versnellingsmethodes, meer efficiënt programmeren, snellere computers en hardware implementatie zullen toelaten om maximum-likelihood iteratieve reconstructie daadwerkelijk te gebruiken in CT. We hopen dat de voorgestelde aanpak zal resulteren in een reductie van metaalartefacten die veel beter is dan wat tot op heden mogelijk is.

Acronyms

1D 1-dimensional
2D 2-dimensional
3D 3-dimensional
ART ..... algebraic reconstruction technique
COR ..... center of rotation
CPU ..... central processing unit
CT ..... computed tomography
EEGE ..... exponential edge-gradient effect
EBT ..... electron-beam tomography
ECG ..... electrocardiogram
EM ..... expectation maximization
ERF ..... edge response function
FBP ..... filtered backprojection
FOV ..... (diameter of the) field of view
FWHM ..... full width at half maximum
FT ..... Fourier transformation
HU ..... Hounsfield units
IBHC ..... iterative beam hardening correction
ILIN180 ..... iterated 180° linear interpolation FBP
IMPACT ..... iterative maximum likelihood polychromatic algorithm for CT
LIN180 ..... 180° linear interpolation FBP
MAP ..... maximum a posteriori
MAR ..... metal artifact reduction
MART ..... multiplicative ART
ML ..... maximum likelihood
ML-TR ..... maximum likelihood algorithm for transmission tomography

MRF ..... Markov random field
MRI ..... magnetic resonance imaging
NLPV ..... non-linear partial volume
NN180 ..... 180° nearest neighbour FBP
OS ..... ordered subsets
PET ..... positron emission tomography
PMT ..... photo-multiplier tube
PSF ..... point spread function
ROI ..... region of interest
SNR ..... signal-to-noise ratio
SPECT ..... single photon emission computed tomography
*t*NLPV ..... trans-axial non-linear partial volume
TR ..... transmission tomography

Symbols

$\otimes$	convolution
α, β	fan-beam coordinate system (section 2.5.5). β is the angle between the center line of a fan and the y-axis. α is the angle between a particular ray and the center line
b_i	blank scan, this is the detected number of photons in sinogram pixel i in the absence of absorber
E	photon energy [keV]
$\mathcal{F}$	Fourier transform
$f(x, y)$	generical 2D function
$F(k_x, k_y)$	2D Fourier transform of f(x,y)
I	intensity of an X-ray beam, this is either the energy detected per unit time per unit area, or the number of photons detected per detector element.
I_0	intensity of an X-ray beam detected in the absence of absorber
k	energy index
K	total number of modeled energies
L	objective function, usually the log-likelihood function (chapter 4)
l_{ij}	effective intersection length [cm] between projection line i and pixel j
$L_{r,\theta}$	projection line at distance r from the origin making an angle θ with the y-axis
μ	the linear attenuation coefficient [cm^{-1}]
p_i	projection value in sinogram pixel i, obtained by log-converting the measured intensity. Ideally p_i equals the integral of the linear attenuation coefficient along projection line i

$P(k, \theta)$	1D Fourier transform of $p(r, \theta)$ w.r.t. r
r, θ	parallel beam coordinate system (section 2.4), or polar coordinates corresponding to Cartesian coordinates x and y
r, s	coordinate system obtained by rotating x, y over an angle θ (section 2.4)
ρ	mass density [g/cm^3]
S_i	scatter contribution in sinogram pixel i
σ	standard deviation
x, y, z	Cartesian coordinate system. z is the longitudinal axis (in craniocaudal direction). x, y is the trans-axial coordinate system (in the scanning plane)
y_i	measured number of photons in sinogram pixel i
$\hat{y}_i$	expected (or calculated) number of photons in sinogram pixel i

Phantoms

The following table gives an overview of all phantoms used in this thesis. It contains the following information:

- phantom number (nr)
- phantom type: hardware (H) or software (S)
- description
- number of the section where the phantom is defined (s)
- section in which the phantom is used
- page number where the phantom is defined (p)

nr	H/S	description	s	section	p
1	H+S	water bowl with iron rod	3.3.2	simulator	41
2	H+S	plexiglas plate with 1, 2, or 3 amalgam fillings	3.3.2	simulator	41
3	S	clinical 2D CT image of the thorax	4.9.3	spiral CT study	68
4	S	elliptical cylinder containing a smaller circular cylinder	4.9.3	spiral CT study	68
5	S	elliptical cylinder containing multiple ellipsoids	4.9.3	spiral CT study	68
6	S	clinical 2D CT image of the thorax with a small region of high attenuation	4.9.3	spiral CT study	68

7	S	circular plexiglas plate containing 12 line-shaped objects and 3 amalgam inserts	5.2.2	MAP algorithm	81
8	H	circular plexiglas plate containing line-shaped objects and (optionally) 3 amalgam inserts	5.2.3	MAP algorithm	82
9	S	circular water phantom	5.3.4.1	IMPACT	96
10	S	circular water phantom with 4 bone inserts	5.3.4.1	IMPACT	96
11	S	circular water phantom with 8 circular regions of fat, aluminum, plexiglas, lung, brain, bone, blood, and soft tissue	5.3.4.1	IMPACT	96
12	S	circular water phantom with 2 bone inserts and 2 iron inserts	5.3.4.1	IMPACT	96
13	H	circular plexiglas plate containing 4 aluminum cylinders	5.3.4.2	IMPACT	97
14	H	circular plexiglas plate containing 2 aluminum cylinders and 2 iron cylinders	5.3.4.2	IMPACT	97
15	H	human skull, filled and surrounded with plexiglas	5.3.4.2	IMPACT	97
16	S	bone triangle surrounded with a number of circular details	5.4.2	tNLPV effect	110
17	S	inverse of phantom 16, obtained by subtracting phantom 16 from a circular bone object	5.4.2	tNLPV effect	110
18	S	circular water phantom containing two iron inserts, two circular bone inserts, a fat tissue region, and a plexiglas region	5.4.2	tNLPV effect	110
19	H+S	square plexiglas plate of 3 cm $\times$ 3 cm	5.4.3	tNLPV effect	112

Contents


Dr. De Man
WELKOM
MARC GAY

Chapter 1

General introduction

1.1 Computed tomography

The discovery of X-rays by Wilhelm Conrad Röntgen in 1895 heralded a new era in medicine: medical imaging was born. Röntgen had shown that bones could be visualized, by X-raying his wife's hand. Until today, radiography remains one of the basic medical imaging modalities. Meanwhile, a number of other imaging modalities have been invented. In echography, ultrasonic waves are used to image the acoustic properties of the body. Nuclear medicine (gamma-camera, single photon emission computed tomography (SPECT), positron emission tomography (PET)) is based on the measurement of gamma-rays that are emitted inside the human body. This allows to image specific functional properties (such as glucose uptake) of the body. Magnetic resonance imaging (MRI) uses magnetic pulses to image the distribution of magnetic spins inside the body. X-ray computed tomography (CT) is based on the same physical principles as radiography. It uses an external X-ray source and images the X-ray attenuation properties of the body. Unlike radiography, CT allows to image thin slices of the human body. Whereas in radiography the attenuation values along the path of each X-ray beam are superimposed resulting in line-integrals of the attenuation, CT uses reconstruction algorithms to reconstruct the value in each voxel separately, resulting in a 3D dataset. CT is described in chapter 2.

1.2 Filtered backprojection and artifacts in CT

Soon after the invention of CT [62] in 1972, reconstruction by filtered backprojection (FBP), originally developed for astrophysical applications [4], was introduced. Until today, FBP remains the most widely used reconstruction method in CT. FBP is a so-called transform method: it is based on the assumption that the measurements are the Radon transform [120] of the distribution of the linear attenuation coefficient to be recovered. Analytical inversion of the Radon transform gives a

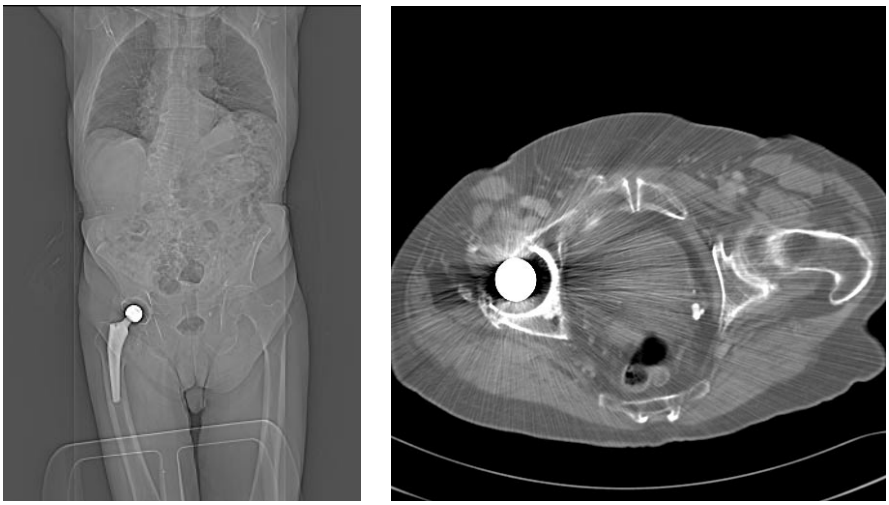

(a) (b)

Figure 1.1: *CT scan of a patient with a hip prosthesis: (a) topogram or scout view, obtained by translating the patient table while keeping the X-ray tube fixed, (b) CT image of a slice through the prosthesis showing severe metal artifacts (courtesy of prof. G. Marchal).*

direct solution to the reconstruction problem. If applied to ideal projections – this means an infinite number of measurements with infinitely thin X-ray beams, without noise, etc. – then this solution equals the ideal solution. Unfortunately, this is only approximately the case. Firstly, the measurements consist of a finite number of detector read-outs using a finite beam-width and measured over a finite rotation interval. Secondly, an X-ray tube emits a continuous spectrum resulting in a phenomenon called beam hardening. Thirdly, the measurements are noisy and include scattered radiation. Many other possible discrepancies exist between the actual measurements and the Radon transform. All these effects result in artifacts[1] in the reconstructed images. Usually, the errors due to these approximations are relatively small, and FBP gives satisfactory results. However, under extreme circumstances, for instance in the presence of highly attenuating objects, artifacts become inadmissibly strong. Figure 1.1 and figure 1.2 show examples of metal artifacts. Clearly, these artifacts make the CT images unusable.

If FBP is used, artifacts are reduced by applying corrections before (or after) applying FBP. Noise and aliasing artifacts are reduced by applying a low-pass filter to the raw data. Scatter and beam hardening are compensated by subtracting their estimated effect from the raw data. A number of dedicated algorithms for metal artifact reduction exist. The measurements through the metal objects are either ignored or replaced by interpolation between adjacent measurements. These existing algorithms allow a strong reduction of metal artifacts, but they introduce

[1] An artifact is an artificially produced change in appearance.

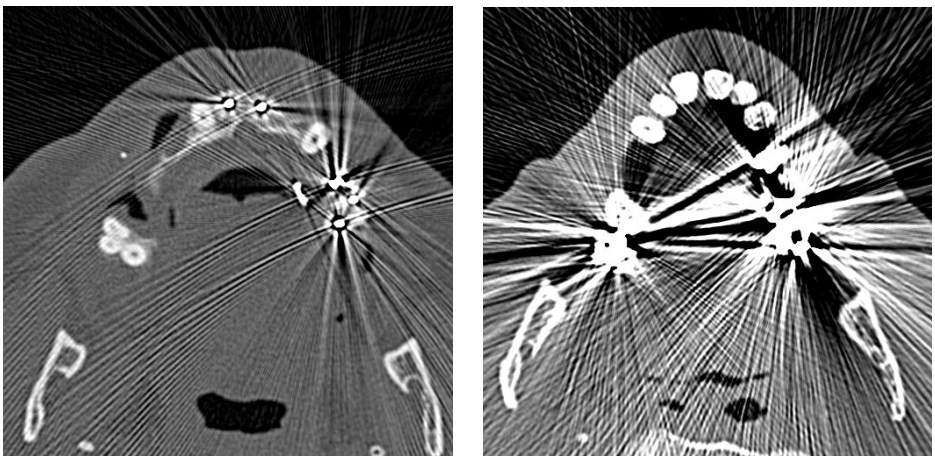

Figure 1.2: *CT scans of human skulls containing amalgam dental fillings (courtesy of prof. G. Marchal).*

some new artifacts. Hence, there is great demand for more effective metal artifact reduction.

1.3 Purpose of this work

The aim of this thesis is to study metal artifacts using a fundamental approach. Firstly, we want to determine the most important causes of metal artifacts. For this purpose we developed a high-resolution CT-simulator (chapter 3), and we performed a number of simulations and measurements. The simulator allows to make very realistic simulations, adapted to different scanner geometries. For illustration: the simulator is currently also being used for simulating micro-CT-scanners by other research groups [12]. The most important causes of metal artifacts were found to be noise, beam hardening, the NLPV effect, and scatter [24].

Secondly, once the most important causes of metal artifacts are known, they must be corrected. For this purpose we want to use iterative reconstruction (chapter 4). Iterative reconstruction allows to incorporate a dedicated forward model of the acquisition. More in particular, we can include a model for all important causes of metal artifacts. We hypothesize that artifacts are due to deviations of the acquisition model assumed by the reconstruction algorithm from the real scanner. Consequently, using a more accurate acquisition model should result in reduced artifacts. In chapter 5, we present new iterative reconstruction algorithms incorporating models for noise, beam hardening, and the NLPV effect. Good results are obtained for simulations and phantom measurements, confirming that improving the forward model results in reduced artifacts. The scatter model requires further research. Finally, the different models are combined into one global algorithm for reduction of metal artifacts.

. . . computed tomography . . .

Chapter 2

X-ray computed tomography

2.1 Introduction

This chapter describes the basics of CT. In section 2.2, we give a general overview of CT. This is followed by a discussion of the physics of X-rays in section 2.3: X-ray production, X-ray interactions and X-ray detectors. Section 2.4 describes the data acquisition in CT, i.e. how an entire plane is scanned and how the data are ordered. Section 2.5 takes up the important topic of image reconstruction, focusing on analytic reconstruction methods. The description of CT imaging is extended to three dimensions in section 2.6. Finally, section 2.7 elaborates on CT-scanner technology, i.e. on scanner generations and scanner geometry.

2.2 Overview of X-ray computed tomography

X-ray computed tomography or *CT* (figure 2.1) is an imaging modality that produces cross-sectional images representing the X-ray attenuation properties of the body. The word tomography originates from the Greek words $\tau o \mu o \varsigma$ (slice) and $\gamma \rho \alpha \phi \epsilon \iota \nu$ (to write). Image formation of a cross-section is represented in figure 2.2: using a thin X-ray beam, a set of lines is scanned covering the entire *field of view* ((a) for a parallel-beam geometry or (b) for a fan-beam geometry). This process is repeated for a large number of angles, yielding line attenuation measurements for all possible angles and for all possible distances from the center. Based on all these measurements, the actual attenuation at each point of the scanned slice can be *reconstructed*. Although there are other imaging modalities (MRI, ultrasound, PET and SPECT) that represent a kind of computed tomography, the term CT (originally CAT) is allocated for X-ray comput(eriz)ed (axial) tomography.

The history of CT begins in 1895, when Wilhelm Konrad Röntgen reported the discovery of what he called "a new kind of rays". Röntgen received the first Nobel prize in physics in 1901. Reconstruction of a function from its projections

was first formulated by Johann Radon in 1917. The first CT-scanner (the EMI scanner) was developed by Godfrey N. Hounsfield in 1972 [62]. His work was based on mathematical and experimental methods developed by A. M. Cormack a decade earlier [20, 21]. Hounsfield and Cormack shared the Noble prize in medicine and physiology in 1979. Spiral CT and multi-slice CT (section 2.6) were introduced in respectively 1989 and 1998.

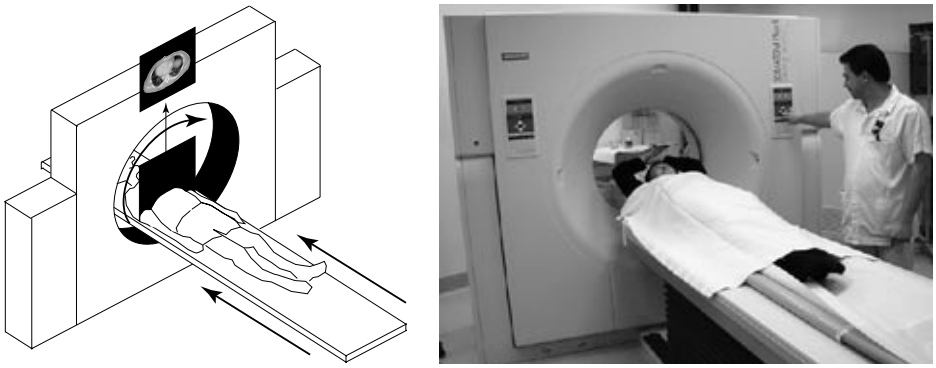

(a) (b)

Figure 2.1: *Schematic representation (a) and photograph (b) of a CT-scanner.*

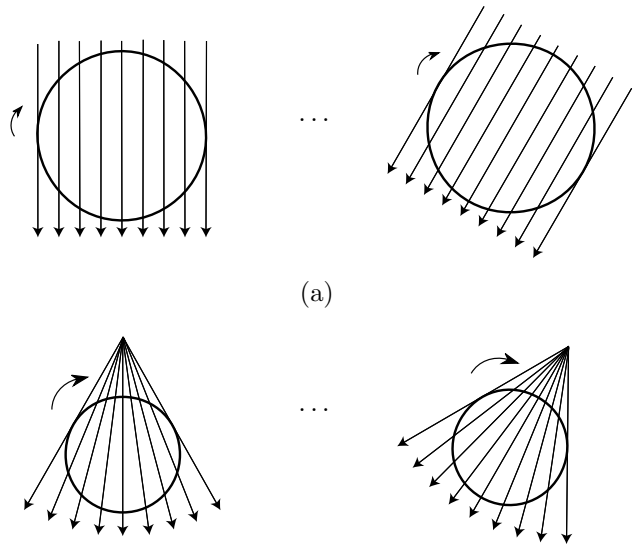

Figure 2.2: *Basic scanning procedure in CT. A set of lines is scanned covering the entire field of view: (a) parallel-beam geometry and (b) fan-beam geometry. This process is repeated for a large number of angles.*

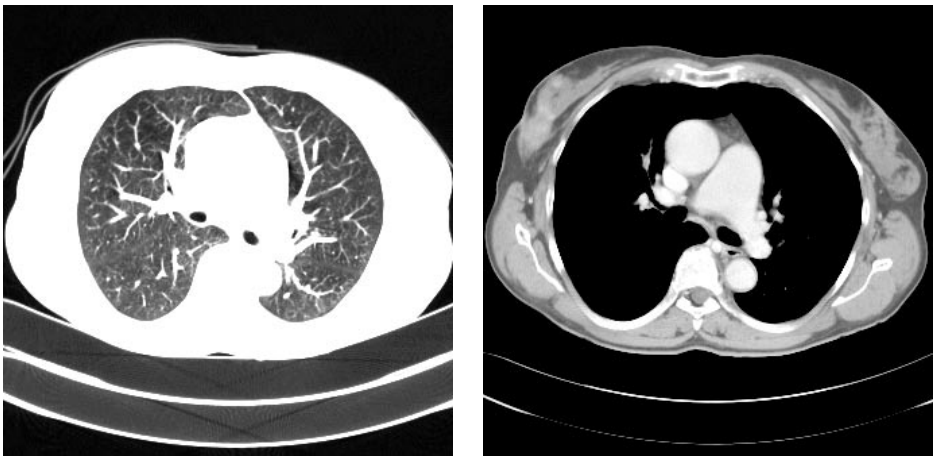

(a) (b)

Figure 2.3: *CT-image of the chest with different window/level settings:(a) for the lungs (window 1500 and level -500) and (b) for the soft tissues (window 350 and level 50).*

In modern CT-scanners, images consist of 512 × 512 pixels representing the *CT-number*, which is expressed in *Hounsfield Units* (HU). The CT-number is defined as

$$\text{CT-number (in HU)} \;=\; \frac{\mu - \mu_{H_2O}}{\mu_{H_2O}} \cdot 1000. \tag{2.1}$$

μ is the linear attenuation coefficient. With this definition, air, water and bone have a CT-number of respectively -1000 HU, 0 HU and 1000 HU. Because the dynamic range is too high to be perceived in a single image, a suitable gray level transformation must be applied. In clinical practice this is done by a real-time window/level operation. Assume a displaying interval [CT_{min} ; CT_{max}], then the *level* is defined as the center of this interval: level = (CT_{min}+CT_{max})/2, and the *window* is defined as the total span of this interval: window = (CT_{max} - CT_{min}). Figure 2.3 shows an example of a CT-image of the chest with two different window/level settings, the first to visualize the lungs (a), the second to emphasize the soft tissues (b).

2.3 X-rays

X-rays are electromagnetic waves. Electromagnetic radiation consists of photons. Each photon has an energy E, inversely proportional to its wavelength λ:

$$E = \frac{hc}{\lambda} = h\nu, \tag{2.2}$$

where $h = 6.6261 \cdot 10^{-20}$Js is Planck's constant, $c = 3 \cdot 10^{8}$m/s is the speed of light, and ν is the wave frequency. The wavelength for X-rays is in the order of Ångstrøm

(10^{-10} m) and consequently, the corresponding photon energies are in the order of 10 keV (1 eV = $1.602\,10^{-19}$ J). CT typically uses X-rays with photon energies between 30 keV and 140 keV.

2.3.1 Production of X-rays

X-rays are generated in an *X-ray tube*, which consists of a vacuum tube with a *cathode* and an *anode* (figure 2.4 (a)). The *cathode current* (typically about 5 A) releases electrons at the cathode by thermal excitation. These electrons are accelerated towards the anode by a *tube voltage* U between the cathode and the anode. U varies typically between 80 kV and 140 kV. The resulting *tube current* from anode to cathode is in the order of 100 mA. When the electrons hit the anode, they loose their excess energy in essentially three possible ways:

1. An electron can collide with an outer shell electron. A part of its energy is then transfered to this secondary electron and is finally dissipated into heat. This explains the necessity of cooling the anode.

2. An electron can interact with a nucleus. It slides around the nucleus and releases its energy by producing so-called *Bremsstrahlung*. The energy (expressed in eV) of the Bremsstrahlung photons is bounded by

$$E \leq E_{\max} = qU, \tag{2.3}$$

   where q is the electric charge of an electron. For example, if $U = 100$ kV then $E_{\max} = 100$ keV. Bremsstrahlung yields a continuous X-ray spectrum.

3. An electron can collide with an inner shell electron (e.g. from the K-shell) and eject it, leaving a hole. This hole is refilled when an electron of higher energy (e.g. from the L-shell) drops into the hole while emitting a photon of a very specific energy. The energy of this photon is the difference between the energies of the two electron states, e.g. when an electron from the L-shell (with energy E_L) drops into the K-shell (getting energy E_K), a photon of energy

$$E = E_L - E_K \tag{2.4}$$

   is emitted. Such transitions therefore yield characteristic peaks in the X-ray spectrum, superimposed onto the continuous Bremsstrahlung spectrum. This radiation is called *characteristic radiation*.

Some tungsten spectra are shown in figure 2.4 (b). The number of photons emitted per unit time is controlled by the cathode current. The energy of the emitted photons (expressed in keV) is controlled by the tube voltage (expressed in kV). Finally, X-ray beams are usually pre-filtered before leaving the X-ray tube, using thin metal sheets (Al, Cu, ...). This has the advantage that the spectrum shifts toward higher energy, resulting in reduced beam hardening effect inside the patient (see section 3.4.2). More details on the production of X-rays are found in [69].

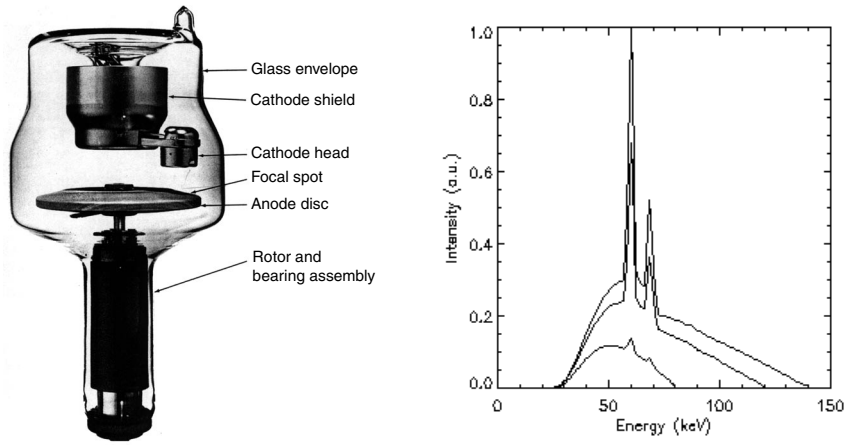

(a) (b)

Figure 2.4: *(a) Picture of an X-ray tube (Courtesy Machlett Laboratories, Inc.). (b) Intensity distribution of the X-ray spectrum of tungsten for nominal tube voltages of 80 kV, 120 kV, and 140 kV.*

2.3.2 Interaction of X-rays with matter

X-ray photons can interact with matter in several ways:

- An X-ray photon can be absorbed by ejecting a so-called photo-electron from an inner shell (e.g. the K-shell). The electron escapes from the atom in the same direction the incoming photon was traveling. This mechanism is called the *photo-electric effect*.

- An X-ray photon can also interact with an outer electron. The electron is recoiled and is made vibrating. Only a part of the photon energy is transfered to the electron. A photon with the remaining energy is emitted in a direction deviating from the direction of the incoming photon with an angle α. The electron is recoiled in a direction making an angle γ with the direction of the incoming photon. The angles α and γ are related through the law of conservation of momentum. This process is called *Compton scattering*. A limiting case of Compton scatter is coherent scatter or Thomson scatter. Here, the electron is not recoiled but is only made vibrating, and the photon doesn't loose any of its energy.

- At higher energies, *pair production* occurs. The photon interacts with the nucleus and creates an electron-positron pair.

- At still higher energies photons may cause nuclear reactions.

Only the first two types of interactions are important in CT.

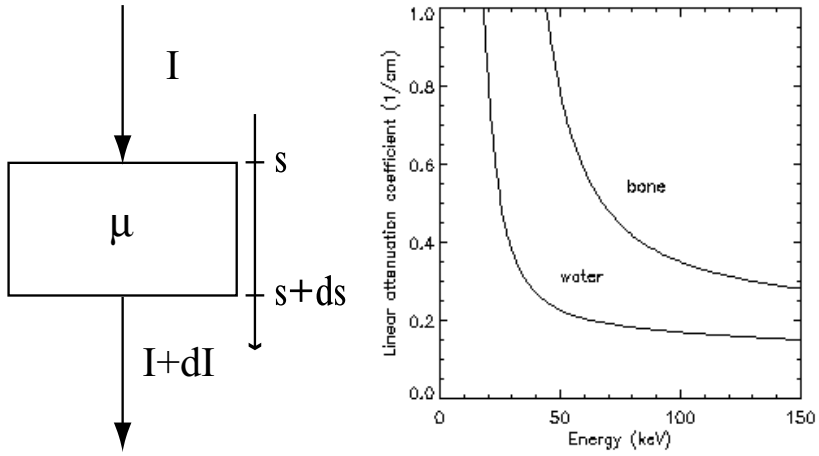

(a) (b)

Figure 2.5: *(a) X-ray beam traveling through a thin slab of material with linear attenuation coefficient μ. (b) The energy-dependent linear attenuation coefficient for bone and water.*

Consider an X-ray beam traveling through an infinitesimally thin slab of material with thickness ds (figure 2.5 (a)). This beam is attenuated by the processes mentioned above. The in-going intensity is I and the out-coming intensity is $I + dI$, Intensity is defined as the energy transmitted per unit time per unit area, the energy being proportional to the number of photons. The linear attenuation coefficient μ is then defined as

$$\mu = -\frac{\frac{dI}{ds}}{I}, \tag{2.5}$$

or 'the fraction of the X-ray beam that is attenuated per unit distance'. Integration gives

$$I(s) = I(0) \cdot \exp\big(-\int_0^s \mu(s') \cdot ds'\big). \tag{2.6}$$

This is a basic equation in CT. Although the individual interactions are of statistical nature, the macroscopic intensity of the beam follows a deterministic exponential law. In fact, the intensity and the attenuation also depend on the photon energy, and we should write

$$I(s) = \int_0^{E_{\max}} I(0, E) \cdot \exp\big(-\int_0^s \mu(s', E) \cdot ds'\big) \cdot dE. \tag{2.7}$$

Figure 2.5 (b) shows the linear attenuation coefficient $\mu(E)$ for bone and water. It decreases with the energy E and it increases with the atomic number Z. More information on interaction of X-rays with matter is found in [69].

2.3.3 X-ray detectors

In order to produce an image from the attenuated X-ray beams, the X-rays must be captured and converted to an electric signal. Three types of X-ray detectors are used in CT.

The first CT-scanners used scintillator crystals with photo-multiplier tubes (PMT). The scintillator material converts X-rays into visible light (scintillations), which then falls onto the PMT that produces an electric current. These detectors have a high quantum efficiency and a fast response time, a disadvantage is their low packing density. Scintillation crystals with PMT's were used in the earliest CT-scanners, but today they have been replaced by newer types of detectors, such as xenon gas ionization detectors.

A gas ionization detector element consists of a pressurized gas chamber with two or three electrodes. Some of the incident X-rays are absorbed: this is the photo-electric effect. The resulting free electrons and gas ions drift towards the anode and cathode respectively, giving rise to a measurable electric signal. Typically, pressures between 10 and 30 bar are used, as a compromise between absorption efficiency and ionic mobility. Gas ionization detectors have a low quantum efficiency (about 60%) and a slow response time (about 700 μs). An advantage compared to photo-multiplier tubes is their high packing density.

Modern scanners are provided with solid state detectors, combining scintillator crystals with photodiodes. A solid-state detector consists of a scintillation crystals (CsI) coupled to a photo-diode. The latter converts scintillations into a measurable electric current. The newest solid-state detectors have a very fast response time, a high quantum efficiency (over 98%), a high packing density, a good stability over time and a good reliability.

All types of CT detectors give an estimate of the total detected energy, compared to the number of photons in nuclear medicine. The relationship between the detector output signal and the detected photon energy is characteristic for every detector type. Ideally the output signal should be proportional to the detected energy. More information on X-ray detectors is found in [108].

2.4 Data acquisition

Consider the 2D parallel-beam geometry in figure 2.6 (a). $\mu(x, y)$ represents the distribution of the linear attenuation coefficient in the xy-plane. It is assumed that the patient lies along the z-axis and that $\mu(x, y)$ is zero outside a circular field of view with diameter FOV. The X-ray beams make an angle θ with the y-axis. The unattenuated intensity of the X-ray beams is I_0. A new coordinate system (r, s) is defined by rotating (x, y) over the angle θ. This gives the following transformation

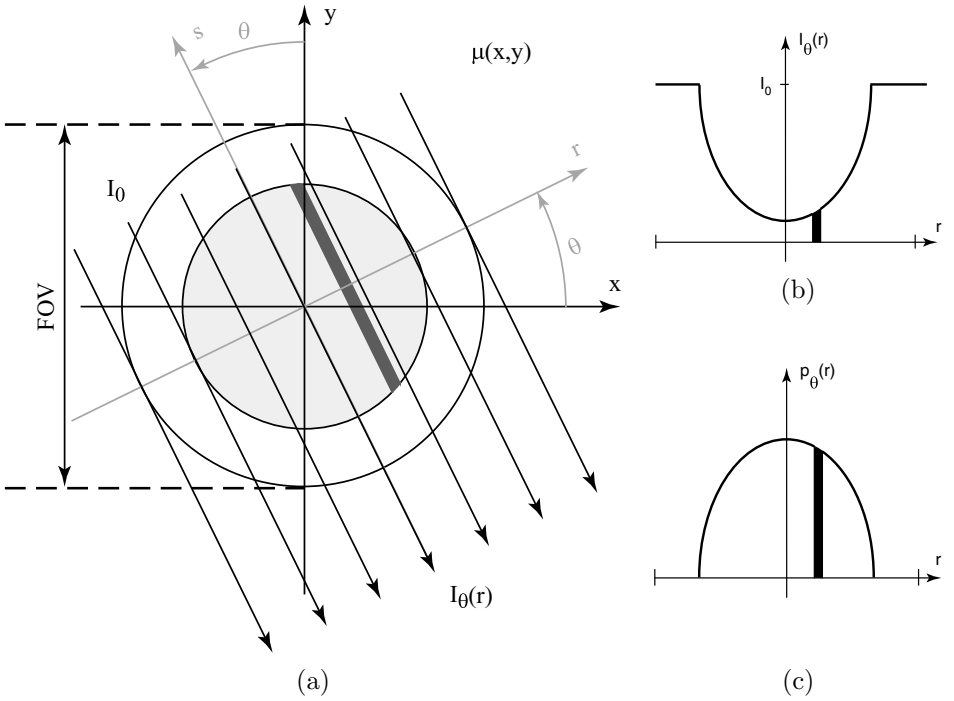

Figure 2.6: *(a) Parallel beam geometry with coordinate systems. The X-ray beams make an angle θ with the y-axis and are at distance r from the origin. (b) An intensity profile $I_\theta(r)$ is measured for every view (defined by an angle θ). I_0 is the unattenuated intensity. (c) The attenuation profiles $p_\theta(r)$ are obtained by log-converting the intensity profiles $I_\theta(r)$ and are the projections of the function $\mu(x, y)$ along the angle θ.*

formulas:

$$\begin{aligned} \begin{bmatrix} r \\ s \end{bmatrix} &= \begin{bmatrix} \cos\theta & \sin\theta \\ -\sin\theta & \cos\theta \end{bmatrix} \begin{bmatrix} x \\ y \end{bmatrix} \\ \begin{bmatrix} x \\ y \end{bmatrix} &= \begin{bmatrix} \cos\theta & -\sin\theta \\ \sin\theta & \cos\theta \end{bmatrix} \begin{bmatrix} r \\ s \end{bmatrix} \end{aligned} \tag{2.8}$$

and the Jacobian is

$$J = \begin{vmatrix} \cos\theta & -\sin\theta \\ \sin\theta & \cos\theta \end{vmatrix} = 1. \tag{2.9}$$

For a fixed angle θ, the measured intensity profile as a function of r is shown in figure 2.6 (b) and is given by

$$I_\theta(r) = I_0 \cdot e^{-\int_{L_{r,\theta}} \mu(r\cdot\cos\theta - s\cdot\sin\theta, r\cdot\sin\theta + s\cdot\cos\theta)\cdot ds}. \tag{2.10}$$

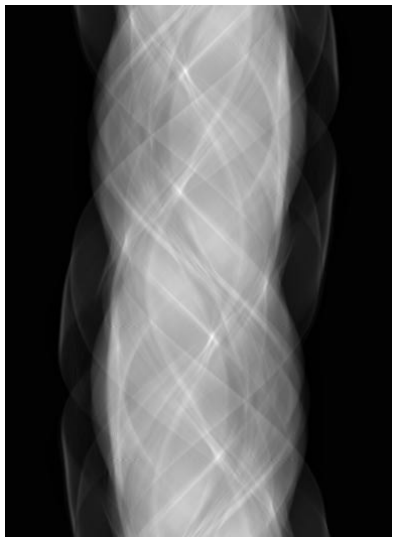

Figure 2.7: *A parallel beam sinogram obtained by stacking together a number of 1D projections at different angles θ (from 0 to 2π).*

$L_{r,\theta}$ is the line that makes an angle θ with the y-axis at distance r from the origin. Actually, the spectrum of the X-ray tube is continuous, yielding

$$I_\theta(r) = \int_0^{E_{\max}} I_0(E) \cdot e^{-\int_{L_{r,\theta}} \mu_E(r\cdot\cos\theta - s\cdot\sin\theta, r\cdot\sin\theta + s\cdot\cos\theta)ds} dE, \tag{2.11}$$

where $E_{\max}$ is the maximum photon energy, which is equal to the tube voltage. However, usually it is assumed that the X-rays are mono-chromatic and eq.(2.10) is used. Each intensity profile is transformed into an attenuation profile:

$$p_\theta(r) = -\ln \frac{I_\theta(r)}{I_0} = \int_{L_{r,\theta}} \mu(r\cdot\cos\theta - s\cdot\sin\theta, r\cdot\sin\theta + s\cdot\cos\theta)ds. \tag{2.12}$$

$p_\theta(r)$ is the *projection* of the function $\mu(x,y)$ along the angle θ (figure 2.6 (c)). Note that $p_\theta(r)$ is zero for $|r| \geqslant \text{FOV}/2$.

$p_\theta(r)$ can be measured for θ ranging from 0 to 2π. As concurrent beams coming from opposite sides yield identical measurements, attenuation profiles acquired at opposite sides contain redundant information. Therefore, as far as parallel-beam geometry is concerned, it is sufficient to measure $p_\theta(r)$ for θ ranging from 0 to π.

Stacking all these projections $p_\theta(r)$ for varying θ (for instance from 0 to 2π) results in a 2D data set $p(r,\theta)$, called *sinogram* (see figure 2.7).

Assume a distribution $\mu(x,y)$ containing a single dot as in Figure 2.8 (a-b). The corresponding projection function $p(r,\theta)$ (figure 2.8 (c)) has a sinusoidal shape, which explains the origin of the name sinogram. In mathematics, the transformation

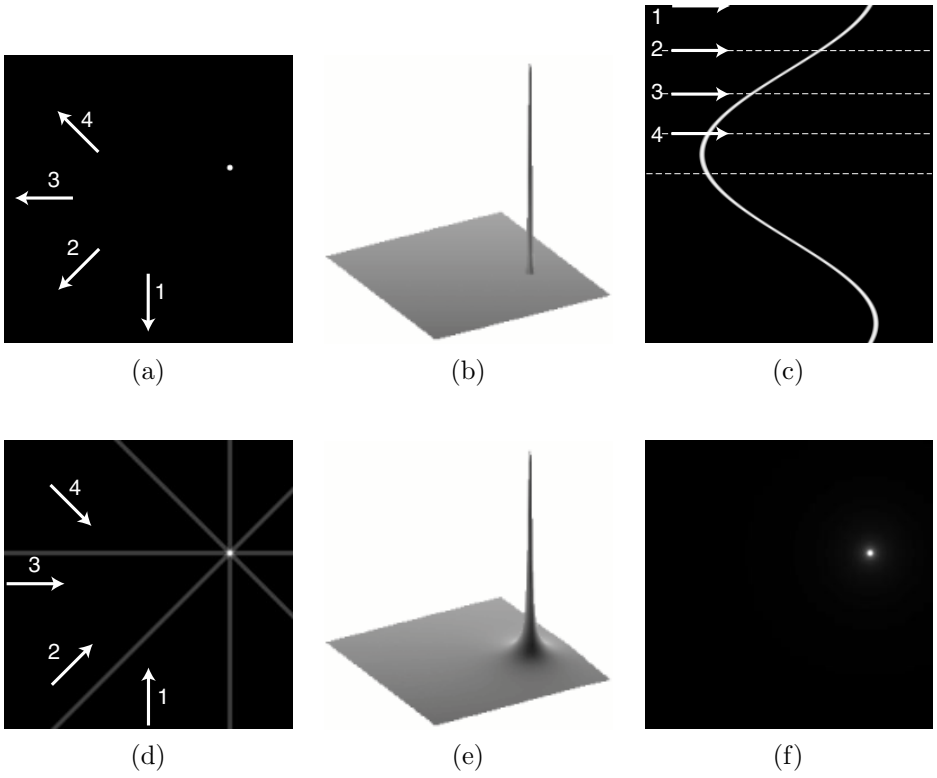

Figure 2.8: *(a-b) Image and surface plot of a distribution $\mu(x, y)$ containing one single dot. The arrows indicate four example projection directions. (c)* $360°$*-sinogram obtained by projecting $\mu(x, y)$. The arrows indicate the views that correspond to the projection directions indicated in (a). (d) Back-projection of the four views indicated in (c). (e-f) Surface plot and image of the backprojection of the entire sinogram in (c).*

of any function $f(x, y)$ into its parallel beam projections $p(r, \theta)$ is called the *Radon transform*:

$$p(r,\theta) = \mathcal{R}\big\{f(x,y)\big\} = \int_{-\infty}^{\infty} f(r\cdot\cos\theta - s\cdot\sin\theta, r\cdot\sin\theta + s\cdot\cos\theta)\; ds. \tag{2.13}$$

The Radon transform has the following properties:

- $p(r, \theta)$ is periodic in θ with period 2π

$$p(r,\theta) = p(r,\theta + 2\pi). \tag{2.14}$$

- $p(r, \theta)$ is symmetric in θ with period π

$$p(r,\theta) = p(-r,\theta \pm \pi). \tag{2.15}$$

Until now, we have assumed that data are available for all possible angles θ and distances r. In practice, we have a limited number M of projections or *views* and a limited number N of detector samples (e.g. 1056 views and 768 detector samples). The sinogram $p(r,\theta)$ becomes a matrix $p[n,m] = p(n\Delta r, m\Delta\theta)$ with M rows and N columns. Δr is the detector sampling distance and $\Delta\theta$ is the rotation interval between subsequent views. Both must be sufficiently small in order to prevent aliasing artifacts.

2.5 Image reconstruction

2.5.1 Backprojection

Given the sinogram $p(r,\theta)$, the question is how to reconstruct the distribution $\mu(x,y)$ (or – generically – the function $f(x,y)$). Intuitively, one could think of the following procedure. For a particular line (r,θ), assign the value $p(r,\theta)$ to all points (x,y) along that line. Repeat this (i.e. integrate) for θ varying from 0 to π. This procedure is called *backprojection* and is given by

$$b(x,y) = \mathcal{B}\big\{p(r,\theta)\big\} = \int_0^\pi p(x\cdot\cos\theta + y\cdot\sin\theta,\theta)\ d\theta. \tag{2.16}$$

Figure 2.8 (d-f) illustrates the backprojection for a dot. By backprojecting only a few projections the image in figure 2.8 (d) is obtained. The backprojection of all the projections is shown in figure 2.8 (e-f). The image is blurred when compared to the original. The narrow peak of the original dot has a cone-like shape after reconstruction. From this example, it is clear that a backprojection as such is not a good reconstruction method.

The discrete version of the backprojection becomes

$$b(x_i,y_j) = \sum_{m=1}^{M} p(x_i\cdot\cos\theta_m + y_j\cdot\sin\theta_m,\theta_m)\ \Delta\theta. \tag{2.17}$$

The discrete positions r_n generally do not coincide with the discrete values $(x_i\cos\theta_m + y_j\sin\theta_m)$. Interpolation is therefore required. Figure 2.9 illustrates this. For each view, a projection line through each pixel is drawn. The intersection of this line with the detector array is computed and the corresponding projection value is calculated by interpolation between its neighboring measured values.

2.5.2 Projection theorem

Instead of this intuitive solution, we need a mathematical answer to the question: given the sinogram $p(r,\theta)$, what is the original function $f(x,y)$? This means that we need a mathematical expression for the inverse Radon transform

$$f(x,y) = \mathcal{R}^{-1}\big\{p(r,\theta)\big\}. \tag{2.18}$$

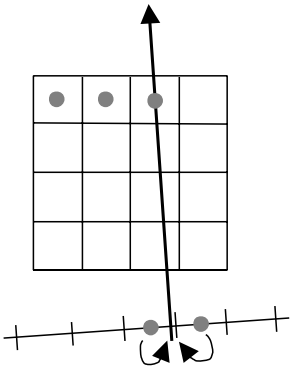

Figure 2.9: *Discrete backprojection with interpolation. For each view, a projection line through each pixel is drawn. The intersection of this line with the detector array is computed and the corresponding projection value is calculated by interpolation between its neighboring measured values.*

The *projection theorem*, also called the *central slice theorem*, gives an answer to this question. Let $F(k_x, k_y)$ be the 2D Fourier transform (FT) of $f(x, y)$:

$$F(k_x, k_y) = \int_{-\infty}^{\infty} \int_{-\infty}^{\infty} f(x, y)\ e^{-2\pi i(k_x x + k_y y)}\ dx\ dy, \tag{2.19}$$

where $i = \sqrt{-1}$, and let $P(k, \theta)$ be the 1D FT of $p(r, \theta)$ with respect to the first variable:

$$P(k, \theta) = \int_{-\infty}^{\infty} p(r, \theta)\ e^{-2\pi i(k \cdot r)}\ dr. \tag{2.20}$$

The projection theorem now states that

$$P(k, \theta) = F(k_x, k_y) \tag{2.21}$$

$$\text{with} \quad \begin{cases} k_x = k \cdot \cos\theta \\ k_y = k \cdot \sin\theta. \end{cases} \tag{2.22}$$

I.e., the 1D FT w.r.t. variable r of the Radon transform of a 2D function is the 2D FT of that function. Hence, it is possible to calculate $f(x, y)$ for each point (x, y) based on all its projections $p_\theta(r)$, θ varying between 0 and π. A proof of the projection theorem is given in appendix A.1.

2.5.3 Direct Fourier reconstruction

Based on the projection theorem, we can use the following algorithm to calculate $f(x, y)$:

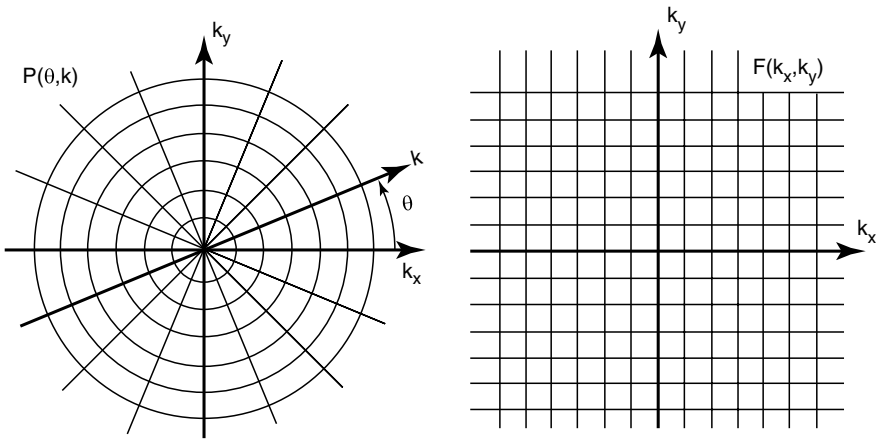

(a) (b)

Figure 2.10: *(a) The function $P(k,\theta)$ is sampled on a polar grid. (b) Samples of the function $F(k_x,k_y)$ on a Cartesian grid are required.*

(1) calculate the 1D FT $\mathcal{F}_1$ of $p(r,\theta)$ with respect to r:

$$\mathcal{F}_1\big\{p(r,\theta)\big\} = P(k,\theta) \tag{2.23}$$

(2) and calculate the 2D inverse FT $\mathcal{F}_2^{-1}$ of $F(k_x,k_y) = P(k,\theta)$:

$$\mathcal{F}_2^{-1}\big\{F(k_x,k_y)\big\} = f(x,y). \tag{2.24}$$

Taking into account the discrete nature of the data, this becomes:

(1) for all θ_m (varying from 0 to π), calculate the 1D discrete FT $\mathcal{F}_1$ of $p(r_n,\theta_m)$ with respect to r_n:

$$\mathcal{F}_1\big\{p(r_n,\theta_m)\big\} = P(k_{n'},\theta_m), \tag{2.25}$$

(2) for every θ_m, put the values of $P(k_{n'},\theta_m)$ on a polar grid,

(3) Calculate $F(k_{x_{i'}},k_{y_{j'}})$ (sampled on a Cartesian grid) from $P(k_{n'},\theta_m)$, using bilinear interpolation,

(4) and calculate the 2D inverse discrete FT $\mathcal{F}_2^{-1}$ of $F(k_{x_{i'}},k_{y_{j'}})$:

$$\mathcal{F}_2^{-1}\big\{F(k_{x_{i'}},k_{y_{j'}})\big\} = f(x_i,y_j). \tag{2.26}$$

The interpolation step (3) makes direct Fourier reconstruction less popular than reconstruction by filtered backprojection, discussed below.

2.5.4 Filtered backprojection

The polar version of the 2D inverse FT avoids interpolation:

$$\begin{aligned} f(x,y) &= \int_0^{\pi} \int_{-\infty}^{\infty} P(k,\theta)\ |k|\ e^{i2\pi kr}\ dk\ d\theta, \quad \text{with } r = x\cos\theta + y\sin\theta \\ &= \int_0^{\pi} \int_{-\infty}^{\infty} P^*(k,\theta)\ e^{i2\pi kr}\ dk\ d\theta, \quad \text{with } r = x\cos\theta + y\sin\theta \\ &= \int_0^{\pi} p^*(r,\theta)\ d\theta, \quad \text{with } r = x\cos\theta + y\sin\theta, \end{aligned} \tag{2.27}$$

where $|k|$ is the absolute value of the Jacobian of the polar transformation. By definition

$$p^*(r,\theta) = \int_{-\infty}^{+\infty} P^*(k,\theta)\ e^{i2\pi kr} dk \tag{2.28}$$

and

$$P^*(k,\theta) = P(k,\theta) \cdot |k|. \tag{2.29}$$

Hence, the function $f(x,y)$ can be reconstructed by backprojecting $p^*(r,\theta)$, which is the inverse one-dimensional FT w.r.t. k of $P^*(k,\theta)$. $P^*(k,\theta)$ is obtained by multiplying $P(k,\theta)$ by the *ramp filter* $|k|$. This explains the name filtered backprojection (FBP) [4]. It can be seen from eq.(2.27) that data must be available for an angular range from 0 to π only. Since a multiplication in the Fourier domain can be written as a convolution in the spatial domain, $p^*(r,\theta)$ can also be written as:

$$p^*(r,\theta) = \int_{-\infty}^{+\infty} p(r',\theta)\ q(r-r')\ dr' \tag{2.30}$$

$$\begin{aligned} \text{with } \ q(r) &= \mathcal{F}^{-1}\big\{|k|\big\} \\ &= \int_{-\infty}^{+\infty} |k|\ e^{i2\pi kr}\ dk. \end{aligned} \tag{2.31}$$

$q(r)$ is called the convolution kernel. This yields the following reconstruction scheme:

(1) filter the sinogram $p(r,\theta)$:

$$\forall\theta: \qquad p^*(r,\theta) = p(r,\theta) \otimes q(r) \qquad \text{or} \qquad P^*(k,\theta) = P(k,\theta) \cdot |k| \tag{2.32}$$

(2) and backproject the filtered sinogram $p^*(r,\theta)$:

$$f(x,y) = \int_0^{\pi} p^*(x\cos\theta + y\sin\theta, \theta)\ d\theta. \tag{2.33}$$

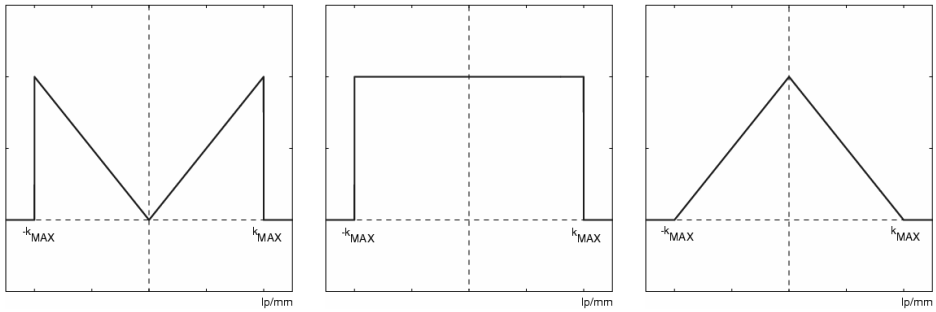

(a) (b) (c)

Figure 2.11: *(a) For a discrete implementation, the ramp filter $|k|$ is cut off at frequency k_{MAX}. The resulting filter is the difference of a block function (b) and a triangular function (c).*

Due to its divergent nature, the continuous filter $|k|$ is not useful in practice. For discrete projection data the useful Fourier content is limited to frequencies smaller than $k_{MAX} = 1/2\Delta r$, where Δr is the sampling distance. Therefore, the filter $|k|$ can be limited to these frequencies and is cut off at k_{MAX} (figure 2.11 (a)). This filter, called the Ram-Lak filter after its inventors Ramachandran and Lakshiminarayanan, can be written as the difference of a block and a triangle (figure 2.11 (b-c)). Their inverse FT yield

$$q(r) = \frac{k_{MAX}\sin(2\pi k_{MAX} r)}{\pi r} - \frac{1-\cos(2\pi k_{MAX} r)}{2\pi^2 r^2}. \tag{2.34}$$

Usually, frequencies slightly below k_{MAX} are unreliable due to aliasing and noise. Application of a smoothing window (Hanning, Hamming, Shepp-Logan, Butterworth, ...) suppresses the highest spatial frequencies and reduces these artifacts. For example the window

$$H(k) = \begin{cases} \alpha + (1-\alpha)\cos(\frac{\pi k}{k_{MAX}}) & \text{for } |k| < k_{MAX} \\ 0 & \text{for } |k| \geqslant k_{MAX}. \end{cases} \tag{2.35}$$

with $\alpha = 0.54$ is the Hamming window and with $\alpha = 0.5$ the Hanning window (figure 2.12 (a)). Figure 2.12 (b) shows the products of a ramp-filter and a Hamming/Hanning window.

2.5.5 Fan-beam filtered backprojection

In the previous sections we assumed a parallel-beam geometry. In modern CT scanners, the acquired data are not ordered in parallel subsets but in fans (figure 2.2). Figure 2.13 (a) shows the coordinates used in parallel-beam geometries (r,θ), together with those used in fan-beam geometries (α,β). β is the angle between the

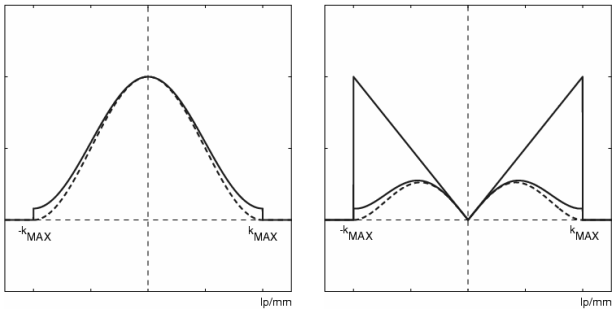

(a) (b)

Figure 2.12: *(a) Hamming window with* $\alpha = 0.54$ *and Hanning window (dashed) with* $\alpha = 0.5$*. (b) Ramp filter and its products with a Hamming window and a Hanning window (dashed).*

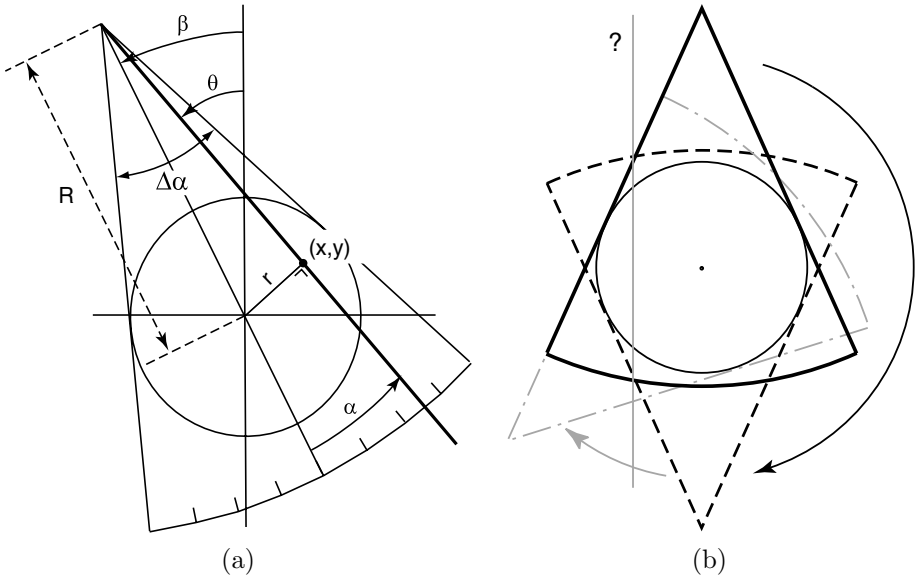

(a) (b)

Figure 2.13: *(a) Fan-beam geometry.* β *is the angle between the center line of a fan and the y-axis.* α *is the angle between a particular ray and the center line.* $\Delta\alpha$ *is the total fan-angle. (b) With the fan-beam geometry a measurement range from* $\beta = 0$ *to* $(\pi + \Delta\alpha)$ *is required to acquire all the projection lines.*

top of the fan and the y-axis. α is the angle between a particular ray and the center line of the corresponding fan. The total fan-angle is given by $\Delta\alpha$. Using the coordinates (α, β) for a fan-beam geometry (figure 2.13 (a)), the following coordinate

transformations are derived:

$$\begin{cases} \theta &= \alpha + \beta \\ r &= R\sin\alpha. \end{cases} \tag{2.36}$$

As can be seen in figure 2.13 (b), using a fan-beam geometry, measurements for β varying from 0 to π no longer include all possible line measurements. Suppose the X-ray tube starts above the patient ($\beta = 0$) and rotates clockwise over 180°, then most but not all lines have been measured, such as for example the vertical line with accompanying question mark in figure 2.13 (b). Actually, a range from 0 to (π + $\Delta\alpha$) is required in order to include all line measurements. For simplicity, we will assume that data for β varying from 0 to 2π are available (360°-acquisition). Two possible reconstruction approaches exist:

- Rebinning: this is the reordering of the data into parallel data.
- An adapted fan-beam FBP algorithm can be used.

Reordering of the data into parallel data requires interpolation [58, 119]. Assuming fan-beam measurements are available at projection lines (α_n,β_m) for n=1→N and m=1→M, the corresponding parallel-beam measurement at a given ($r_{n'}$,$\theta_{m'}$) can be calculated by

$$p(r_{n'}, \theta_{m'}) = \sum_{i=0}^{1}\sum_{j=0}^{1} c_i \cdot d_i \cdot p(\alpha_{n'+i}, \beta_{m'+j}), \tag{2.37}$$

where $\alpha_{n'}$ and $\beta_{m'}$ are the largest available values such that

$$\begin{aligned} \alpha_{n'} &<= \alpha &&= \operatorname{asin}(\frac{r_{n'}}{R}) \\ \beta_{m'} &<= \beta &&= \theta_{m'} - \alpha, \end{aligned} \tag{2.38}$$

and where

$$\begin{aligned} c_0 &= (\alpha_{n'+1} - \alpha)/(\alpha_{n'+1} - \alpha_{n'}) \\ c_1 &= 1 - c_0 \\ d_0 &= (\beta_{m'+1} - \beta)/(\beta_{m'+1} - \beta_{m'}) \\ d_1 &= 1 - d_0. \end{aligned} \tag{2.39}$$

A dedicated fan-beam FBP algorithm [56, 57] is obtained by using the coordinates (α, β) for a fan-beam geometry (figure 2.13 (a)):

$$f(x,y) = \int_0^{2\pi} \frac{1}{v^2} \int_{-\frac{\Delta\alpha}{2}}^{+\frac{\Delta\alpha}{2}} [\frac{1}{2} R\cos\alpha \; p(\alpha,\beta)] \big(\frac{\gamma-\alpha}{\sin(\gamma-\alpha)}\big)^2 \; q(\gamma-\alpha) \; d\alpha \; d\beta. \tag{2.40}$$

Note that this is a modified backprojection weighted with $\frac{1}{v^2}$. The inner integral is a convolution of $p(\alpha, \beta)$, weighted with $\frac{1}{2}R\cos\alpha$, with a modified filter kernel $\big(\frac{\alpha}{\sin\alpha}\big)^2 q(\alpha)$. A derivation is given in appendix A.2.

All reconstruction methods discussed in the previous sessions are transform methods: they are based on the analytic inversion of the Radon transform. For a more detailed discussion, we refer to [4, 56, 57, 79, 94, 108, 136].

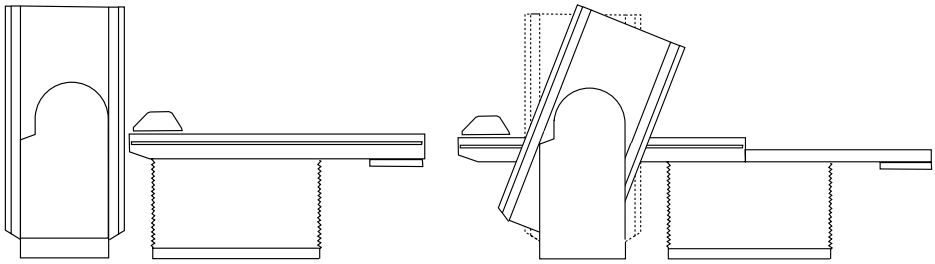

Figure 2.14: *Schematic views of a spiral CT-scanner showing gantry tilt and table translation.*

2.6 Imaging in three dimensions

The most straightforward way to image an entire volume is to scan a number of consecutive slices by translating the table intermittently, also called *sequential CT*. The *gantry* – this is the part of the CT-scanner that contains the rotating parts – can be tilted over a limited angle for imaging oblique slices (figure 2.14).

A technique that is widely spread nowadays is *spiral CT* or *helical CT* [5, 23, 80, 83, 84]. The X-ray tube rotates continuously around the patient, just like in 2D CT. At the same time, the patient is slowly translated through the gantry (figure 2.14). Hence, the tube describes a helical orbit w.r.t. to the patient. The *table feed* is the axial distance over which the table translates during a complete tube rotation of 360°. The pitch ratio – or simply *pitch* – is the ratio between the table feed and the collimated slice thickness. The pitch must be small enough in order to avoid spiral artifacts, typically between 1.0 and 2.0. The most obvious solution for reconstructing a 2D slice based on a 3D spiral acquisition is to use measurements over a range of 360° and to ignore the table motion. This results in longitudinal smoothing and spiral artifacts. More advanced methods synthesize data for a particular reconstruction plane using linear or cubic interpolation between data measured at the same angle β but at different axial positions (*full-scan-* or 360°-interpolation). It is also possible to combine data measured from opposite sides (*half-scan-* or 180°-interpolation). A detailed analysis of spiral CT and spiral interpolation is found in [5, 23, 80, 83, 84].

Since 1998, a number of manufacturers have commercialized *multi-slice CT* [66, 81, 90, 98]. This type of scanner allows to acquire multiple slices simultaneously using adjacent detector arrays (figure 2.15), compared to one slice in a single-slice CT-scanner. The number of detector arrays varies between 8 and 34, depending on the manufacturer. By combining several detector arrays and using appropriate z-collimation, different slice widths are obtained. Until now, all manufacturers have in common that maximum 4 slices are scanned simultaneously. The main advantage of multi-slice CT-scanners is the ability of faster scanning. With a 4-slice system and a 0.5 second rotation, it is for instance possible to obtain a CT of the lungs in a few seconds while the patient holds his/her breath. Faster scanning results in reduced motion artifacts. Shorter scan times result in a longer tube lifetime and

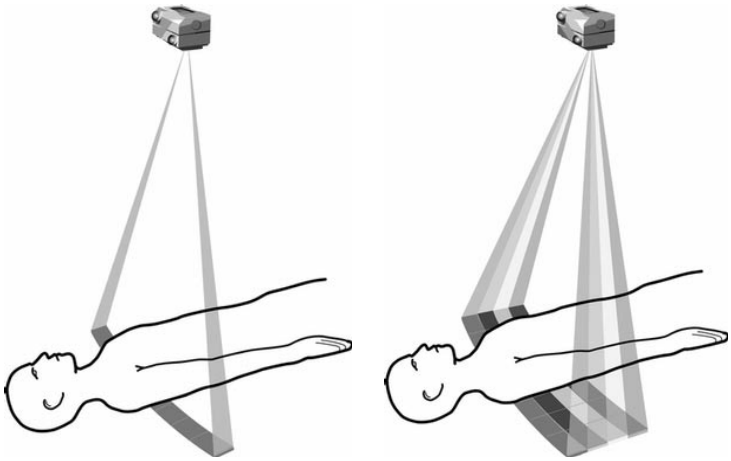

(a) (b)

Figure 2.15: *(a) Single-slice CT versus (b) multi-slice CT: a multi-slice CT-scanner can acquire four slices simultaneously by using four adjacent detector arrays (with permission of RSNA).*

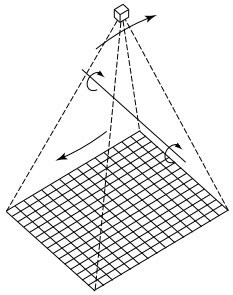

Figure 2.16: *A cone-beam geometry is based on a 2D detector array. An entire volume is measured in one single orbit of the X-ray tube.*

eliminate the need to wait for tube cooling between scans.

If the detector array is extended to a 2D array of detector elements, an entire volume is measured in one single orbit of the X-ray tube. This is called *cone-beam CT* (figure 2.16). Unfortunately, except for the central plane, the in-plane data required for 2D reconstruction are not measured. A dedicated 3D cone-beam approach is then needed. If the distance between the X-ray tube and the detector array is large and/or the axial width of the detector is limited, all the projection lines can be assumed to be parallel to the central plane. In this case, the problem reduces to the reconstruction of a series of 2D images. This is what happens in multi-slice CT, discussed above.

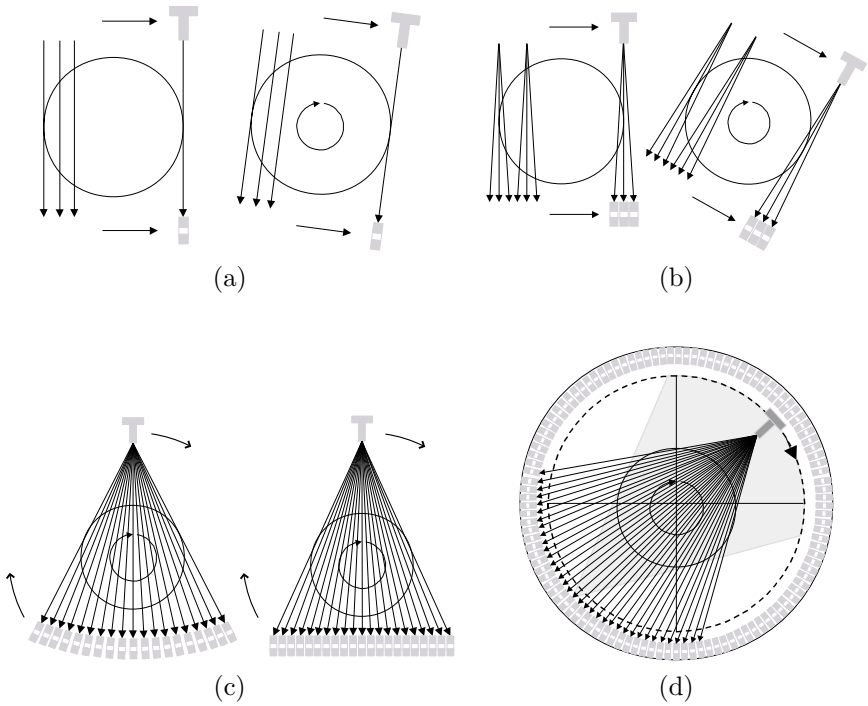

Figure 2.17: *Subsequent scanner generations: (a) first generation, (b) second generation, (c) third generation and (d) fourth generation CT-scanner.*

2.7 Equipment

Having discussed the theory of CT imaging, let us now have a closer look at the technology of CT-scanners, i.e. the different scanner generations and the internal scanner geometry. Figure 2.17 shows subsequent scanner generations and the corresponding modes of acquisition:

In first-generation scanners, also called "rotate-translate-type scanners", the tube-detector unit consists of an X-ray tube and one detector element. This unit is moved along the field of view while measuring the line attenuation at equidistant positions. This process is systematically repeated after rotation of the tube-detector unit over a small angular interval, until a complete 180° rotation has been performed (5 minutes/slice).

In second-generation scanners, the tube-detector unit consists of an X-ray tube and multiple detector elements. Again, the unit is translated across the field of view while measuring the attenuation at equidistant positions. Similar to the first generation this process is systematically repeated. However, the multiple detector

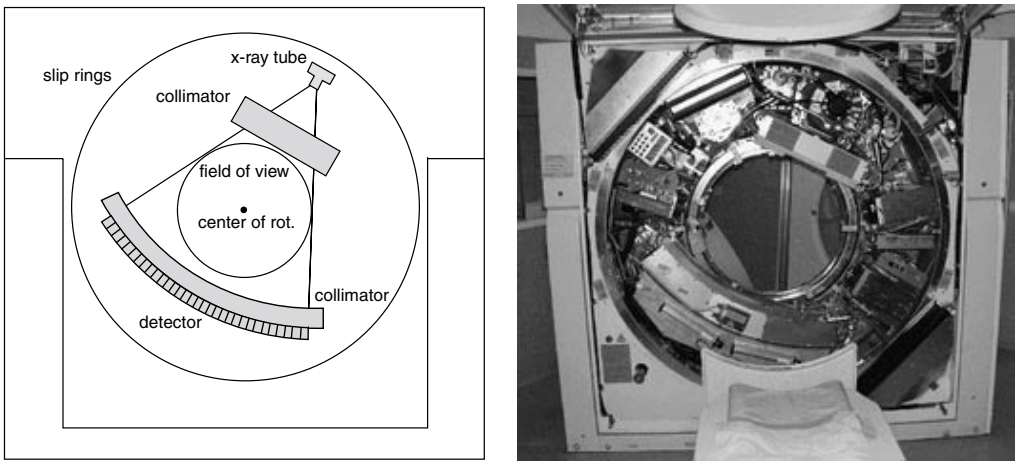

(a) (b)

Figure 2.18: *The basic internal geometry of a third generation spiral CT-scanner: (a) schematic overview and (b) picture.*

elements allow a larger rotation interval, resulting in a reduced acquisition time (20 seconds/slice).

In third-generation scanners, the tube-detector unit consists of an X-ray tube and a detector array covering the entire field of view. The unit continuously rotates around the scanned object. From now on, the data are arranged in fans, hence the name fan-beam geometry instead of parallel-beam geometry (0.5 seconds/slice).

In fourth-generation scanners, the detector elements are positioned stationary on a full circle around the scanned object. The X-ray tube rotates on a concentric circle. Unlike for the other generations, each view is now made up of one detector element and a large number of tube positions (gray background in figure 2.17 (d)). The number of views is defined by the number of detectors and the sampling density within each view depends on the frequency at which the detector elements are sampled.

Nowadays the third-generation geometry is by far the most successful. This has two important reasons. Firstly, fourth-generation scanners require a larger number of detector elements. Secondly, the fixed detector geometry makes it more difficult to prevent scattered radiation (see below). The basic geometry of a third-generation spiral CT-scanner is shown in figure 2.18. In front of the X-ray tube is a collimator, which limits the transmitted X-rays to the selected slice and prevents useless irradiation of the patient. A post-patient collimator is used to limit the detected scattered radiation. Additionally, solid state detectors in third generation scanners have external septa in between the detector elements in order to prevent

detection of scattered radiation. Scanners with gas detectors do not have such in-plane collimators because they are self-collimating. In fourth generation scanners in-plane septa are rare. The reason is that the orientation of the detectors with respect to the rotating tube continuously changes, which requires the septa to rotate as well. The circle inscribed by the tube-detector fan determines the field of view. Data and power are transmitted from and to the rotating tube-detector unit through *slip rings* (not shown). These are sliding contacts which eliminate the mechanical problems that would be implied by cables connecting fixed and rotating parts.

To terminate this chapter we briefly mention one other type of CT-scanner: electron beam tomography (EBT), also called ultrafast CT[1]. Here, the X-ray tube - until now a compact unit - has become an integrated part of the system. Electrons, produced by an electron gun, pass through an electromagnetic focusing coil and are bent electro-magnetically onto one of four tungsten target rings lying in the gantry below the patient. The impact of electrons on the target rings produces X-rays that are directed onto a double ring of cadmium tungstate detector elements located in the gantry above the patient. The X-rays are tightly collimated before passing through the patient. Each sweep of a target ring requires 50 ms and there is an 8 ms delay to reset the beam. This provides a temporal resolution of 17 frames per second. These features make the EBT-scanner useful to produce images of the beating heart. Recently, also third generation scanners are used for cardiac imaging, by combining multi-slice CT with ECG triggering [78, 116].

2.8 Conclusion

In this chapter, we have described the basics of CT. For a more complete reference on different aspects of CT, we refer to the literature [18, 56, 79, 108, 144, 145]. We have selected the topics that are most relevant to this thesis. Two aspects are particularly important. Firstly, a perfect understanding is required of how data are acquired in CT, including the underlying physical processes. This allows to build a CT-simulator and to find causes of artifacts. Secondly, image reconstruction by FBP (for fan-beam geometry) is used as the reference reconstruction algorithm throughout the remainder of this work.

[1] see http://www.imatron.com

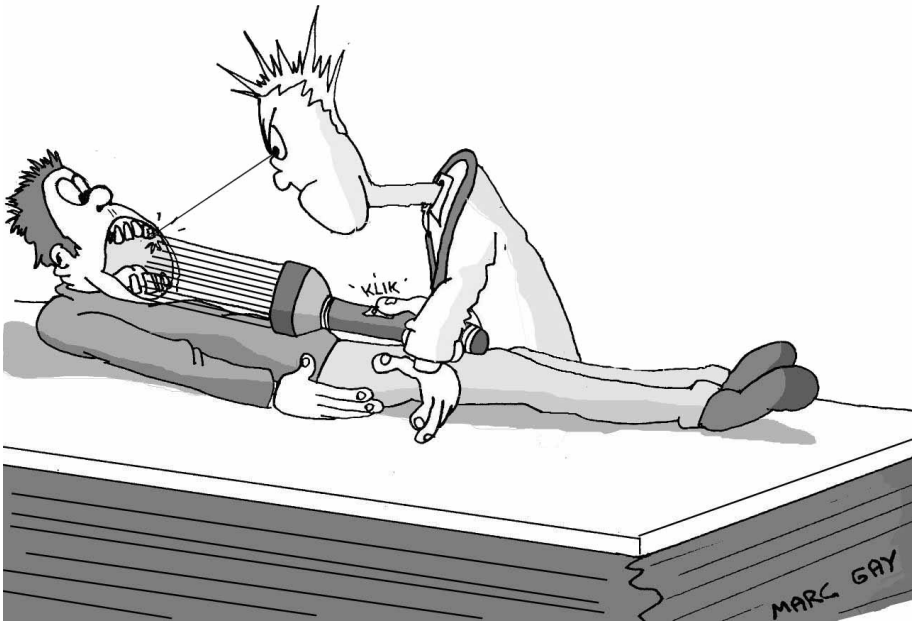

. . . determining the causes of metal artifacts . . .

Chapter 3

Simulator and simulations

3.1 Introduction

This chapter is based on [24] and presents a simulator and a simulation study to investigate the causes of metal artifacts.

Several researchers have tried to remove metal artifacts using various approaches, which are usually based on the assumption that measured data affected by metal objects are useless for the reconstruction. These 'corrupt' data are either ignored [127, 148] or replaced by synthetic data [82, 127]. In our opinion, a complete understanding of the streak generation processes is indispensable for a well-founded solution to the metal streak artifact problem. In CT literature, several causes of (more general) streak artifacts are found: beam hardening [33, 34, 72, 74, 100, 124], scatter [43, 76], trans-axial nonlinear partial volume effect [75], axial nonlinear partial volume effect [45], noise [34], object motion [46], detector under-sampling [77] and view under-sampling [73]. To investigate which of these causes are relevant to metal artifacts with modern CT-scanners, we developed a CT-simulator and we performed a number of measurements and simulations. Section 3.2 describes the simulator. Section 3.3 describes a number of experiments for validating the simulator. In section 3.4, several causes of artifacts are simulated separately. This allows to study specific types of artifacts qualitatively and to determine which are the most important causes of metal artifacts.

3.2 Simulator

The simulator is developed in IDL (Interactive Data Language, Research Systems Inc., Boulder, Colorado). It uses a projector which is implemented in C for fast computation. The simulator is based on a 2D fan-beam geometry (figure 3.1 (a)). The third dimension, perpendicular to the scanning plane, is not taken into account. Spiral artifacts [5, 109, 149] are beyond the scope of this thesis. For the simula-

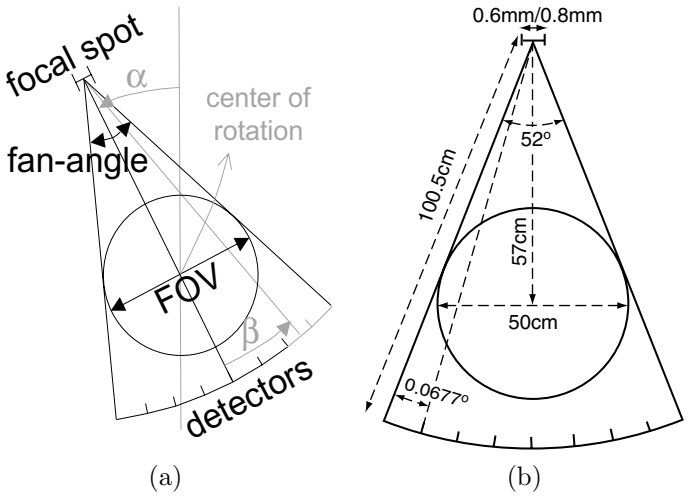

Figure 3.1: *Fan-beam scanner geometry: (a) schematic overview and (b) dimensions for a Siemens Somatom Plus 4 CT-scanner.*

Table 3.1: *Example of a simulator script containing the geometrical parameters.*

geo	; script type
768	; number of detector elements
1056	; number of views
0.908073	; fan angle (radian)
50.	; FOV [cm]
0.	; start angle [radian]
57.	; distance from source to center of rotation [cm]
100.5	; distance from source to detector [cm]
0.25	; detector offset (fraction of detector element width)
0.06	; width of the focal spot [cm]

tions described below, all geometrical parameters were adjusted to the Siemens Somatom Plus 4 CT-scanner (figure 3.1 (b)). All simulation parameters are defined in scripts. An example of a geometry script is shown in table 3.1.

The simulator is based on the calculation of the attenuation for a single projection line at a particular energy. This calculation is repeated a large number of times: projection lines are grouped into X-ray beams, monochromatic simulations are grouped into polychromatic simulations, and the calculation of polychromatic X-ray beams is repeated for all detector elements and for all views. The attenuation of a particular projection line is calculated by summing all pixel attenuation values μ_j along that line. This is called the projection. The projection is implemented like in [71] (figure 3.2): for a projection line i that is more vertical than horizontal

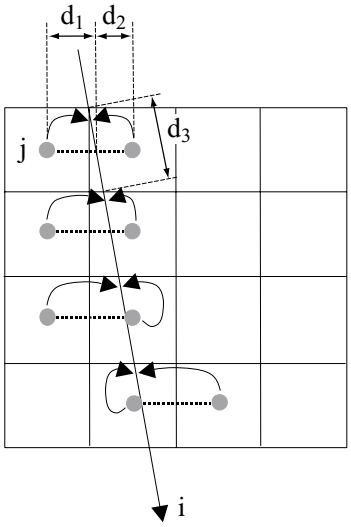

Figure 3.2: *Projector: the intersection of the projection line with each row is calculated, linear interpolation is performed between the two adjacent columns, the interpolated pixel values are summed for all rows, and this sum is multiplied with the intersection length of the projection line with one single row.*

($\theta \in [-45°; 45°]$ or $\theta \in [135°; 225°]$), the following steps are performed:

- the intersection with each row is calculated,
- linear interpolation is performed between the two adjacent columns,
- the interpolated pixel values are summed for all rows,
- and this sum is multiplied with the intersection length d_3 of the projection line with one single row.

For all other projection lines ($|\theta| \in]45°; 135°[$), the same steps are performed swapping rows and columns. The projection value for projection line i can be written as a summation:

$$p_i = \sum_{j=1}^{J} l_{ij}\mu_j, \tag{3.1}$$

where l_{ij} represents an effective intersection length of projection line i with pixel j. Using the projection method described above, this effective intersection length is defined as the product of the row (or column) intersection length and the interpolation coefficient between the two adjacent columns (or rows). Using the notation defined in figure 3.2, we have:

$$l_{ij} = d_3 \cdot \frac{d_2}{d_1 + d_2} \tag{3.2}$$

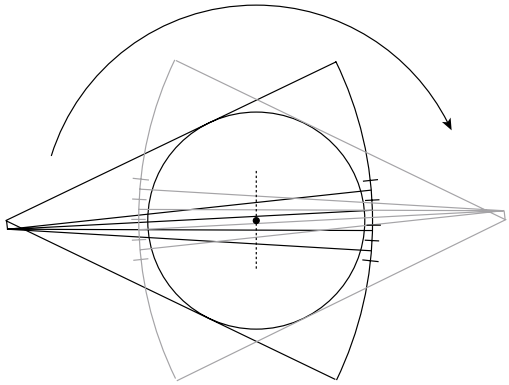

Figure 3.3: *Quarter-detector offset: the focal spot is shifted laterally over a small distance, so that the line connecting the focal spot and the center of rotation intersects the detector row at a distance from the middle equal to one quarter of a detector element. The resulting projection lines are interleaved with the opposite projection lines obtained after* 180° *rotation.*

and l_{ij} is zero for all pixels j that are not adjacent to projection line i.

CT-scanners often use a principle called *quarter detector offset* (figure 3.3) (detector offset = 0.25 in table 3.1). The focal spot is shifted laterally over a small distance, so that the line connecting the focal spot and the center of rotation intersects the detector row at one quarter of a detector element from the middle. The resulting projection lines and the opposite projection lines (obtained after 180° rotation) will be perfectly interleaved in the center of the FOV (dotted line). This removes the redundancy inherent to a standard 360° fan-beam acquisition, and the increased sampling density reduces aliasing artifacts.

For ease of computation, the X-ray source is modeled as a uniformly radiating straight line. The finite sizes of the focal spot and the detector elements are modeled by sampling at high resolution (typically 0.1mm or 0.2mm) followed by a summation of the photon flux over focal spot width (0.6mm) and detector element width (1.2mm). This is shown schematically in figure 3.4 (a). The resulting photon intensity is shown in figure 3.4 (b). Detector cross-talk is taken into account by including samples from neighboring detector elements (figure 3.5). Based on measurements of the point spread function (PSF) on the Siemens Somatom Plus 4 (section 3.3), this overlap was estimated to be about 1/6 at both sides. The manufacturer confirmed that this is a good estimate.

The continuous rotation of the tube-detector unit is simulated by sampling at small angular (or temporal) intervals followed by a summation of the photon flux over the view angle (or time) interval. This is shown in figure 3.6 (a-b). Simulations show that this finite integration time has a large influence on the PSF (see section 3.3.1). The time for one 360° rotation (0.75 s) divided by the number of views (1056) gives the expected integration time (710 μs). Measurements of the PSF on the Siemens Somatom Plus 4 (section 3.3) indicate that this integration time

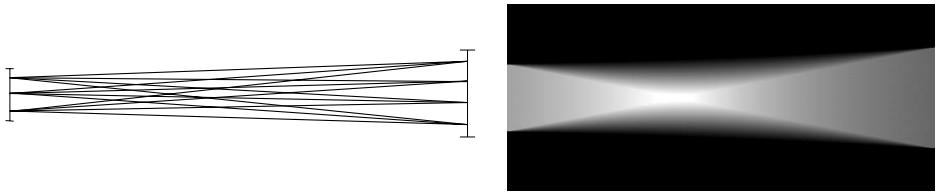

(a) (b)

Figure 3.4: *(a) The finite sizes of the focal spot and the detector elements are modeled by sampling at high resolution followed by a summation of the photon flux over focal spot width and detector element width. (b) The resulting intensity distribution.*

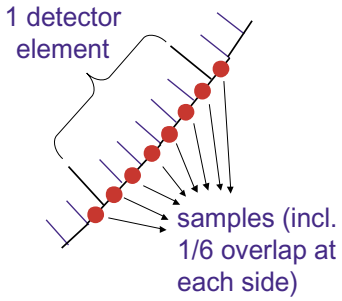

Figure 3.5: *Detector cross-talk is taken into account by including samples from neighboring detector elements.*

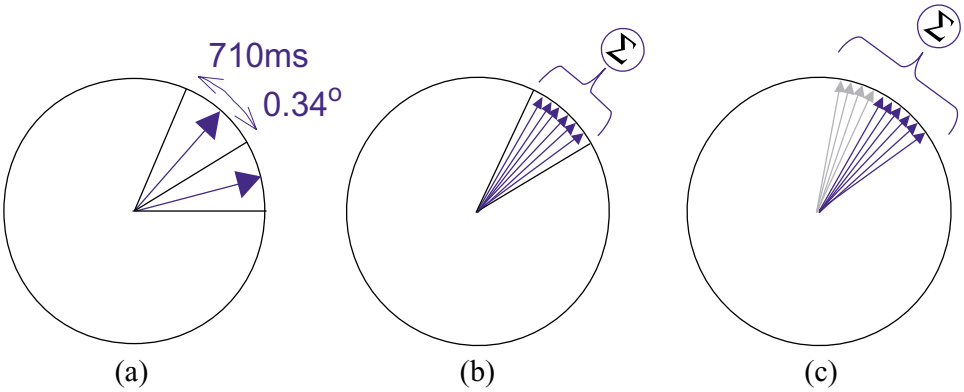

Figure 3.6: *(a-b) The continuous rotation of the tube-detector unit is simulated by sampling at small angular (or temporal) intervals followed by a summation of the photon flux over the view angle (or time) interval. (c) The after-glow effect is modeled by adding to each view an appropriate number of samples from the previous view.*

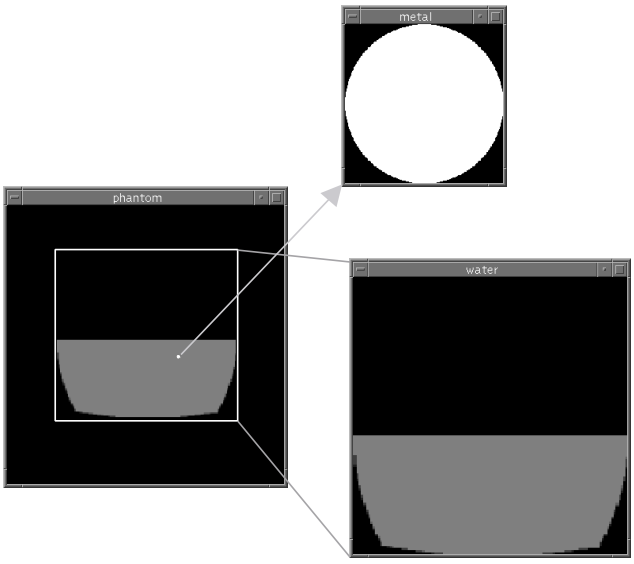

Figure 3.7: *Example of a software phantom consisting of a water bowl with an iron rod. Software phantoms are defined as the superposition of a number of basic objects, each with its own size, position, composition, and resolution.*

is about 66% higher than this expected value. We attribute this excess integration time to the ion collection time, this is the time needed for the ions to drift towards the measuring electrodes in the Xenon detectors used in the Siemens Somatom Plus 4 (they are now replaced by solid state detectors, which don't have this effect). The estimated 66% is in good agreement with the theoretical ion collection time of $600\mu s$ calculated as $t_{coll} = \frac{(\Delta x)^2}{k\ V}$ where Δx is the inter-electrode distance, V the applied voltage and $k = 0.015\frac{cm^2}{V \cdot s}$ the ionic mobility taken from [32]. This so-called '*after-glow* effect' is modeled by adding to each view an appropriate number of samples (66%) from the previous view (figure 3.6 (c)).

Software phantoms are defined as the superposition of a number of basic objects, each with its own size, position, composition, and resolution. An example of a phantom definition for a water bowl containing an iron rod is shown in figure 3.7. Every phantom part is defined by a foreground and a background substance. The actual attenuation of a phantom part is calculated by subtracting the background attenuation from the foreground attenuation. This allows to define phantom parts contained within other, larger phantom parts. This superposition principle has the advantage that for instance small metal objects can be simulated very accurately, while saving computation time by using only relatively few pixels for the background objects. More importantly, it allows to increase the number of simulated energies with only marginal increase in computation time (see below). An example of a simulator script containing the phantom definition is shown in table 3.2. Phantom part type 2 is a circular phantom part. Phantom part type 6 is the water bowl

```
ph                  ; script type
2                   ; number of phantom parts
;
; phantom part 1
;
6                   ; phantom part type
water               ; substance
no                  ; background substance
256                 ; image size [pixels]
25.                 ; part size [cm]
0.                  ; horizontal offset [cm]
0.                  ; vertical offset [cm]
;
; phantom part 2
;
2                   ; phantom part type
Fe                  ; substance
water               ; background substance
50                  ; image size [pixels]
1.16                ; part size [cm]
4.05                ; horizontal offset [cm]
0.05                ; vertical offset [cm]
```

Table 3.2: *Example of a simulator script containing the phantom definition. All distances are w.r.t. the center of rotation.*

phantom part (shape only), which is stored in a normalized bitmap.

In our simulator, the spectrum of the X-ray tube is modeled by summing a number of monochromatic simulations. The spectrum in figure 3.8 is divided into a number K of regions R_k with equal area. For each region, a monochromatic simulation is performed using attenuation coefficients μ_k. Every μ_k is calculated as a weighted average of the linear attenuation coefficient $\mu(E)$ over the corresponding part of the spectrum:

$$\mu_k = \frac{\int_{R_k} I_0(E)\,\mu(E)\,dE}{\int_{R_k} I_0(E)\,dE}, \tag{3.3}$$

where $I_0(E)$ represents the simulated spectrum. Simulated spectra were provided by Siemens for different tube voltages (140 kV in figure 3.8). These spectra include the effect of physical pre-filtration of the X-ray beam and the detector response as a function of energy (section 2.3). Linear attenuation coefficients $\mu(E)$ are obtained from [68][1].

[1] http://physics.nist.gov/PhysRefData/

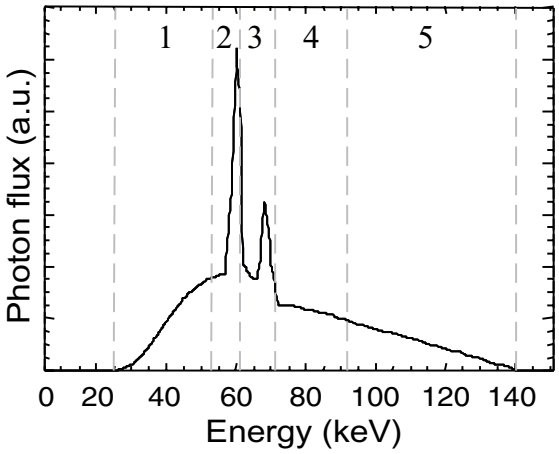

Figure 3.8: *Simulated spectrum for a nominal tube voltage of 140 kV. The polychromaticity is modeled by summing a number of monochromatic simulations. The spectrum is divided into a number of regions with equal area, and for every region, a weighted average of the linear attenuation coefficients is calculated.*

The simulator can be summarized in one formula, giving the intensity I_i detected at projection line i:

$$I_i = \frac{1}{S}\frac{1}{D}\frac{1}{V}\frac{1}{K}\sum_{s=1}^{S}\sum_{d=1}^{D}\sum_{v=1}^{V}\sum_{k=1}^{K} I_0 \cdot \exp\Big(-\sum_{p=1}^{P}\Big[\mu_{kp}\cdot\sum_{j=1}^{J_p} l_{ijpsdv}\cdot\rho_{jp}\Big]\Big), \qquad (3.4)$$

where S, D, V and K are the number of source samples, detector samples, view samples, and energy levels respectively. I_0 is the detected intensity in the absence of absorber. μ_{pk} is the linear attenuation coefficient of phantom part p at energy k. P is the number of phantom parts p. J_p is the total number of pixels in phantom part p. l_{ijpsdv} is the interpolation coefficient for projection line i and pixel j in phantom part p for source sample s, detector sample d, and view sample v. ρ_{jp} is the fill fraction of pixel j in phantom part p. For instance, a bone insert p has $\mu_{pk} = \mu_k^{\text{bone}}$. In this phantom part, a pixel that is entirely filled with bone has $\rho = 1$. A pixel with air has $\rho = 0$. The inner summation $\sum l_{ijsdvp}\rho_{jp}$ is the actual projection. l_{ijsdvp} depends on p because resolution and position can be chosen differently for different parts.

The modular phantom definition allows to bring the index k outside the projection. This reduces the number of projections by a factor K and makes computation time essentially independent of the number of energy levels. Of course, the modular approach also introduces a factor P. However, P is usually much smaller than K, and also – as stated above – J_p can be made relatively small for some phantom parts, resulting in much faster projections.

Scatter, noise, and non-linearities are added retrospectively. In accordance with [43, 76] a constant scatter profile is used for the simulations further in this chapter.

sp	; script type
2	; number of source samples
4	; number of detector samples
6	; number of view samples
1	; number of detector overlap samples
4	; number of view overlap samples
1	; perform summation after exponentiation
0.	; scatter level (fraction of I_0)
1.e5	; blank-scan I_0 [number of photons] (determines the noise level)
0	; non-linearity (OFF=0, ON=1)
50	; number of simulated energy levels
140.	; nominal tube voltage [kV]
70.	; the energy used if the simulation is monochromatic [keV]

Table 3.3: *Example of a simulator script containing the simulation parameters.*

Real scatter profiles usually contain very little high frequencies, and therefore, a constant scatter profile is expected to be a good approximation, at least for the purpose of simulating scatter artifacts. Alternative scatter models are discussed in chapter 6. Poisson noise is approximated as a Gaussian pseudo-random realization, with variance equal to the mean. According to the manufacturers, all non-linearities inherent to the detector are perfectly compensated for. Therefore, the detector response is assumed to be linear. An example of a script containing the simulation parameters is shown in table 3.3.

3.3 Validation

3.3.1 PSF experiments

Several experiments were performed, both for exploring the properties of the scanner and for validating the simulator. An iron wire with diameter $\varnothing = 0.7$ mm was positioned at different locations in – and perpendicular to – the scanning plane. Different setups are shown in figure 3.9. Measurements and simulations were performed. This allowed to estimate the PSF of the acquisition for both the real CT-scanner and the simulator. This PSF is defined as the projection of a point in the scanning plane. The full width at half maximum (FWHM) of the PSF is calculated by fitting a Gaussian. The PSF and its FWHM appear to be very view- and position-dependent. Good agreement is obtained between measured and simulated FWHM of PSF as a function of view angle (figure 3.10) (a). A good Gaussian fit of the PSF was obtained in most projections, except where the projection of the wire coincides with the border of the patient table. This explains the peaks in the measured curve. The typical cyclic behaviour has an easy intuitive explanation. The width of the PSF depends mainly on three parameters (figure 3.10 (b)): the distance $\overline{IF}$ from the iron wire to the focal spot, the distance $\overline{IC}$ from the iron wire to the center of

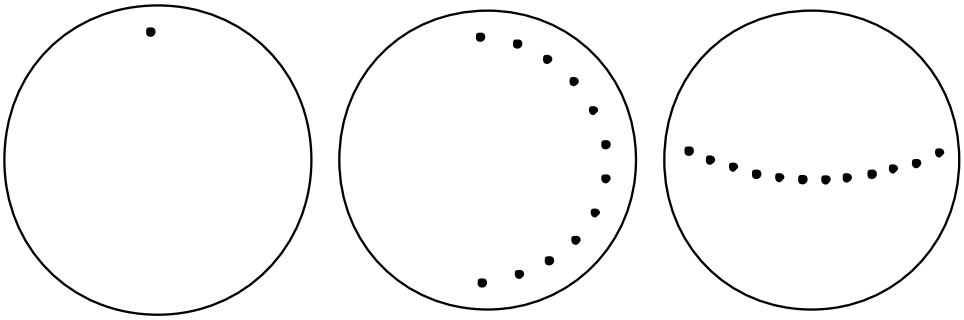

Figure 3.9: *Several experiments were performed using thin iron wires positioned perpendicular to the scanning plane.*

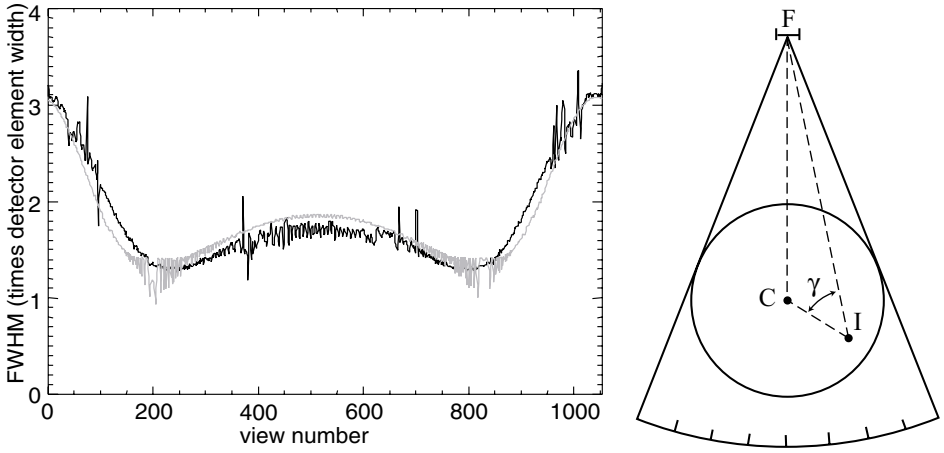

(a) (b)

Figure 3.10: *(a) FWHM of the PSF versus view number: measured (black) and simulated (gray). (b) Schematic representation of the position of the iron wire relative to the COR and the focal spot.*

rotation and the angle γ between $\overrightarrow{IF}$ and $\overrightarrow{IC}$. Distance $\overline{IF}$ determines the beam aperture and the distance between two consecutive beams at that particular location I. This gives a cyclic behaviour with a period of one rotation (360°). Distance $\overline{IC}$ and angle γ determine the speed at which a beam sweeps by at that particular position: $v_{sweep} = v_{angular} \cdot \overline{IC} \cdot |cos(\gamma)|$. This gives a cyclic behaviour with a period of a half rotation (180°). Superposition of both cyclic behaviors explains the behaviour in figure 3.10 (a).

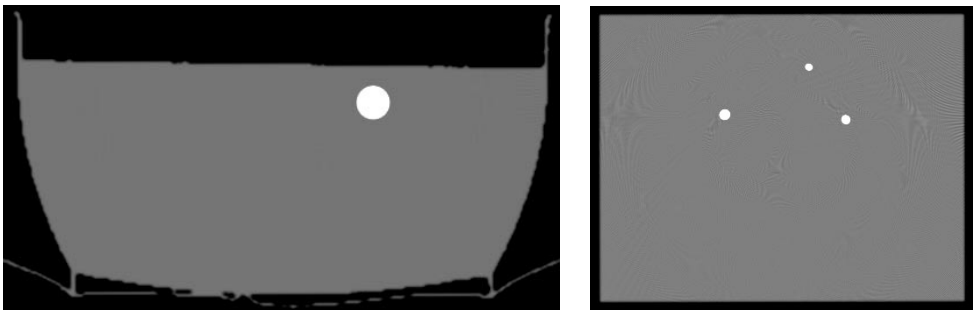

(a) (b)

Figure 3.11: *Reconstructions of artifact-free simulations: (a) phantom 1: water bowl with iron rod and (b) phantom 2: plexi plate with 3 amalgam fillings.*

3.3.2 Phantom experiments

A number of phantoms were measured and simulated. Phantom 1 consists of a water bowl and a cylindrical iron rod (ø = 11.6mm) positioned eccentrically in the water. Phantom 2 consists of a plexiglas plate with three cylindrical amalgam fillings (ø=1 mm, 2 mm, and 3 mm). Reconstructions from artifact-free simulations are shown in figure 3.11. Note that the images are actually not entirely artifact-free, but contain some low-level aliasing artifacts. Other similar plexiglas phantoms with one and two amalgam fillings were scanned.

Two reconstruction algorithms were applied (see section 2.5.5). The first is the direct fan-beam filtered backprojection algorithm from Herman [56, 57]. The second reconstruction algorithm consists of a rebinner (see section 2.5.5), followed by a parallel beam FBP. This was used only for validation of the direct fan-beam reconstruction. The results were identical, except for some extra smoothing with the rebinning approach (not shown). The backprojector from section 2.5.1 is implemented in C for fast computation. In all cases, a Hamming window with a cutoff frequency of half the maximum frequency was applied, and the windowing interval is $\mu = [0.1; 0.3]\ cm^{-1}$.

Figure 3.12 compares the measurements (top) with the simulations (bottom). Good agreement is obtained for both phantom 1 and phantom 2. The artifacts in the simulations are similar to those in the measurements, both qualitatively (by visual comparison) and quantitatively (by comparing the mean values and the standard deviations). This indicates that we can use the simulator to study the appearance of different artifacts, and compare their relative importance.

3.4 Artifact simulations

A major advantage of a CT-simulator is the possibility to change some specific properties that are always present or difficult to change in a real CT-scanner. In

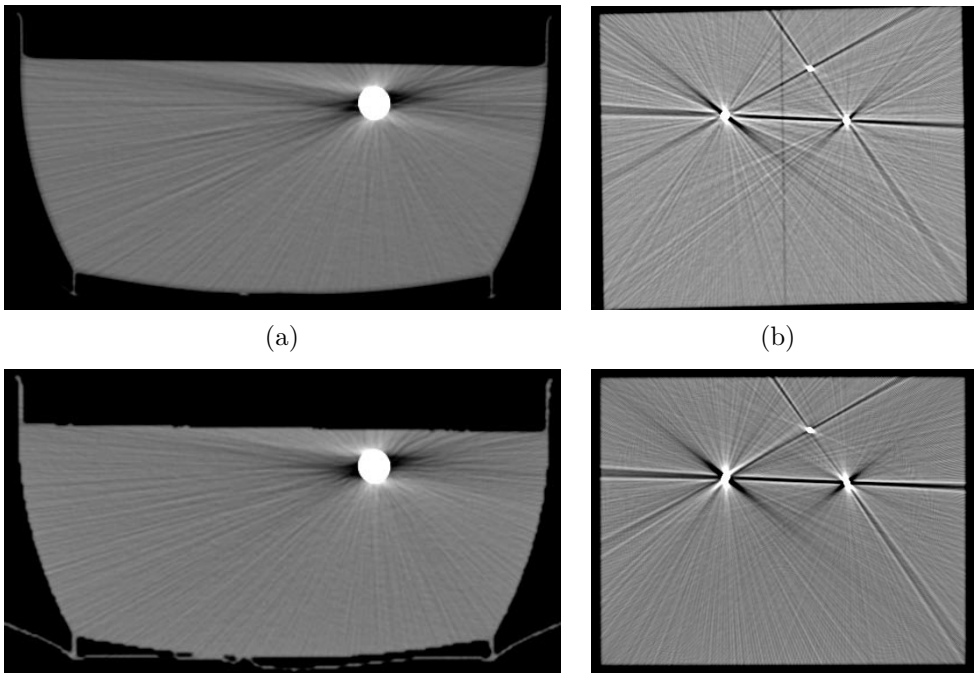

(a) (b)

(c) (d)

Figure 3.12: *Validation of the simulator by comparing simulations (bottom) and measurements (top) for phantom 1 (left) and phantom 2 (right).*

particular, we are able to switch on/off beam hardening, scatter, noise, ... This allows to make quasi artifact-free simulations like in figure 3.11, or to investigate what is the effect of each of these causes separately. In the following paragraphs, a number of causes of artifacts are explained and illustrated with simulations.

3.4.1 Noise

It is usually assumed that the main source of uncertainty results from the quantum nature of the X-ray photons (quantum noise), and therefore that the photon counts are Poisson-distributed [48, 63]. Noise is decreased by increasing the tube current (at the expense of increased patient dose) or by increasing the voxel size (at the expense of decreased spatial resolution). The statistical fluctuations on the measurements cause fine dark or bright streaks along the corresponding projection lines after reconstruction with filtered backprojection. These fine streaks are most prominent in directions of high attenuation, as the signal-to-noise (SNR) ratio of the detected intensity is relatively low there:

$$n \sim \sqrt{I} \qquad \mathrm{SNR_I} \sim \frac{I}{\sqrt{I}} \sim \sqrt{I} \sim \exp(-p/2), \tag{3.5}$$

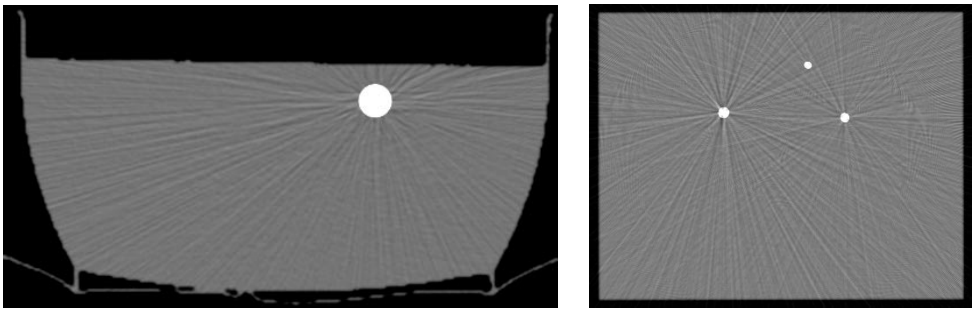

(a) (b)

Figure 3.13: *Simulations with noise: (a) phantom 1 and (b) phantom 2.*

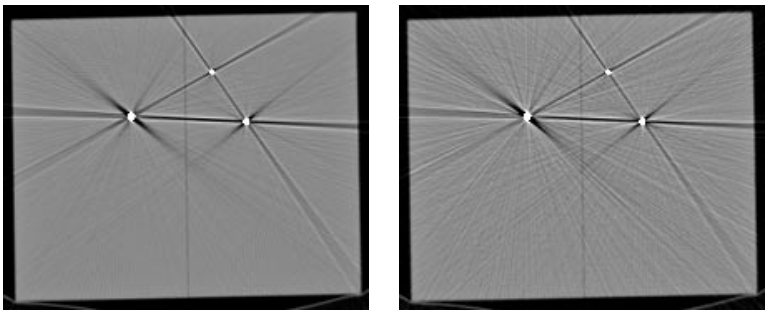

(a) (b)

Figure 3.14: *Measurements of phantom 2: (a) reconstruction of the averaged sinograms and (b) reconstruction of one single sinogram.*

where n is the noise level, I is the noise-free intensity, and p is the noise-free projection value. This shows that the degree of error is a non-linear function of the total attenuation p [34]. Note that effects such as beam hardening and scatter also have an influence on the severity of the noise artifacts, as they alter p and I.

The easiest way to study noise artifacts is using simulations, by switching the noise on/off. I_0 was chosen in the order of 10^5 photons per detector: under these circumstances, both the standard deviations on the intensities and the degree of artifact were comparable to those in the measured data. Figure 3.13 shows the simulations with noise for phantom 1 and phantom 2. Streaks are seen in directions of highest attenuation, and connecting metal objects more in particular. This type of streaks is also distinguishable in figure 3.12. Comparison with the noise-free simulations in figure 3.11 shows the net effect of noise.

In order to study noise artifacts using measurements, a phantom was scanned multiple times under identical circumstances. Averaging N measurements allows to reduce the standard deviation of the noise by a factor $\sqrt{N}$. Figure 3.14 shows the results for phantom 2. Comparing the reconstruction of the averaged sinograms

(a) with a regular reconstruction (b) allows to identify the noise artifacts. As expected, the noise streaks are strongly reduced by the averaging effect. Note that this averaging can not be applied to patient scans because of the increased dose.

3.4.2 Beam hardening

When a polychromatic X-ray beam passes through matter, low-energy photons are preferentially absorbed, as the linear attenuation coefficient generally decreases with energy. As a result, the beam gradually becomes *harder*, i.e. its mean energy increases (figure 3.15). The harder a beam, the less it is further attenuated. Therefore, the total attenuation is no longer a linear function of absorber thickness. This is schematically depicted in figure 3.16 for a homogeneous circular phantom: (a) shows an intensity profile and (b) shows a projection (or attenuation profile), both as a function of r (the location on the detector array, see chapter 2). For rays with little or no attenuation, the values are similar for the monochromatic and the polychromatic case. For rays with higher attenuation, the error becomes larger. (c) shows the projection value as a function of path length s through the absorber material. For the monochromatic case (gray line), the projection value increases linearly with path length. For the polychromatic case (black line), the projection value is a non-linear function of the path length. Neglecting this effect leads to various well-known beam hardening artifacts such as cupping, the apical artifact, streaks, and flares [7, 24, 31, 33, 34, 35, 40, 103, 122, 132, 152, 154]. Figure 3.17 gives a schematic representation of a patient. Vertical X-ray beams have short path lengths and therefore give small negative errors on p. Most horizontal X-ray beams have longer path lengths and therefore give larger negative errors. More importantly, the presence of materials that are much denser than water – such as bone – will give larger errors. As a result, dark beam hardening streaks are seen along projection lines that are attenuated most (horizontal dark band in figure 3.17). A distinct but related phenomenon is the cupping effect. X-ray beams that go through central pixels always have a relatively long path length, while beams that go through eccentric pixels can have both short and long path lengths. As a result, pixel values will always be depressed toward the center of an object.

The effect of beam hardening was investigated by comparing polychromatic and monochromatic simulations. For the latter, the simulated energy E_0 was chosen so that the resulting intensities were in the same order of magnitude as in the polychromatic case. Figure 3.18 shows the polychromatic simulations for phantom 1 and 2. For phantom 1, we observe dark streaks in the directions of highest attenuation. There is also a cupping effect, but this can not be seen with the current windowing. In the case of metal inserts (phantom 2), additional dark streaks are seen connecting the metal objects, corresponding to the directions of highest attenuation. The artifacts in these results are undoubtedly due to beam hardening, as beam hardening is the only source of artifacts that is included with respect to the artifact-free simulations in section 3.3.2. The results show that beam hardening is an important source of artifacts, and of metal artifacts in particular.

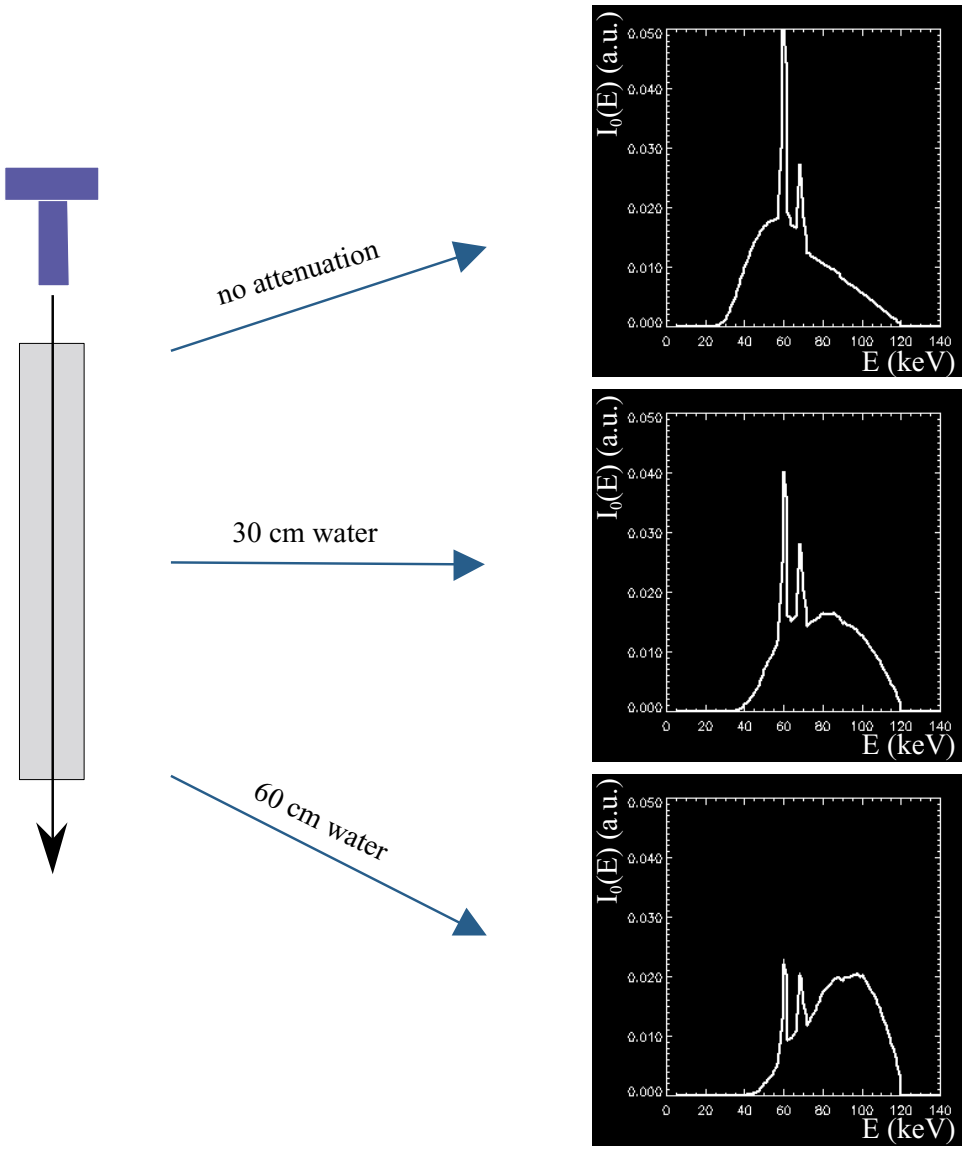

Figure 3.15: *When a polychromatic X-ray beam passes through matter (left), low-energy photons are preferentially absorbed, and the beam gradually becomes harder, i.e. its mean energy increases.*

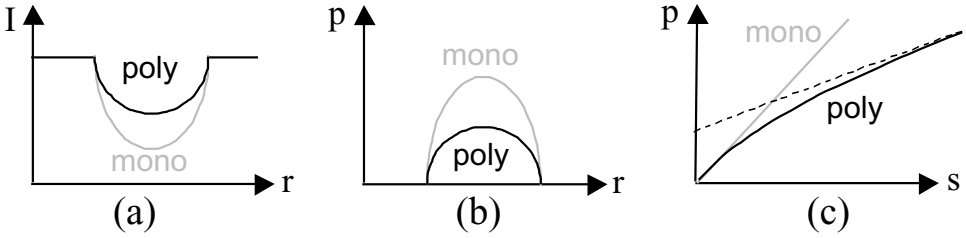

Figure 3.16: *Schematic representation of monochromatic and polychromatic measurements: (a) intensity profile, (b) attenuation profile (projection), and (c) projection value as a function of path length.*

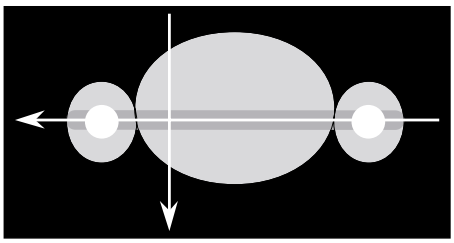

Figure 3.17: *Schematic representation of a patient. Vertical X-ray beams have short path lengths and therefore give small negative errors on p. Most horizontal X-ray beams have longer path lengths and therefore give larger negative errors.*

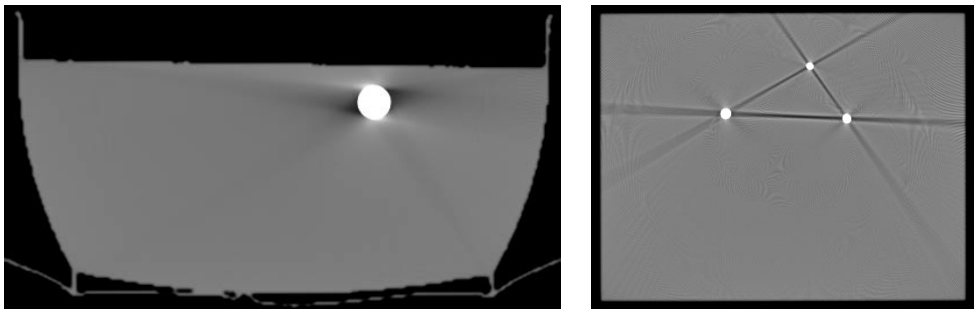

(a) (b)

Figure 3.18: *Polychromatic simulations: (a) phantom 1 and (b) phantom 2.*

3.4.3 Partial volume effect

3.4.3.1 Linear partial volume effect

If the volume represented by a voxel is only partly filled with a certain substance, the reconstructed attenuation is a fraction of the attenuation of that particular

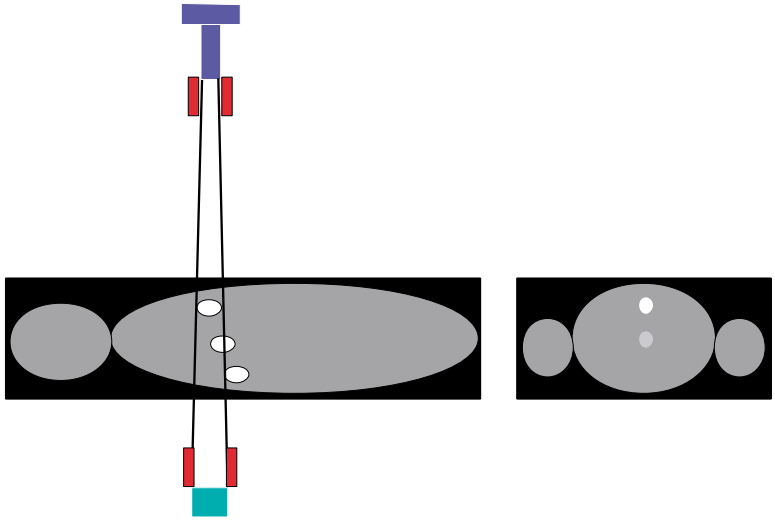

Figure 3.19: *Schematic example of the axial partial volume effect. The longitudinal view (left) shows three lesions. The upper lesion entirely fills the slice. The middle lesion only partially fills the slice. The lower lesion is completely outside the slice. In the trans-axial image (right), the contrast of these three lesions is seen to be proportional to the filled fraction of the slice.*

substance. Generally, in first order approximation (or ignoring the non-linearity due to the exponent inherent to transmission measurements), the reconstructed voxel attenuation represents the volume-weighted average of the attenuations of all substances present in that voxel. This effect is most prominent for axial averaging (because the axial resolution is usually lower than the in-plane resolution), using thick slices, and in the presence of strong z-gradients. It is commonly known as the *partial volume effect* [3, 6, 44, 88, 153]. A schematic example is shown in figure 3.19: A lesion that only partially fills a given slice (in axial direction), has lower contrast in the corresponding trans-axial image.

3.4.3.2 Non-linear partial volume effect

A related phenomenon, that is much more important within the scope of our work on metal artifacts, is the non-linear partial volume effect (NLPV). Consider two voxels with attenuation coefficients μ_1 and μ_2, as shown in figure 3.20. The ingoing intensity is I_0 and the out-going intensities are I_1 and I_2. On the detector, the out-going intensities are averaged, resulting in intensity I. The total attenuation is usually estimated by taking the logarithm of I:

$$\mu = -\ln \frac{I}{I_0} = -\ln \left(\frac{\frac{I_1}{I_0} + \frac{I_2}{I_0}}{2} \right). \tag{3.6}$$

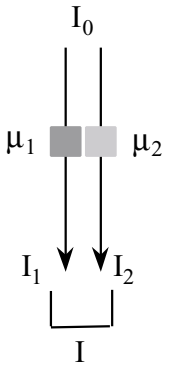

Figure 3.20: *Schematic depiction of the non-linear partial volume effect. Assume two voxels with different attenuation coefficients μ_1 and μ_2. The in-going intensity is I_0 and the out-going intensities are I_1 and I_2. The measured attenuation calculated from the average intensity I is always an underestimation of the average attenuation.*

What most reconstruction algorithms expect as input, is the average attenuation:

$$\frac{\mu_1 + \mu_2}{2} = \frac{1}{2}\left(- \ln \frac{I_1}{I_0} - \ln \frac{I_2}{I_0}\right) = - \ln \sqrt{\frac{I_1}{I_0}\frac{I_2}{I_0}}. \tag{3.7}$$

For any two positive numbers a and b, it can be proven that $(a + b)/2 \geq \sqrt{ab}$. Therefore, if $\mu_1 \neq \mu_2$, it follows from equations (3.6) and (3.7) that μ is an underestimation of $(\mu_1 + \mu_2)/2$.

Now consider an ideal attenuation profile $p(\vec{r})$ and a corresponding intensity profile

$$I(\vec{r}) = I_0 \cdot \exp(-p(\vec{r})), \tag{3.8}$$

both function of a position vector $\vec{r}$. It can then be shown (see appendix A.3) that, if $p(\vec{r})$ is not constant over a region R, then

$$- \ln \frac{\bar{I}}{I_0} \quad < \quad \bar{p}, \tag{3.9}$$

where $\bar{I}$ and $\bar{p}$ are the averages of $I(\vec{r})$ and $p(\vec{r})$ over the region R:

$$\bar{I} \quad = \quad \frac{\iint_R I(\vec{r}) d\vec{r}}{\iint_R d\vec{r}} \tag{3.10}$$

$$\bar{p} \quad = \quad \frac{\iint_R p(\vec{r}) d\vec{r}}{\iint_R d\vec{r}}. \tag{3.11}$$

In practice, this means that a gradient perpendicular to the direction of an X-ray beam causes a negative error in the corresponding estimated projection value. These theoretical findings can be applied to both axial and trans-axial gradients.

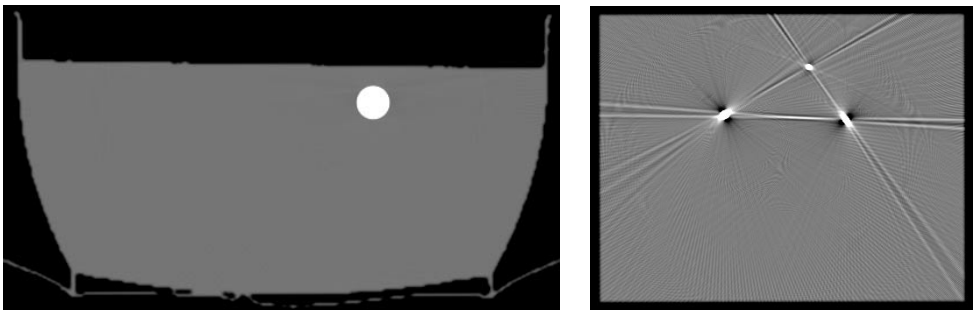

(a) (b)

Figure 3.21: *Simulation with the NLPV effect: (a) phantom 1 and (b) phantom 2.*

3.4.3.3 Transaxial non-linear partial volume effect

The trans-axial NLPV effect (tNLPV) [75, 138] results from averaging over the beam width, or more in particular over the in-plane width of the focal spot, over the in-plane width of the detector elements, and also – not to forget – over the rotation interval corresponding to one single view. The tNLPV effect manifests as dark streaks tangent to sharp edges, hence the names *exponential edge-gradient effect* [75] and *edge-induced streaking artifact* [138]. In this thesis, the tNLPV effect is investigated using two simulation modes. The standard simulation mode performs summation of the beam samples after exponentiation, i.e. it uses intensity-averaging. This is the most realistic simulation mode, and it includes the tNLPV effect. Alternatively, the summation of the beam samples can be performed before exponentiation, i.e. using attenuation-averaging. This eliminates the tNLPV effect. The simulation formula from eq.3.4 becomes:

$$I_i = \frac{1}{K}\sum_{k=1}^{K} I_0 \cdot \exp\Big(-\frac{1}{S}\frac{1}{D}\frac{1}{V}\sum_{s=1}^{S}\sum_{d=1}^{D}\sum_{v=1}^{V}\sum_{p=1}^{P}\Big[\mu_{kp}\cdot\sum_{j=1}^{J_p} l_{ijpsdv}\cdot\rho_{jp}\Big]\Big). \qquad (3.12)$$

Additionally, detector cross-talk and afterglow, which result in increased tNLPV effect, can be taken into account by extending the summation intervals.

Figure 3.21 shows the simulations with the NLPV effect. For phantom 1, no streaks are observed. For phantom 2, dark streaks are seen connecting edges with equally-signed gradients, while bright streaks are seen connecting edges with opposite gradients. Using different windowing, dark streaks are seen along the edges of the plexi plate (not shown). Additionally, a number of streaks are seen radiating from the metals.

3.4.3.4 Axial non-linear partial volume effect

The axial NLPV effect results from averaging over the slice width, or more in particular over the axial width of the focal spot and over the axial width of the

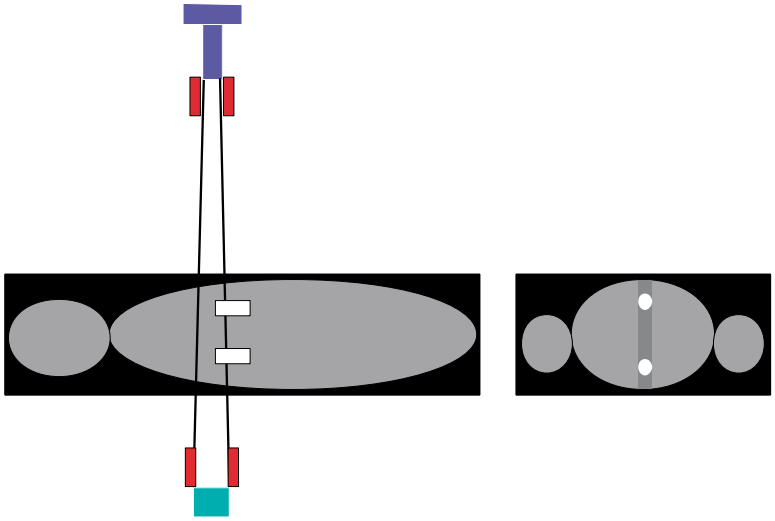

Figure 3.22: *Schematic example of the axial non-linear partial volume effect. The longitudinal view (left) shows two rods that partially intersect the scanned slice. The trans-axial image (right) shows dark streaks connecting the rods.*

detector. This is addressed in [45, 47, 60, 64, 131]. Figure 3.22 shows an example of two rods that partially intersect the scanned slice. The strongest gradients occur for projection lines that pass through both rods. The trans-axial image shows a dark streak connecting both rods. Figure 3.23 shows an example of two rods that partially intersect the scanned slice, but now from opposite sides. The gradients will now compensate each other only along projection lines that pass through both rods, while for all other projection lines the error is still present. The trans-axial image shows a bright streak connecting both rods. This is the result of a negative error over the entire image, except between the rods.

Some simple simulations (not shown) showed that axial gradients also cause severe artifacts. We chose to focus on the tNLPV effect first; reduction of the axial NLPV effect is beyond the scope of this thesis. Equivalently, we limited ourselves to metal artifacts in the absence of axial gradients or using infinitely thin slices. The axial NLPV effect is essentially very similar to the tNLPV effect, and we expect that the extension to the axial NLPV effect will be relatively straightforward. However, unlike the tNLPV effect, the axial NLPV effect requires 3D algorithms, resulting in much larger computation times.

3.4.4 Scatter

Many photons that penetrate an object are subject to Compton scatter (see section 2.3.2). They are deviated from their original direction. Obviously, these photons are useless for the reconstruction, and care must be taken that they don't

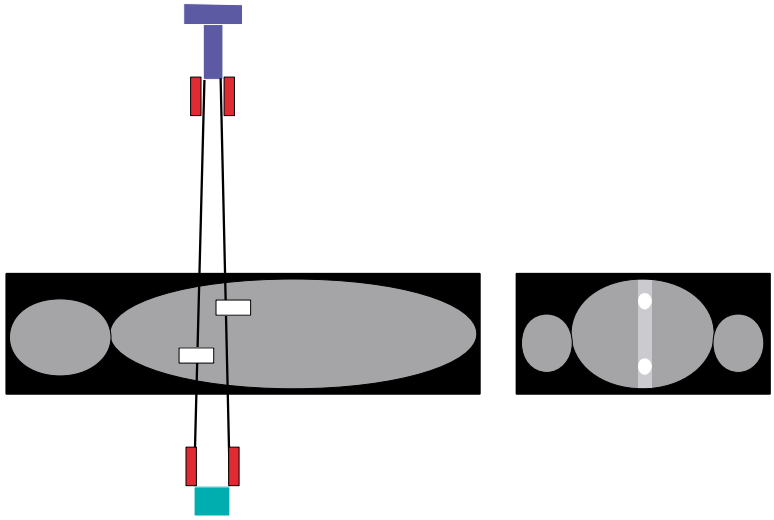

Figure 3.23: *Schematic example of the axial non-linear partial volume effect. The longitudinal view (left) shows two rods that partially intersect the scanned slice from opposite sides. The trans-axial image (right) shows bright streaks connecting the rods.*

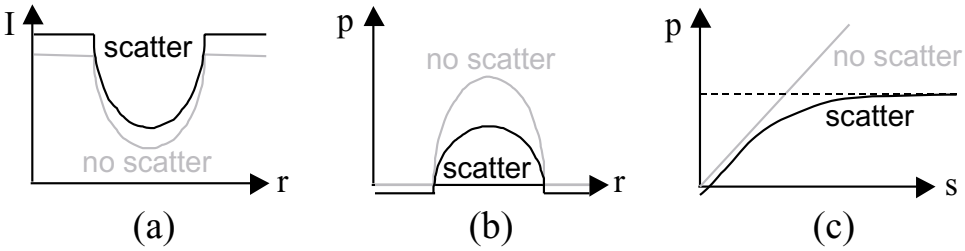

Figure 3.24: *Schematic representation of measurements with and without scatter: (a) intensity profile, (b) attenuation profile (projection), and (c) projection value as a function of path length.*

contaminate the measurement. This is achieved by post-patient collimation and by septa between the detector elements. Nevertheless, a portion of the measurement will still be made up of scattered photons. As the directional information of these photons is largely lost in the scattering process, scatter profiles will be relatively smooth. Sometimes the scatter contribution is even approximated by a constant [43]. Figure 3.24 depicts schematically what happens: (a) shows a measured intensity profile and (b) shows a measured projection, both as a function of r. In the intensity profile, the scatter contribution results in a simple addition of a constant I_{sc}. The relative error will of course be small for rays with little or no attenuation, and large for rays with high attenuation. Accordingly, the (negative) error in

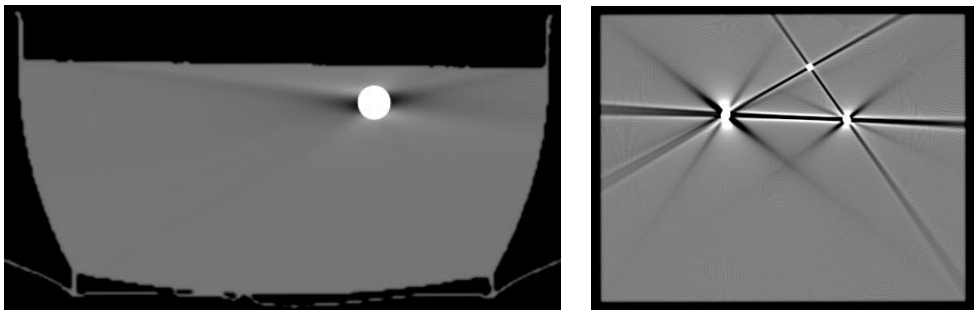

(a) (b)

Figure 3.25: *Simulations with scatter: (a) phantom 1 and (b) phantom 2.*

the projection profile will be larger for high attenuation. (c) shows the projection value as a function of path length s through the absorber material. Similar to beam hardening, the projection value is a non-linear function of path length [43, 76]. This curve even has an upper limit, as there is always a minimum number of (scattered) photons reaching the detectors: $p_{\max} = \ln(I_0/I_{\text{sc}})$. Due to the non-linear behaviour, the qualitative nature of the scatter artifacts is similar to beam hardening. Streaks in the direction of highest attenuation and cupping are the most prominent artifacts.

The effect of scatter was investigated by choosing a constant scatter intensity equal to 0.0001 times the blank scan I_0. Assuming a blank scan value of 10^6 photons per detector element (t.i. the number of photons detected in the absence of absorber), the number of scattered photons per detector element would be 100. Figure 3.25 shows the simulations with added constant-level scatter. For phantom 1, we observe dark streaks in the directions of highest attenuation. Again, also cupping is present but not visible with the current windowing. For phantom 2, additional streaks connecting the metal objects are seen. Even a very small scatter fraction causes significant streaks. Also some bright streaks are present bordering the dark streaks. They originate from the negative values in the reconstruction kernel, and they compensate the negative values from the dark streaks.

3.4.5 Motion

Several types of object motion exist: continuous motion, pulsating motion, discrete motion. All types of motion have in common that they cause inconsistencies in the measurements, but different types of motion cause different types of artifact. Motion artifacts were investigated, by combining two simulations of phantom 1. The iron rod was positioned at two slightly different positions (1.4 mm apart). A new sinogram was obtained by merging a subset of views from the first simulation with a subset of views from the second simulation, as shown in figure 3.26 (a). Figure 3.26 (b) shows the reconstruction for phantom 1. The indices 1, 2, 3, and 4 indicate the positions of the tube at the beginning and end of both subsets. Streaks connect the moving object and the position of the focal spot at the moment of the

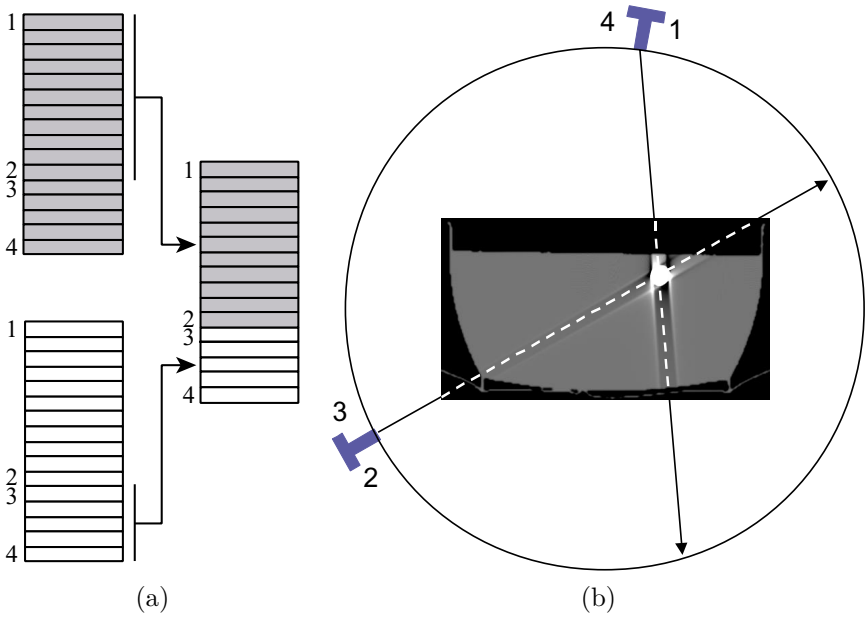

Figure 3.26: *(a) Object motion is simulated by merging sinogram parts from two simulations, with the moving object at two slightly different positions. (b) Reconstruction of phantom 1 with motion of the iron rod. Streaks connect the moving object and the position of the focal spot at the moment of the object motion and at the beginning (or end) of the scan.*

object motion (between view 2 and view 3) and at the beginning (or end) of the scan (between view 4 and view 1). These are the two places corresponding to an inconsistency. For simulating a continuous object motion, this method could be repeated a large number of times for slightly different object positions. A detailed study of motion artifacts is beyond the scope of this work. Ever increasing acquisition speed decreases the probability of motion artifacts. Therefore, we limited ourselves to metal artifacts in the absence of motion.

3.4.6 Aliasing

When samples are taken from a continuous signal, care must be taken to avoid aliasing. The Nyquist criterion states that the sampling frequency must be at least twice the highest frequency in the continuous signal. In CT, it is not straightforward to determine the minimum number of views and detector readouts. They depend on several factors, such as the scanned object, the beam width, the used reconstruction kernel, ... [8, 9, 22, 41, 70, 73, 77, 133, 142, 150]. In practice, aliasing artifacts are always present, at least at a very low level. Several approaches exist to reduce aliasing artifacts: quarter detector offset (section 3.2), flying focal spot (the focal spot is making a sinusoidal movement in order to improve sampling), or applying a

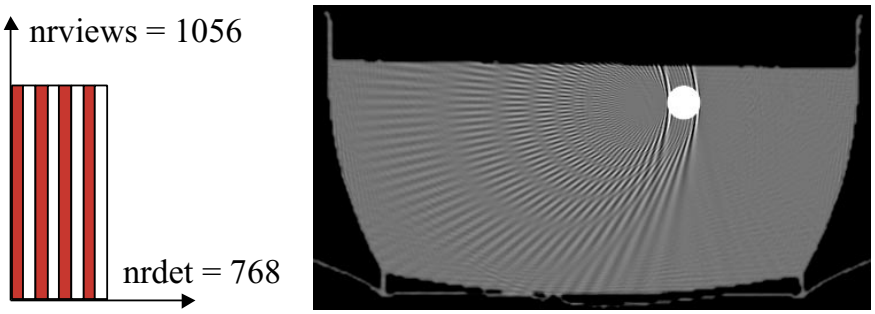

(a) (b)

Figure 3.27: *Throwing away measurements from every second detector element (a) results in severe detector aliasing streaks (b).*

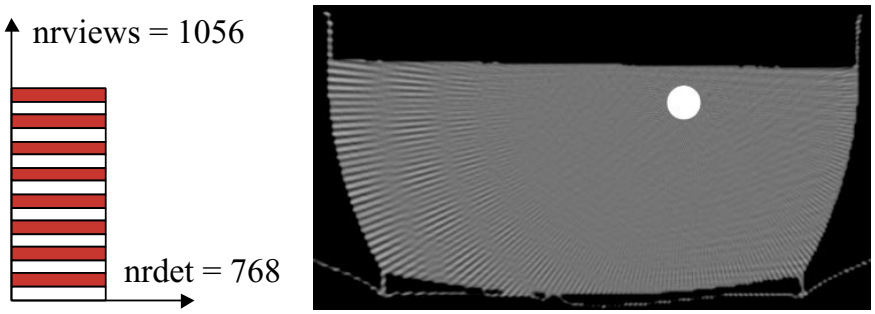

(a) (b)

Figure 3.28: *Throwing away measurements at every fourth view angle (a) results in severe view aliasing streaks (b).*

low-pass filter to the measurements before reconstruction.

We investigated aliasing artifacts by using only a subset of the data from an artifact-free simulation and reconstructing this reduced data set. Figure 3.27 shows a simulation of phantom 1 using only half of the detectors for the reconstruction. Clearly, typical artifacts due to detector under-sampling (circular patterns tangent to sharp edges) are seen. Similarly, figure 3.28 shows a simulation of phantom 1 using only a quarter of the views for the reconstruction. Again typical artifacts due to view under-sampling (streaks starting at a certain distance from the center) are observed. Note that even in the 'artifact-free' simulations (figure 3.11), aliasing errors (such as Moiré patterns) are present, but they are hardly visible with the current windowing. This allows to conclude that - with respect to metal artifacts - aliasing is less important than beam hardening, noise, scatter, and the NLPV effect.

3.5 Conclusion

In this chapter, a high-resolution 2D CT-simulator was presented and validated. The simulator allowed us to estimate a number of parameters such as detector cross-talk and afterglow. Very realistic simulations are obtained. We focussed on one type of CT-scanner, but the simulator is easily applicable to different geometries, for instance to micro-CT-scanners [12]. A number of artifacts were studied based on measurements and simulations. Although we based ourselves on one specific scanner type, the physical processes behind the studied artifacts are very general and the conclusions apply to all modern CT-scanners. We have shown that all investigated causes of streaks are effectively able to produce streaks. The most important causes of metal artifacts were found to be noise, beam hardening, the NLPV effect, and scatter. In the absence of metal objects all these effects still result in artifacts, but to a lesser extent. Both motion artifacts and artifacts due to axial gradients need further attention but are beyond the scope of this thesis.

. . . iterative reconstruction . . .

Chapter 4

Iterative reconstruction

4.1 Introduction

In section 2.5 we described direct Fourier reconstruction and reconstruction by filtered backprojection. These are transform methods: they are based on an analytical inversion of the Radon transform and give a one-step solution. If applied to ideal projections, i.e. projections with an infinite number of samples, a vanishing X-ray beam width, and without noise, beam hardening, scatter or other imperfections, then these algorithms result in an ideal reconstruction. In practice, the continuous formulation of these algorithms is discretized, allowing to calculate a discrete image from a discrete set of projection values.

A totally different approach is used in iterative reconstruction. Here, we start from discrete representations of both the image and the measurement. An image, say $\mu(x, y)$, is written as a finite linear combination of base functions $f_j(x, y)$:

$$\mu(x, y) = \sum_{j=1}^{J} \mu_j \cdot f_j(x, y). \tag{4.1}$$

The most obvious solution is to use a square pixel basis. In this case μ_j represents the value of pixel j, and $f_j(x, y) = 1$ within the support of pixel j and 0 elsewhere. However, many other approaches exist, such as the method of sieves [139, 140], spherically symmetric volume elements [95], and natural pixels [65]. We use the vector $\vec{\mu}$ to denote the set of pixel values $\{\mu_j\}_{j=1}^{J}$, and $\vec{y}$ to denote the measurements $\{y_i\}_{i=1}^{I}$.

Based on this representation, we can define a discrete forward model of the acquisition. Given an image $\vec{\mu}$, the expected number of detected photons can be written as

$$\hat{y}_i = b_i \cdot \exp(-\sum_{j=1}^{J} l_{ij}\mu_j), \tag{4.2}$$

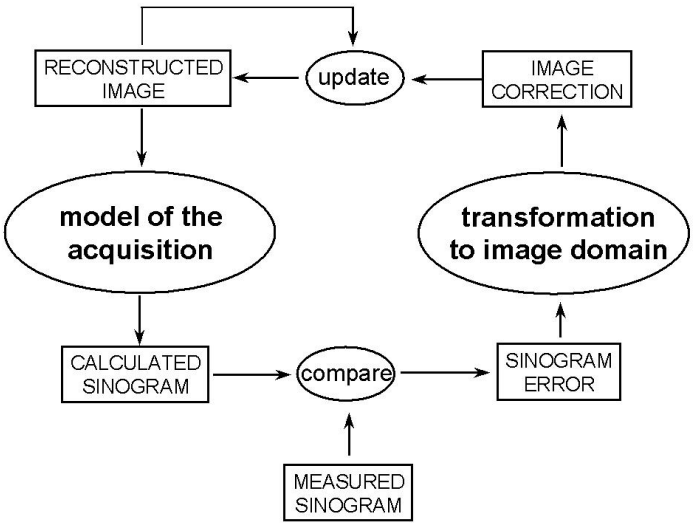

Figure 4.1: *General iterative reconstruction scheme. Starting from the current reconstruction, a sinogram is calculated. A measure for the sinogram error is transformed to the image domain. The reconstruction is updated in a way that reduces the sinogram error.*

where b_i is the number of photons that would be detected in the absence of absorber (blank scan), and l_{ij} is the effective intersection length of projection line i with pixel j (see section 3.2). b_i is usually obtained by a calibration scan.

In reality, the measurements y_i deviate from their expected values due to statistical fluctuations (see section 3.4.1). We could neglect this error and approximate $\hat{y}_i$ by y_i. $\vec{\mu}$ can then be estimated by solving eq.(4.2). This comes down to solving a set of I equations in J unknowns. The most common approach to do this, is to divide both sides of eq.(4.2) by b_i, take the logarithm, and apply a transform method (see section 2.5) to invert the Radon transform. Usually, an exact solution does not exist or is not acceptable, for instance because it is too noisy. Transform methods try to accommodate for this be filtering out the highest frequencies before reconstruction (see chapter 2).

In iterative reconstruction, the deviation of y_i from $\hat{y}_i$ is really taken into account, usually by using a statistical model to describing y_i as a function of $\hat{y}_i$. The reconstruction problem is tackled in two steps. First, an objective function is defined, and second, this objective function is optimized. Many different objective functions exist (e.g. minimum least squares error, maximum likelihood, ...) and many different ways to optimize these objective functions (steepest ascent, conjugate gradients, ...). Usually, this results in an iterative optimization algorithm with an update scheme like in figure 4.1. Starting from an initial – often blank – image, the corresponding sinogram is calculated. The calculated sinogram is compared to the measured sinogram. The sinogram error is transformed back to the image

domain and subtracted from the current reconstruction. This process is repeated a number of times until a good reconstruction is obtained.

Although widely used in nuclear medicine (PET and SPECT), iterative reconstruction has not yet penetrated in CT. The main reason for this is that data sets in CT are much larger than in nuclear medicine, and iterative reconstruction then becomes computationally very intensive. Compared to filtered backprojection, which is currently the standard reconstruction method in CT, computation times in iterative reconstruction are easily 10 to 1000 times higher. Furthermore, many iterative algorithms have a statistical basis. Count rates are much lower in nuclear medicine, resulting in increased noise. This explains the stronger need for a statistical approach in nuclear medicine. However, iterative reconstruction is promising for some specific topics in CT, such as artifact reduction and low dose CT, and ever increasing computer capacity is bringing iterative reconstruction within reach.

In this chapter we discuss the aspects of the maximum likelihood approach in transmission tomography that are most relevant for this thesis. Section 4.2 describes the general approach. Section 4.3 describes the ML-TR algorithm, which forms the base of all iterative reconstruction algorithms presented in chapter 5. Section 4.8 describes the implementation, and the projector-backprojector in particular. Finally, section 4.9 presents a simulation study (based on [109]) that investigates the possible benefit of iterative methods for CT.

4.2 Maximum likelihood for transmission tomography

The basic idea of the maximum a posteriori (MAP) approach is the following: given a set of transmission measurements $\vec{y}$, find the distribution of linear attenuation coefficients $\vec{\mu}$ that maximizes the probability $P(\vec{\mu}|\vec{y})$. Bayes rule states:

$$P(\vec{\mu}|\vec{y}) = \frac{P(\vec{y}|\vec{\mu}) \cdot P(\vec{\mu})}{P(\vec{y})}. \tag{4.3}$$

The term $P(\vec{y})$ is independent of $\vec{\mu}$ and can therefore be omitted. The term $P(\vec{\mu})$ contains prior information about the image (see section 4.6). If no prior information is available, the problem reduces to optimizing $P(\vec{y}|\vec{\mu})$, which is called the *maximum-likelihood (ML)* approach [92, 105, 128, 129, 137]. As the statistical variations on the measurements y_i are mutually independent, P can be factorized:

$$P(\vec{y}|\vec{\mu}) = \prod_{i=1}^{I} P(y_i|\vec{\mu}). \tag{4.4}$$

Instead of optimizing this expression, we can also optimize its logarithm, as the logarithm is a monotonic function. This results in the *log-likelihood* (logarithm of

the likelihood):

$$\ln P(\vec{y}|\vec{\mu}) = \sum_{i=1}^{I} \ln P(y_i|\vec{\mu}). \tag{4.5}$$

It is usually assumed that the main source of uncertainty results from the quantum nature of the X-ray photons (quantum noise), and therefore that the photon counts are Poisson-distributed [48, 63]. A Poisson distribution y with mean $\hat{y}$ is described by

$$P(y|\hat{y}) = \frac{\hat{y}^y e^{-\hat{y}}}{y!}. \tag{4.6}$$

As the probability of measuring y_i depends only on its expected value $\hat{y}_i$ based on the image $\vec{\mu}$, we have

$$P(y_i|\vec{\mu}) = P(y_i|\hat{y}_i). \tag{4.7}$$

Combining equations (4.5), (4.6) and (4.7), and omitting the constant term, we obtain the following objective function:

$$L = \sum_{i=1}^{I} \big(y_i \cdot \ln \hat{y}_i - \hat{y}_i\big). \tag{4.8}$$

Given a distribution $\vec{\mu}$ of the linear attenuation coefficient, we need a model of the acquisition to calculate $\hat{y}_i$, the expected value of y_i. A simple acquisition model for transmission tomography is given by eq.(4.2). The aim is now to find a distribution $\vec{\mu}$ that maximizes

$$L = \sum_{i=1}^{I} \Big(y_i \cdot \ln \big(b_i \cdot \exp(-\sum_{j=1}^{J} l_{ij}\mu_j)\big) - b_i \cdot \exp(-\sum_{j=1}^{J} l_{ij}\mu_j)\Big). \tag{4.9}$$

Unlike in emission tomography, the unknowns μ_j are inside an exponential, which makes optimization less trivial. One possible solution is to apply the expectation maximization method [30]. The maximization step leads to a transcendental equation, which can be solved by approximation as a truncated series expansion [92]. This results in complex iterations and requires a dedicated projector/backprojector.

4.3 ML-TR

A simple gradient ascent algorithm was proposed by Nuyts et al [25, 109, 110]: Given the current reconstruction $\vec{\mu}^n$, L is approximated by a truncated series expansion:

$$\begin{aligned} L(\vec{\mu}) = &\simeq T_1(\vec{\mu};\vec{\mu}^n) \\ &= L(\vec{\mu}^n) + \sum_{j=1}^{J} \frac{\partial L}{\partial \mu_j}\Big|_{\vec{\mu}^n} (\mu_j - \mu_j^n) \\ &\quad + \sum_{j=1}^{J}\sum_{h=1}^{J} \frac{1}{2} \frac{\partial^2 L}{\partial \mu_j \partial \mu_h}\Big|_{\vec{\mu}^n} (\mu_j - \mu_j^n)(\mu_h - \mu_h^n). \end{aligned} \tag{4.10}$$

Because the second derivatives of L are always negative and because

$$2(\mu_j - \mu_j^n)(\mu_h - \mu_h^n) \leq (\mu_j - \mu_j^n)^2 + (\mu_h - \mu_h^n)^2, \tag{4.11}$$

it follows that

$$\begin{aligned} &\sum_{j=1}^{J}\sum_{h=1}^{J} \frac{1}{2} \frac{\partial^2 L}{\partial \mu_j \partial \mu_h}\Big|_{\vec{\mu}^n} (\mu_j - \mu_j^n)(\mu_h - \mu_h^n) \\ \geq &\sum_{j=1}^{J}\sum_{h=1}^{J} \frac{1}{2} \frac{\partial^2 L}{\partial \mu_j \partial \mu_h}\Big|_{\vec{\mu}^n} (\mu_j - \mu_j^n)^2. \end{aligned} \tag{4.12}$$

This allows the introduction of a function T_2 in which the variables are separated:

$$\begin{aligned} T_1(\vec{\mu};\vec{\mu}^n) &\geq T_2(\vec{\mu};\vec{\mu}^n) \\ &= L(\vec{\mu}^n) + \sum_{j=1}^{J} \frac{\partial L}{\partial \mu_j}\Big|_{\vec{\mu}^n} (\mu_j - \mu_j^n) \\ &\quad + \sum_{j=1}^{J}\sum_{h=1}^{J} \frac{1}{2} \frac{\partial^2 L}{\partial \mu_j \partial \mu_h}\Big|_{\vec{\mu}^n} (\mu_j - \mu_j^n)^2. \end{aligned} \tag{4.13}$$

Thus we obtain the following relations:

$$\begin{aligned} L(\vec{\mu}^n) &= T_1(\vec{\mu}^n;\vec{\mu}^n) &= T_2(\vec{\mu}^n;\vec{\mu}^n) \\ L(\vec{\mu}) &\simeq T_1(\vec{\mu};\vec{\mu}^n) &\geq T_2(\vec{\mu};\vec{\mu}^n). \end{aligned} \tag{4.14}$$

Consequently, an iteration that updates $\vec{\mu}^n$ to $\vec{\mu}$ by maximizing T_2, increases T_1 (unless $\vec{\mu} = \vec{\mu}^n$) and should increase L if the quadratic approximation (4.10) is sufficiently accurate. Maximizing the quadratic function T_2 is trivial since each term depends on exactly one variable μ_j. Setting the derivatives with respect to μ_j to zero yields:

$$\mu_j = \mu_j^n - \frac{\frac{\partial \mathrm{L}}{\partial \mu_j}\Big|_{\vec{\mu}^n}}{\sum_{h=1}^{J} \frac{\partial^2 \mathrm{L}}{\partial \mu_j \partial \mu_h}\Big|_{\vec{\mu}^n}}. \tag{4.15}$$

Substituting eq.(4.8) in eq.(4.15) results in the following update step:

$$\mu_j^{n+1} = \mu_j^n + \frac{\sum_{i=1}^{I} l_{ij} \cdot (\hat{y}_i - y_i)}{\sum_{i=1}^{I} l_{ij} \cdot \left[\sum_{h=1}^{J} l_{ih}\right] \cdot \hat{y}_i}, \tag{4.16}$$

where $\hat{y}_i$ is given by eq.(4.2). The sinogram error $(\hat{y}_i - y_i)$ is backprojected, divided by the backprojection of a scaled version of the calculated sinogram, and added to the current reconstruction. This is called the *ML-TR* (Maximum-Likelihood for TRansmission) algorithm. A very similar update step is obtained for emission tomography [113]. ML-TR forms the basis of all iterative algorithms discussed further in this work.

4.4 Alternative derivation

Fessler et al [38] have derived a class of algorithms that monotonically increase the likelihood. The likelihood is optimized by using surrogate functions similar to De Pierro [28, 29] and by applying Jensen's inequality. ML-TR appears to be a member of that class of algorithms, by omitting the scatter term, omitting the prior, updating all pixels simultaneously, and choosing $\alpha_{ij} = l_{ij} / \sum_{h=1}^{J} l_{ih}$ (see section IV.A of [38]). Note that in [38], the calculated sinogram $\hat{y}_i$ is approximated by the measured sinogram y_i in the denominator. The advantage is that one can then precompute the denominator prior to iterating. In the neighborhood of the optimum, both formulas are equivalent. If however the initial estimate is far from the optimal solution, the approximation leads to slower convergence. We have not applied this approximation.

In what follows we repeat the derivation of [38], using our particular assumptions. First define $h_i(p)$ as

$$h_i(p) = y_i \ln\left(b_i e^{-p}\right) - b_i e^{-p} \tag{4.17}$$

so that the objective function eq.(4.9) can be written as

$$L = \sum_{i=1}^{I} h_i\Big(\sum_{j=1}^{J} l_{ij}\mu_j\Big). \tag{4.18}$$

The key step is to note that

$$\sum_{j=1}^{J} l_{ij}\mu_j = \sum_{j=1}^{J} \frac{l_{ij}}{\sum_{h=1}^{J} l_{ih}} \cdot \Big[\Big(\sum_{h=1}^{J} l_{ih}\Big)(\mu_j - \mu_j^n) + \sum_{h=1}^{J} l_{ih}\mu_h^n\Big]. \tag{4.19}$$

Jensen's inequality states that for a function $f(x)$ which is convex over a region R, and a set of values $\{x_i | x_i \in R\}$:

$$E\{f(x_i)\} \leq f(E\{x_i\}), \tag{4.20}$$

or the mean of the function f is smaller than or equal to the function f of the mean. Substituting eq.(4.19) in eq.(4.18), and applying Jensen's inequality (as h_i is convex), gives

$$\begin{aligned} L(\vec{\mu}) &\geq Q(\vec{\mu};\vec{\mu}^n) \\ &= \sum_{j=1}^{J}\sum_{i=1}^{I} \frac{l_{ij}}{\sum_{h=1}^{J} l_{ih}} \cdot h_i\Big((\sum_{h=1}^{J} l_{ih})(\mu_j - \mu_j^n) + \sum_{h=1}^{J} l_{ih}\mu_h^n\Big) \end{aligned} \tag{4.21}$$

and

$$L(\vec{\mu}^n) = Q(\vec{\mu}^n;\vec{\mu}^n). \tag{4.22}$$

According to De Pierro's optimization transfer idea [28, 29], we can now maximize the surrogate function $Q(\vec{\mu};\vec{\mu}^n)$ in order to try to maximize $L(\vec{\mu})$. This is a 1D optimization problem, which is solved numerically using Newton-Raphson's method:

$$\mu_j^{n+1} = \mu_j^n + \frac{\frac{\partial Q(\vec{\mu};\vec{\mu}^n)}{\partial \mu_j}\Big|_{\vec{\mu}^n}}{-\frac{\partial^2 Q(\vec{\mu};\vec{\mu}^n)}{\partial \mu_j^2}\Big|_{\vec{\mu}^n}}. \tag{4.23}$$

Comparing $\frac{\partial Q(\vec{\mu};\vec{\mu}^n)}{\partial \mu_j}\big|_{\vec{\mu}^n}$ and $\frac{\partial^2 Q(\vec{\mu};\vec{\mu}^n)}{\partial \mu_j^2}\big|_{\vec{\mu}^n}$ with $\frac{\partial L(\vec{\mu})}{\partial \mu_j}\big|_{\vec{\mu}^n}$ and $\frac{\partial^2 L(\vec{\mu})}{\partial \mu_j^2}\big|_{\vec{\mu}^n}$ respectively shows that eq.(4.23) and eq.(4.15) are equivalent.

4.5 Scatter

Iterative reconstruction algorithms can easily be adapted to take into account scatter. If a scatter estimate is available (from a measurement or a simulation), instead of subtracting it from the measurements, it can be used as an input of the reconstruction algorithm. This approach is routinely used in nuclear medicine, where the scatter can be estimated more easily thanks to the energy-discriminating detectors. It has the advantage that the noise characteristics of the scatter itself are taken into account. We now show how ML-TR is adapted to take into account scatter. The acquisition model of eq.(4.2) is extended with a *known* scatter term S_i:

$$\hat{y}_i = b_i \cdot \exp(-\sum_{j=1}^{J} l_{ij}\mu_j) + S_i. \tag{4.24}$$

Following the same derivation as in section 4.3, the following update formula is obtained

$$\mu_j^{n+1} = \mu_j^n + \frac{\sum_{i=1}^{I} l_{ij} \cdot \frac{\hat{y}_i - S_i}{\hat{y}_i} \cdot (\hat{y}_i - y_i)}{\sum_{i=1}^{I} l_{ij} \cdot \big[\sum_{h=1}^{J} l_{ih}\big] \cdot (\hat{y}_i - S_i) \cdot \big(1 - \frac{y_i S_i}{\hat{y}_i^2}\big)}, \tag{4.25}$$

where $\hat{y}_i$ is now given by eq.(4.24). Note that eq.(4.16) can be seen as a special case of eq.(4.25), by assuming $S_i \equiv 0$.

4.6 Gibbs priors

The maximum-likelihood approach has the drawback that images become increasingly non-smooth as the iteration number increases, in particular when the measurements are very noisy. This can be solved by post-smoothing the image, at the expense of spatial resolution. Other authors propose to initialize the algorithm with a smooth estimate and to terminate the algorithm before convergence [97]. Another solution consists in choosing smoother basis functions instead of square pixels (see above). Many authors use a MAP approach based on Markov Random Field (MRF) Gibbs priors [42, 51, 106]. We explain this method in more detail.

In section 4.2 it was assumed that no prior information is available, in which case the MAP estimation reduces to ML estimation. We now consider the case were the factor $P(\vec{\mu})$ is not constant. We use the following MRF Gibbs prior

$$P(\vec{\mu}) = \frac{1}{Z} \exp\Big(-\beta \sum_{j=1}^{J} \sum_{h=1}^{J} w_{jh} V(\mu_h - \mu_j) \Big), \tag{4.26}$$

where β is a parameter that influences the degree of smoothness of the estimated images and Z is a normalizing constant. V is the potential function. w_{jh} is inversely proportional to the Euclidean distance between pixels j and h, and is zero if $h = j$ or $h \notin N_j$. N_j denotes the set of neighbors of pixel j. Several choices exist for the potential function. The quadratic function

$$V(\mu) = \mu^2 \tag{4.27}$$

penalizes large differences. Geman and McClure [42] proposed the function

$$V(\mu) = \frac{\mu^2}{\delta^2 + \mu^2}, \tag{4.28}$$

where δ is a positive constant. This function goes asymptotically to 1 and prevents that large differences (which are likely to occur around edges) are considered too unlikely. This function is not convex and therefore can lead to local maxima. Others prefer to use the Huber function [106, 112]

$$V(\mu) = \begin{cases} \frac{\mu^2}{2\delta^2} & \text{for } |\mu| \leqslant \delta \\ \frac{|\mu| - \delta/2}{\delta} & \text{for } |\mu| \geqslant \delta, \end{cases} \tag{4.29}$$

where δ is a positive constant. This function becomes linear in μ for $|\mu| \geqslant \delta$ and is a compromise between the two previous choices. It is relatively edge-preserving (like the Geman prior) and it is convex (like the quadratic prior). Convexity has the advantage that the prior does not introduce local maxima [37].

Substituting eq.(4.26) in eq.(4.3) leads to the following objective function:

$$L = \sum_{i=1}^{I} \big(y_i \cdot \ln \hat{y}_i - \hat{y}_i \big) - \beta \sum_{j=1}^{J} \sum_{h=1}^{J} w_{jh} V(\mu_h - \mu_j). \tag{4.30}$$

Applying update step (4.15), the following MAP algorithm is obtained:

$$\mu_j^{n+1} = \mu_j^n + \frac{\sum_{i=1}^{I} l_{ij} \cdot (\hat{y}_i - y_i) + \beta \sum_{h=1}^{J} \frac{\partial V}{\partial \mu}(\mu_h - \mu_j)}{\sum_{i=1}^{I} l_{ij} \cdot \left[\sum_{h=1}^{J} l_{ih}\right] \cdot \hat{y}_i}. \tag{4.31}$$

A more conservative update step is given by

$$\mu_j^{n+1} = \mu_j^n + \frac{\sum_{i=1}^{I} l_{ij} \cdot (\hat{y}_i - y_i) + \beta \sum_{h=1}^{J} \frac{\partial V}{\partial \mu}(\mu_h - \mu_j)}{\sum_{i=1}^{I} l_{ij} \cdot \left[\sum_{h=1}^{J} l_{ih}\right] \cdot \hat{y}_i + \beta \sum_{h=1}^{J} \frac{\partial^2 V}{\partial \mu^2}(\mu_h - \mu_j)}. \tag{4.32}$$

If the prior term is relatively important (e.g. large β), than this version is more stable.

4.7 Ordered subsets

Hudson and Larkin invented the method of ordered subsets (OS) [67], which dramatically increases the speed of the ML-EM (maximum likelihood expectation maximization) algorithm [137]. A very similar approach is formed by the block-iterative versions [13, 14, 15] of the simultaneous multiplicative algebraic reconstruction technique (MART) and ML-EM.

The OS method groups projection data into an ordered sequence of subsets. An iteration of ordered subsets is defined as a single pass through all the subsets, in each subset using the current reconstruction to calculate the update step with that data subset. The convergence of OS is guaranteed only if an exact solution exists (a reconstruction so that $\hat{y}_i \equiv y_i$). If no exact solution exists, OS results in a limit cycle [14]. Convergence can be enforced by using under-relaxation [11] or by adapting the projection data once a limit cycle is reached [14]. Several authors have adapted the OS method for transmission tomography [36, 85]. We apply it to ML-TR, yielding ML-OSTR [109].

One important parameter in OS is the choice of subsets. Hudson and Larkin [67] make a distinction between:

non-overlapping subsets: all subsets are mutually exclusive and their union equals the complete set of projection data.

cumulative subsets: every subset is contained within the following subset.

standard: there is only one subset containing all the projection data, this is equivalent to not using OS.

In this work we always use the following guidelines for defining subsets:

- The subsets are non-overlapping.
- The number of subsets is decreased as iteration number increases (for improved convergence).

- The views within one subset are equally spaced.
- Consecutive subsets are mutually as different as possible (e.g. by choosing the views midway between these in the previous subset).

4.8 Practical implementation

All reconstruction algorithms discussed in this work are implemented in IDL. The projection and backprojection, which form the core of all iterative algorithms, are implemented in C for faster computation. A parallel-beam projector-backprojector is available [111], which was developed for nuclear medicine (PET, SPECT). However, in modern CT-scanners, the acquired data are not ordered in parallel subsets but in fans. Therefore, two approaches were followed:

- A rebinner was implemented to convert fan-beam data into parallel-beam data (and vice versa) (see section 2.5.5). This allowed us to re-use the parallel-beam projector-backprojector and all inherently parallel-beam algorithms.
- A fan-beam projector-backprojector was implemented, allowing to use dedicated fan-beam reconstruction algorithms.

Both methods gave comparable results for FBP. In the remainder of this thesis, the second approach is used, unless where stated differently. A pixel-driven backprojector – used for FBP – is described in section 2.5.1. The fan-beam projector and backprojector used in iterative reconstruction are ray-driven: the (back-)projection of one single line is performed for all sinogram pixels. The projection is described in section 3.2. The corresponding ray-driven backprojector (figure 4.2) performs the transpose operation. The backprojected value is added to all pixels that are adjacent to projection line i, using a multiplication with l_{ij}.

4.9 Iterative reconstruction for CT

4.9.1 Introduction

This section is based on [109] and presents a simulation study that investigates the possible benefit of iterative methods for spiral CT (see section 2.6), regardless of any speed considerations. In current clinical systems, the 3D sinogram is converted using linear interpolation (see section 2.6) to a set of approximate 2D sinograms, which are reconstructed with filtered backprojection (FBP). If rays coming from opposite directions are also used, this is called 180°-interpolation. However, the interpolation reduces the axial resolution. Moreover, this method is only approximate, and artifacts may be produced in regions with high axial gradients. In this section, iterative reconstruction algorithms for helical CT are derived from two-dimensional reconstruction algorithms, by adapting the projector/backprojector to the helical orbit of the source, and by constraining the axial frequencies with a Gaussian sieve [139, 140].

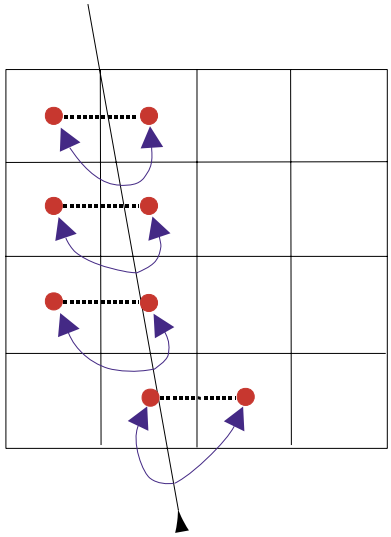

Figure 4.2: *The ray-driven backprojector performs the transpose operation of the ray-driven projector described in chapter 3. The backprojected value is multiplied with the row/column intersection length and added to all pixels that are adjacent to the (back)projection line, using linear interpolation.*

4.9.2 Reconstruction algorithms

The following algorithms have been included in this study:

- NN180: 180° nearest neighbor interpolation FBP
- LIN180: 180° linear interpolation FBP
- ILIN180: iterated 180° linear interpolation FBP
- ML-EM
- ML-TR

The first two methods are included for comparison. LIN180 is the current standard in clinical practice. NN180 produces better axial resolution, but at the cost of more severe reconstruction artifacts near axial gradients. ILIN180 is a heuristic algorithm based on iterative filtered backprojection [123], which is expected to converge faster than the maximum likelihood methods. ML-TR treats the transmission data as realizations from a Poisson distribution. ML-EM, on the other hand, is designed for emission tomography, and treats the log-converted sinograms as Poisson data. This assumption is wrong. However, ML-EM is known to be a robust algorithm (at least at low iterations numbers): it is less sensitive to inconsistencies in the sinograms than e.g. FBP. Comparison between ML-TR and ML-EM is of

interest, since it helps to find out whether the power of the ML-method is in its robustness or in its accurate noise model.

In the FBP-based methods (NN180, LIN180, ILIN180), the high frequency noise is suppressed by convolving the reconstructed slices with a 2D Gaussian convolution mask. In the iterative methods (ILIN180, ML-EM, ML-TR), noise is suppressed by stopping the iterations before convergence is obtained. For NN180 and LIN180, the standard deviation of the Gaussian smoothing is varied from 0 to 3 pixels. For ML-EM and ML-TR, the number of iterations is varied. For ILIN180, both the number of iterations and the width of the Gaussian mask are varied.

Because of the helical orbit and because of the finite slice thickness, the measurement has a limited axial resolution. As the number of reconstructed planes is arbitrary, axial constraining is required. Therefore, we use the method of sieves [139, 140]. We defined an axial sieve S according to

$$S = \{\mu : \mu(x,y,z) = \int_z K(z)\mu'(x,y,z)dz\}, \tag{4.33}$$

where $K(z)$ is the Gaussian sieve kernel. In practice, prior to each projection and after each backprojection, a convolution with the sieve kernel is applied. The resulting reconstruction must be convolved with the sieve to produce the final image. In this study, the full width at half maximum of the sieve was set equal to the width of the rectangular axial point spread function of the simulated scanner. Another option would be to use ellipsoidally symmetric volume elements as in [95].

In the iterative reconstruction algorithms, the axial point spread function (PSF) is taken into account in an approximate way. In each iteration, the reconstructed images are convolved with the axial PSF (before projection and after backprojection). This is an approximation: because in reality, axial blurring occurs during detection of the photons.

Evaluation is done qualitatively by visual inspection, and quantitatively by computing bias-noise curves for each algorithm. Bias and noise in a region R are computed as:

$$\text{Bias: } \sqrt{\frac{\sum_{j\in R}(\mu_j^{\text{nonoise}} - \mu_j^{\text{ideal}})^2}{M}} \qquad \text{noise: } \sqrt{\frac{\sum_{j\in R}(\mu_j^{\text{noise}} - \mu_j^{\text{nonoise}})^2}{M}} \tag{4.34}$$

where M is the number of pixels in region R, $\vec{\mu}^{\text{nonoise}}$ is the reconstruction of a noise-free simulation, $\vec{\mu}^{\text{ideal}}$ is the reference image, and $\vec{\mu}^{\text{noise}}$ is a reconstruction of noisy data. Lower bias for the same noise (and lower noise for the same bias) is suggestive for more accurate reconstruction.

4.9.3 Simulations

Four software phantoms have been simulated:

1. Phantom 3 (figure 4.3) is a clinical 2D CT image of the thorax, in which the

Figure 4.3: *Phantom 3 is a clinical 2D CT image of the thorax, in which the gray values were replaced by typical attenuation coefficients. Using this 2D simulation is equivalent to testing the algorithms in the case of a phantom that is constant in the z-direction.*

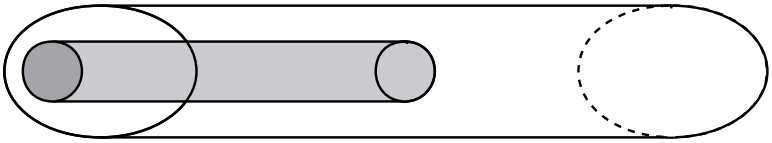

Figure 4.4: *Phantom 4 (figure 4.4) consists of an elliptical attenuating cylinder. This cylinder contains a smaller circular cylinder with 10 % higher attenuation coefficient. The smaller cylinder occupies only half of the axial field of view, thus producing a sharp axial gradient. This phantom is used to study performance near axial gradients, since axial gradients are the dominant source of artifacts in helical CT.*

gray values were replaced by typical attenuation coefficients. Using this 2D simulation is equivalent to testing the algorithms in the case of a phantom that is constant in the z-direction. The image contained 300x300 pixels, there were 300 detectors per angle and 400 projection angles were simulated. For this phantom, NN180 and LIN180 reduce to FBP and ILIN180 to iterative FBP. Projections were computed at twice the resolution as compared to the projection/backprojection in the reconstruction programs (i.e. two projection lines were computed per detector pixel, using twice the number of points per projection line). Finite spatial resolution was simulated by convolving the computed counts with the mask [.25, .5, .25].

2. Phantom 4 (figure 4.4) consists of an elliptical attenuating cylinder. This cylinder contains a smaller circular cylinder with 10 % higher attenuation co-

efficient. The smaller cylinder occupies only half of the axial field of view, thus producing a sharp axial gradient. This phantom is used to study performance near axial gradients, since axial gradients are the dominant source of artifacts in helical CT. Projections were computed analytically as line integrals and finite resolution was simulated with the same convolution mask. Here, the axial PSF was simulated by computing for every angle and every detector 10 projections at different axial position (uniformly sampling the rectangular PSF) and adding the "detected" counts. In the reported results, the axial increment per 180° was 0.9 times the axial (rectangular) PSF-width.

3. Phantom 5 consists of an elliptical attenuating cylinder containing multiple ellipsoids with different attenuation coefficient. The purpose is to verify the findings obtained on the previous two phantoms. Six slices were reconstructed for phantom 4 and 15 for phantom 5, using a slice separation of 0.5 times the axial PSF-width, 150 angles per 180 ° and 120 detectors. Simulation parameters were the same as for phantom 4.

4. Phantom 6 is identical to phantom 3 except for the inclusion of a small region with high attenuation. This phantom is included to study the potential application of iterative algorithms for metal artifact reduction. Simulation parameters were the same as for phantom 3.

For all phantoms, Poisson noise was simulated assuming 10^6 photons per detector prior to attenuation. Poisson noise was approximated as a Gaussian pseudo-random realization, with variance equal to the mean.

4.9.4 Results and discussion

Figure 4.5 (a) shows the resulting bias-noise curves for phantom 3. Note that in the 2D case NN180 and LIN180 both turn into FBP, and ILIN180 turns into iterative FBP. For iterative FBP, one curve per iteration is shown, where the curve is produced using different smoothing masks. Initially, iteration increases noise and decreases bias. At 10 iterations, however, increased bias is observed. For the other algorithms, bias decreases monotonically with iteration number. The bias-noise curves of iterative FBP and FBP overlap, but iterative FBP allows to reach lower bias-values at the cost of increased noise. The maximum likelihood algorithms both produce very similar bias-noise curves, which are slightly better than those of (iterative) FBP. At higher iteration numbers, all images are of high quality and approximately equivalent. These findings suggest that the ML methods perform at least as well as the FBP-methods for nearly ideal data (in the absence of axial gradients or objects with high attenuation). Figure 4.5 (b) illustrates the most common bias-noise behaviour: smoothing decreases the noise but increases the bias, iterations decrease the bias but increase the noise.

Figure 4.6 shows five central reconstructed slices of phantom 4 at similar noise level for each of the algorithms. Figure 4.7 (a) presents the bias-noise curves for a

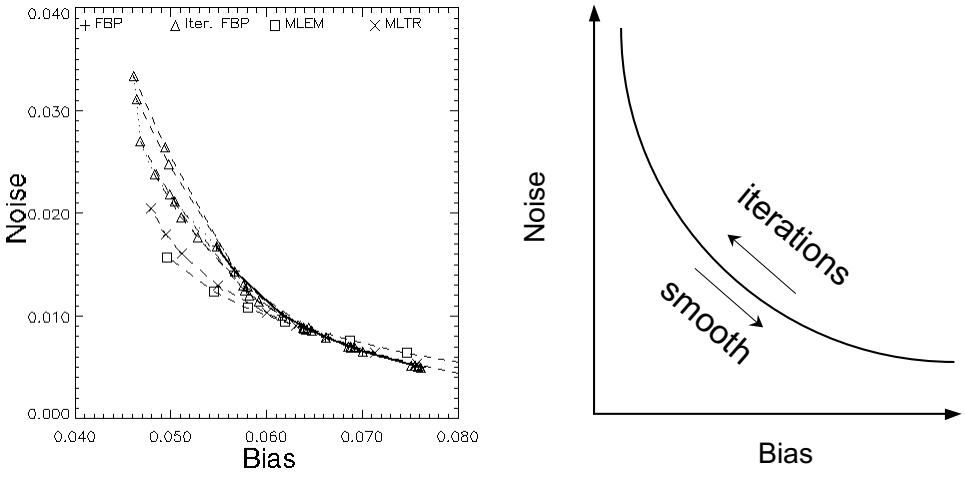

(a) (b)

Figure 4.5: *Phantom 3: (a) bias-noise curves using Gaussian smoothing with $\sigma = 0$, 0.5, 1, 1.5, 2 and 3 pixels for FBP (solid line) and iterative FBP (triangles, dotted line). For iterative FBP, iterations 1, 2, 3, 5, 10, and 15 are shown as independent dashed lines. The points for 15 iterations are connected with a dotted line. Iteration 1 is identical to FBP, shown as a plane line. For ML-EM, iterations 1, 3, 6, 10, 20, 30, 50, 70, 100, and 200 are shown, and for ML-TR also iterations 400, 600, and 1000. (b) Schematic representation of the general bias-noise behaviour. Smoothing decreases the noise but increases the bias. Iterations decrease the bias but increase the noise.*

central region enclosing the central cylinder. When the region encloses the entire elliptical cylinder, the curves of the ML-algorithms shift towards lower bias and lower noise, relative to the other curves (data not shown). Figure 4.7 (b) shows axial profiles, computed as the mean of a region in the center of the small cylinder (shown on top left slice in figure 4.6) as a function of plane position. NN180 has somewhat better axial resolution than LIN180 (figure 4.7 (b)), but with severe artifacts near the gradient (figure 4.6). LIN180 reduces these artifacts at the cost of poorer axial resolution. The iterative methods produce an axial resolution superior to that of NN180 combined with strong artifact reduction. However, a new artifact is introduced: noticeable axial Gibbs undershoots and overshoots show up in slices adjacent to the gradient. The ML-methods also produce in-plane Gibbs overshoots (ringing) at the edges of the outer cylinder. The axial Gibbs over- and undershoots are due to reconstruction of strong gradients without incorporating the highest frequencies. In the transaxial direction, the highest frequencies are not yet fully converged, even at high iteration numbers. Snyder et al [140] argue that the Gibbs artifact is due to the ill-posedness of the reconstruction problem (high spatial frequencies are lost during detection) and they show that post-smoothing reduces the artifact. Without smoothing, the Gibbs artifact also appears in ILIN180 reconstructions, but it is suppressed by the 2D Gaussian post-filtering. In the axial direction, the high

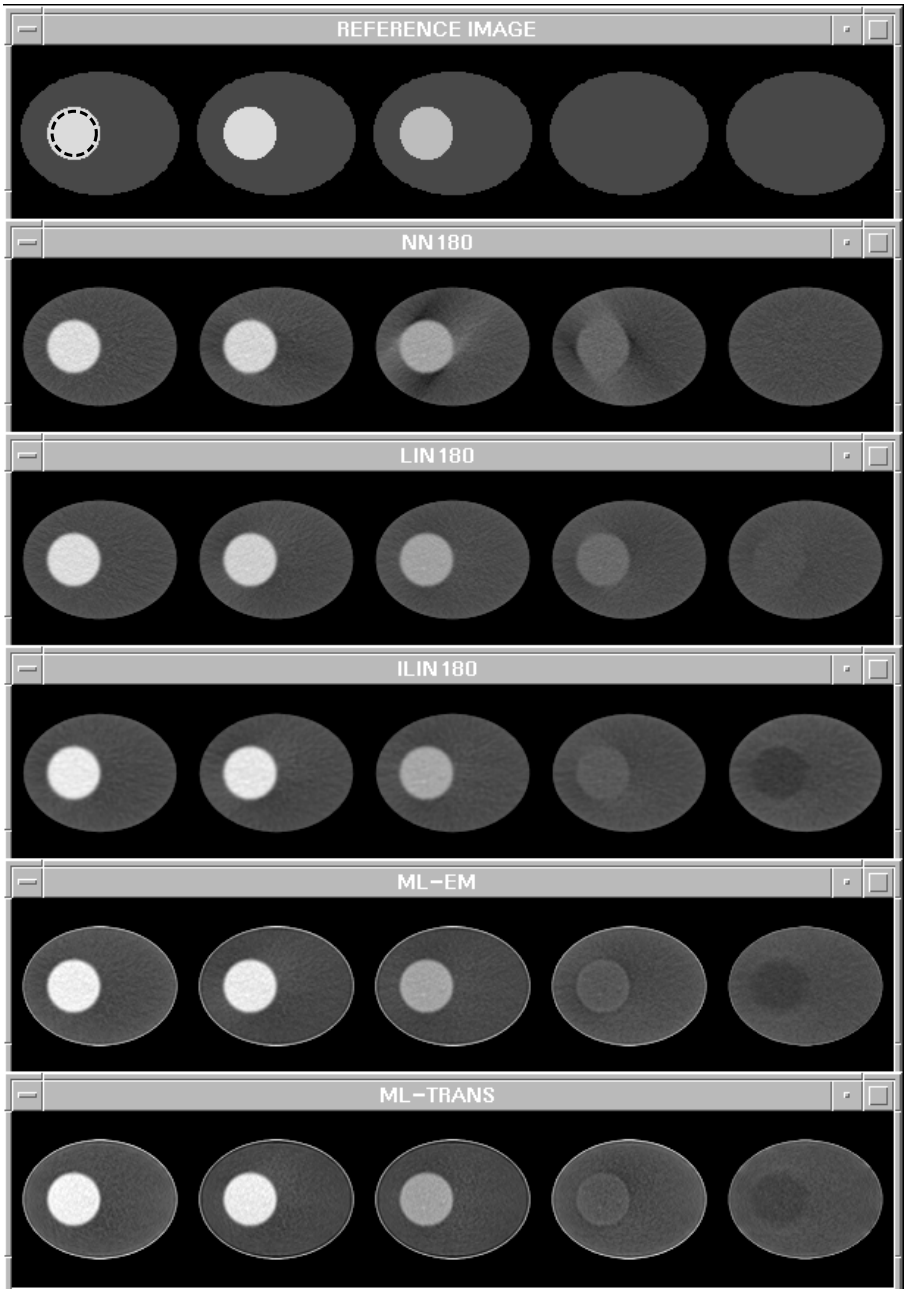

Figure 4.6: *Phantom 4: five reconstructed transaxial slices, from top to bottom: reference image, NN180, LIN180, ILIN180, ML-EM, ML-TR. For ML-EM and ML-TR, images at highest iteration number are shown, for ILIN180, it is the image at 20 iterations, smoothed with* $\sigma = 1$.

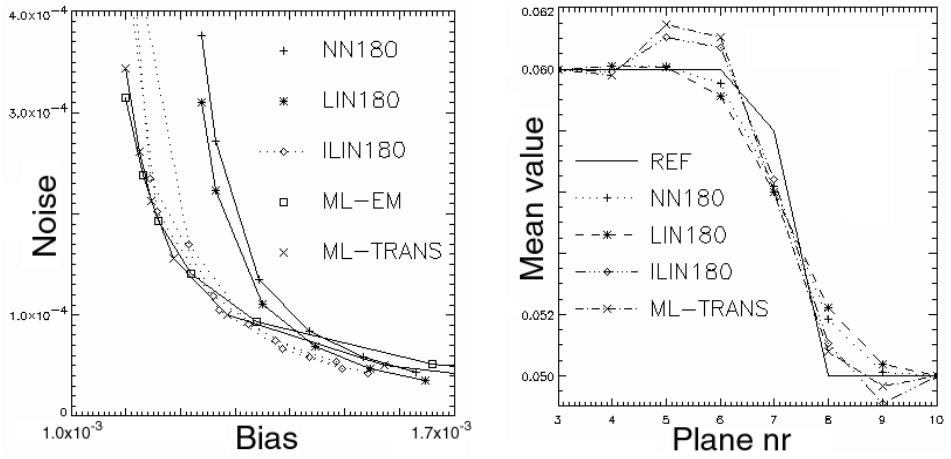

(a) (b)

Figure 4.7: *Phantom 4: (a) bias-noise curves for a region around the central cylinder. Gaussian smoothing with sigma = 0 up to 2.5 pixels was applied. For iterative FBP, iterations 5, 10 and 20 are shown, as independent lines. For ML, iterations 5, 10, 15, 30, 50, 75, 100, 150 are shown. (b) Mean value of the circular region as a function of axial position for the reference image, NN180, LIN180, ILIN180 and ML-TR.*

frequencies are suppressed by the sieve. Omitting the sieve, however, results in still stronger artifacts (data not shown), because only few projection angles are actually acquired for every reconstructed slice. In the gradient region, the bias noise curves of the iterative methods are superior to those of the non-iterative methods, which is attributed to the artifact reduction and recovery of axial resolution. All three iterative methods perform equivalently near the gradient. When the entire region is considered, we found that the ML-methods produce better bias-noise curves. Visual inspection reveals that in homogeneous regions, ILIN180 tends to produce higher noise than the ML-methods.

Figure 4.8 shows five transaxial slices for phantom 5, and figure 4.9 shows a profile intersecting two ellipsoids (position shown on top left slice of figure 4.8). For this simulation, the bias-noise curves of ILIN180 overlapped those of NN180 and LIN180, while those of the two ML-methods had about 20% lower bias for the same noise level (not shown). Figures 4.8 and 4.9 confirm that the iterative algorithm yields better axial resolution than LIN180, resulting in a better contrast. The axial Gibbs effect produces shadows of opposite contrast in slices adjacent to objects with strong axial gradients.

Figure 4.10 shows the results for phantom 6. FBP (a) and IFBP (b) result in severe streak artifacts. Both ML-EM and ML-TR yield strong reduction of the streak artifacts. These results are confirmed by the corresponding bias-noise curves (not shown). The robustness of the maximum-likelihood algorithms clearly plays an

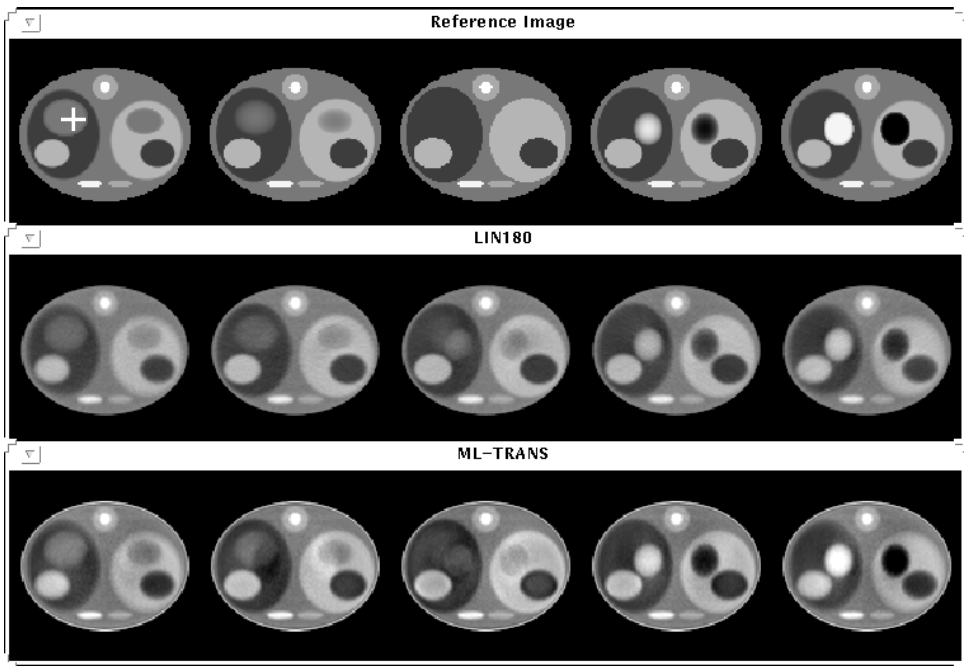

Figure 4.8: *Phantom 5: five reconstructed transaxial slices, from top to bottom: reference image, LIN180 and ML-TR.*

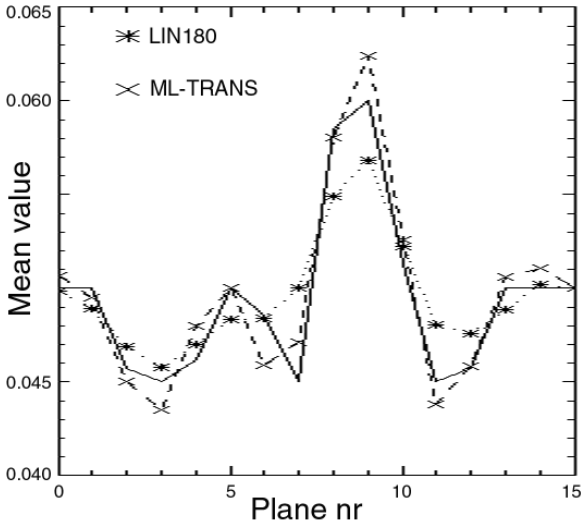

Figure 4.9: *Phantom 5: an axial profile (position shown on top left slice) for the reference image (solid line), LIN180, and ML-TR.*

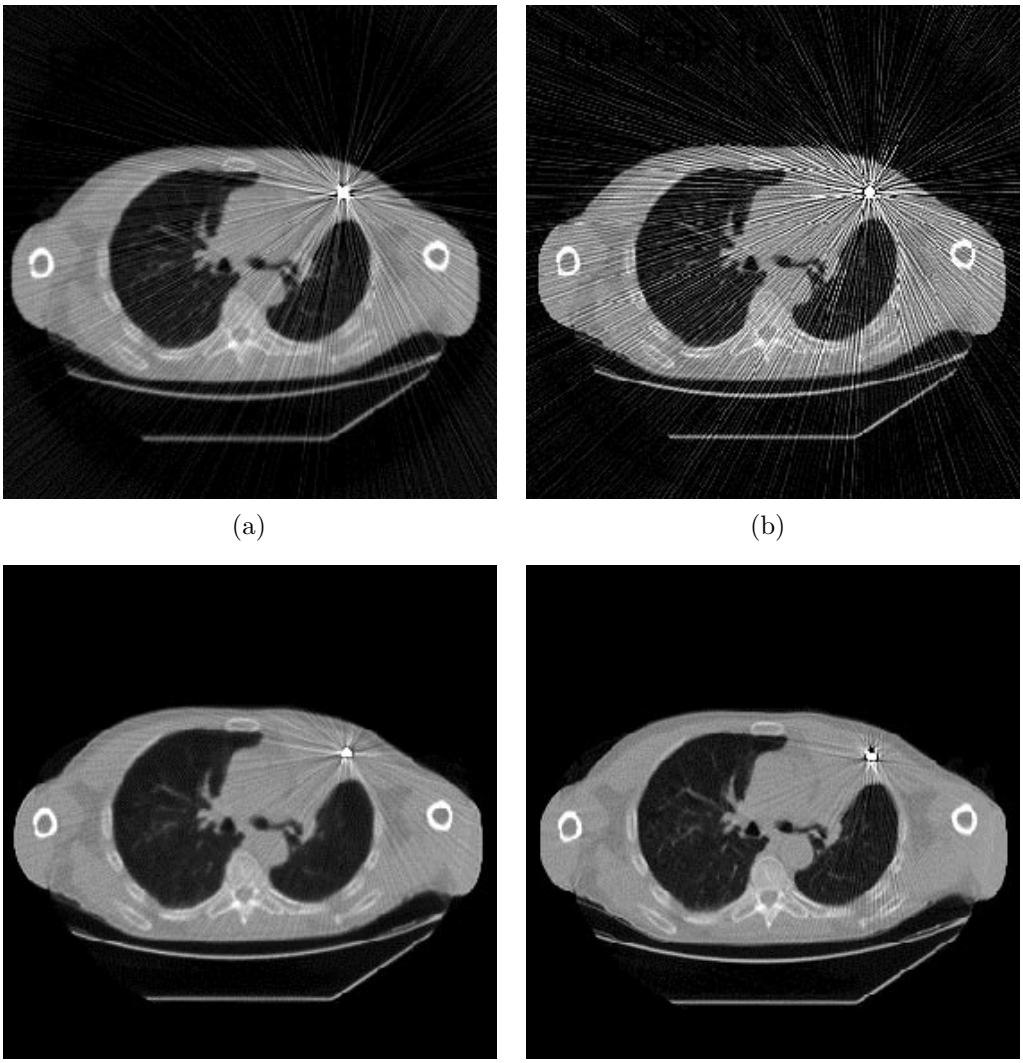

(a) (b)

(c) (d)

Figure 4.10: *Phantom 6: (a) FBP, (b) IFBP, (c) ML-EM, (d) ML-TR.*

important role. On the other hand, comparing ML-TR with ML-EM also indicates that the correct noise model results in a further reduction of the streak artifacts.

4.9.5 Conclusion for the simulation study

In this exploratory study, we hoped to find evidence that iterative reconstruction based on a superior mathematical model of the acquisition, would produce a clear improvement in image quality, as compared to the classical approach.

We conclude that iterative ML reconstruction allows improvement of the axial resolution beyond that of nearest neighbor interpolation (NN180) without introducing the in-plane distortions seen in NN180 and without excessive noise amplification. Iterative FBP (ILIN180) can produce lower bias than LIN180 or NN180, but for the same bias, noise was equivalent or higher than for the ML-methods, depending on the region studied. Performance of ML-EM and ML-TR was rather similar in this study. This suggests that, at least in these simulations, the exactness of the noise model was less important than the robustness of the numerical procedures and the more accurate geometrical modeling. Constraining axial resolution is necessary, and the current sieve-based constraint introduces unacceptable axial Gibbs artifacts, which completely offset the advantage of improved axial resolution, in-plane artifact reduction and noise suppression. A potential solution is the use of a non-linear axial constraint, such as a Gibbs prior [42]. Preliminary results indicate that, when small objects with very high attenuation are present, performance of ML-EM, and ML-TR in particular, is significantly better.

4.10 Conclusion

In this chapter, we have given an overview of iterative reconstruction and of the maximum-likelihood method ML-TR in particular. ML-TR forms the basis of this thesis. All algorithms described in the next chapter are extensions of ML-TR. The practical implementation of the projector and backprojector has been discussed. Finally, we have presented our initial experience with iterative reconstruction applied to spiral CT. The most promising application appears to be the reduction of metal artifacts. This brings us to chapter 5: applying iterative reconstruction for reduction of metal artifacts.

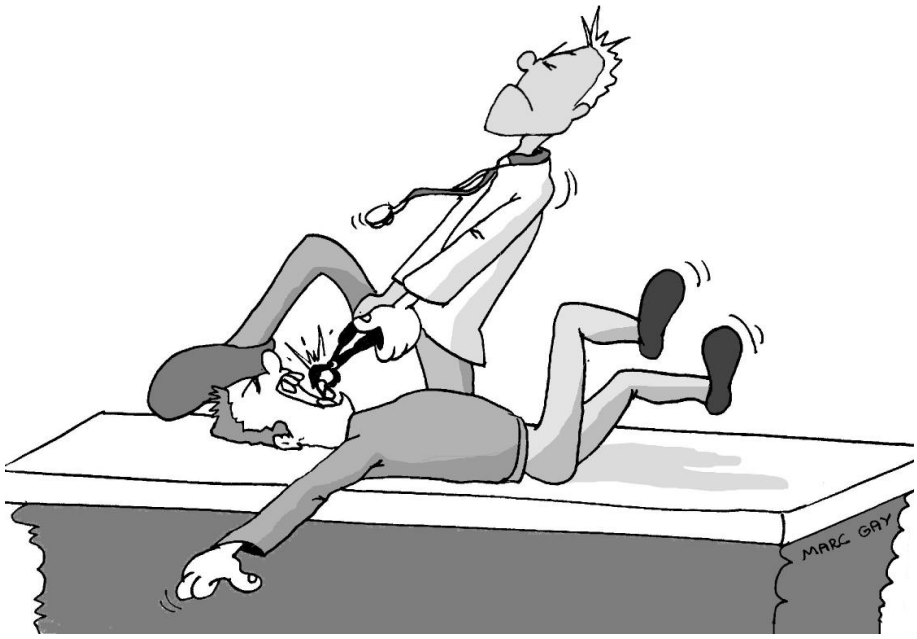

. . . reduction of metal artifacts . . .

Chapter 5

Reduction of metal artifacts

5.1 Introduction

In chapter 3, we have determined the most important causes of metal artifacts: noise, beam hardening, the non-linear partial volume (NLPV) effect, and scatter. In chapter 4, we have described the aspects of iterative reconstruction that are most relevant for this thesis. In this chapter, iterative reconstruction is applied to reduce metal artifacts, taking into account the causes determined in chapter 3.

Many different approaches for metal artifact reduction (MAR) are found in literature. The most obvious solution is to prevent metal artifacts by using less-attenuating materials (e.g. titanium) or devices with smaller cross-section [50, 126, 147]. A second possible approach is to reduce metal artifacts by adapting the acquisition. Noise is reduced by using a higher tube current. Beam hardening is minimized by using pre-filtering to obtain a narrower spectrum. Haramati [50] showed that using a higher tube voltage gives no substantial artifact reduction. The NLPV effect is reduced by using thinner X-ray beams. Aliasing is reduced by using a higher number of detector elements and views. Unfortunately, all these measures are in direct conflict with other concerns such as low patient dose, tube life, low cost, etc .... Robertson [125, 126] showed that multi-planar reformation[1] allows a better visualization of bone in the presence of metallic orthopedic implants. Henrich [53] applied a post-reconstruction image processing algorithm for removing metal artifacts. The majority of MAR-methods consist of a modified reconstruction algorithm, in which metal objects are usually considered opaque and data corresponding to projection lines through metal objects are defined as *missing data*. These methods can be divided into two groups:

- Projection completion methods: missing data are replaced by synthetic data, obtained by polynomial or linear interpolation [46, 61, 82, 91, 96, 101, 134,

[1] Multi-planar reformation is the calculation of images in planes perpendicular or oblique to the scan planes

135, 146], pattern recognition [102], or linear prediction methods [121]. Many of these methods apply beam hardening correction as a pre-processing step.

- Iterative methods: existing iterative methods, such as the maximum likelihood expectation maximization (ML-EM) algorithm and the algebraic reconstruction technique (ART), are modified in order to ignore missing data [117, 127, 148].

We hypothesize that artifacts are caused by deviations of the mathematical model assumed by the reconstruction algorithm, from the true acquisition process. Hence, improving the accuracy of the model should reduce or eliminate the artifacts. From the previous chapter, we know that ML-TR uses a Poisson noise model. Section 5.2 investigates the usefulness of this noise model with respect to metal artifacts. In addition, the usefulness of including prior knowledge is investigated. Beam hardening is addressed in section 5.3, by introducing a polychromatic acquisition model. Section 5.4 addresses the NLPV effect, by introducing models for the finite beamwidth and the continuous scanner rotation.

5.2 A maximum a posteriori algorithm

This section is based on [25] and presents a maximum a posteriori (MAP) algorithm for reduction of metal artifacts. If along some projection lines all (or nearly all) photons are attenuated, the projections are incomplete. We hypothesize that the inclusion of some prior knowledge may compensate for this missing information. The algorithm uses a Markov random field smoothness prior and applies increased sampling in the reconstructed image. Good results are obtained for simulations and phantom measurements. Streak artifacts are reduced while small line-shaped details are preserved. Comparisons are included with the projection completion method, and with iterative reconstruction ignoring the projections through metal objects.

5.2.1 Algorithm

The algorithm is based on ML-TR, described in chapter 4. ML-TR assumes that the measured detector read-outs have a Poisson distribution. Therefore, projections with high attenuation, which result in low detected intensities, are considered less reliable, while projections with low attenuation, which result in high detected intensities, are considered more reliable. We use this noise model because we want to minimize noise artifacts. Additionally, the properties of this noise model also make the algorithm inherently robust against other sources of artifacts that are most prominent in directions of high attenuation, such as beam hardening, the NLPV effect, and scatter.

Two extensions are introduced:

1. A Markov random field smoothness prior is used with a Huber potential function [106, 112], given by eq.(4.29). The Huber function has the advantage of

being convex and more or less edge-preserving. The reconstruction in parts of the image for which many high-count measurements are available, is mainly steered by the measured data, while the prior dominates in under-determined parts of the image.

2. Iterations are performed using a reconstruction image at double resolution. After the last iteration, the image is re-sampled to normal resolution. This higher resolution provides a better model for sharp transitions in the image. The increased number of degrees of freedom allows a better handling of other sources of artifacts, such as the NLPV effect and beam hardening, and it makes the algorithm more robust.

As described in section 4.6, the logarithm of the posterior probability is given by

$$L = \sum_{i=1}^{I} \left(y_i \cdot \ln \hat{y}_i - \hat{y}_i \right) - \beta \sum_{j=1}^{J} \sum_{h=1}^{J} w_{jh} V(\mu_h - \mu_j), \tag{5.1}$$

where y_i and $\hat{y}_i$ represent the measured and calculated counts in detector read-out i, μ_j is the linear attenuation coefficient in pixel j, $w_{jk} = 1$ for adjacent pixels j and k, $w_{jk} = 0$ elsewhere and $V(\mu)$ is the potential function. The actual update step is given by

$$\mu_j^{n+1} = \mu_j^n + \frac{\sum_{i=1}^{I} l_{ij} \cdot (\hat{y}_i - y_i) + \beta \sum_{h=1}^{J} \frac{\partial V}{\partial \mu}(\mu_h - \mu_j)}{\sum_{i=1}^{I} l_{ij} \cdot \left[\sum_{h=1}^{J} l_{ih} \right] \cdot \hat{y}_i}. \tag{5.2}$$

where n is the iteration number and l_{ij} is the effective intersection length of projection line i with pixel j. The ray-driven projector and backprojector described in section 3.2 and section 4.8 respectively are used.

5.2.2 Simulations

Our CT-simulator is described and validated in chapter 3. Parameters were adjusted to the Siemens Somatom Plus 4 scanner as truthfully as possible. The simulations include beam hardening (summing 5 discrete energy levels), noise (using Poisson noise and a blank scan of 10^5 photons), scatter (using a constant scatter level and a scatter fraction of 0.0001), and the trans-axial NLPV effect.

Phantom 7 is a circular plexiglas phantom (figure 5.1 (a) with a diameter of 9.5 cm and containing 3 amalgam inserts ($\varnothing$ = 1 mm, 2 mm and 3 mm) and 12 line-shaped objects (length = 8 mm, width = 1 or 2 mm, μ=$\pm$40%, $\pm$20%, $\pm$10% or $\pm$5% compared to the attenuation of plexiglas ; the effective linear attenuation coefficient of plexiglas is about 0.2 cm^{-1}). We chose a circular phantom in order to exclude most non-metal-artifacts and to concentrate on pure metal-artifacts. Figure 5.1 (b) shows an uncorrected FBP reconstruction of the simulation. All simulation results are shown using a windowing interval $\mu = [0.0\,;\,0.4]\,\text{cm}^{-1}$ (centered at $\mu_{\text{plexiglas}}$),

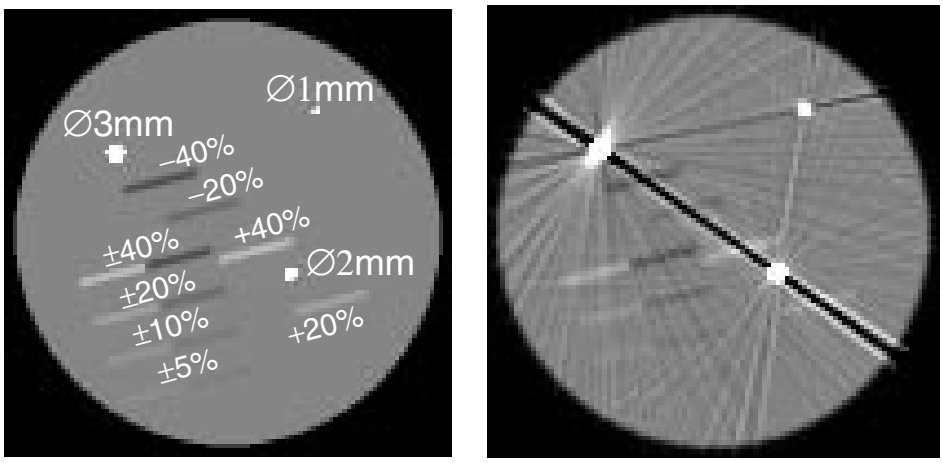

(a) (b)

Figure 5.1: *Phantom 7: (a) reference image and (b) FBP reconstruction.*

which corresponds to a window of 2000 HU and a level of 0 HU. The images are $10\,\text{cm} \times 10\,\text{cm}$ and 102×102 pixels.

Figure 5.2 shows ML-TR reconstructions of the simulation, computed at normal resolution (top) and at double resolution followed by re-sampling (bottom), without prior (left) and with a Huber prior (right).

All ML-TR reconstructions in figure 5.2 exhibit fewer streaks than the FBP reconstruction in figure 5.1 (b). This illustrates the robustness of the ML-TR algorithm and the importance of the correct acquisition model. Comparison of the images at the left to those at the right shows the importance of the prior for a good convergence. Comparison of top and bottom images shows the importance of the double resolution reconstruction. ML-TR *with* prior at *double* resolution (figure 5.2 (d) gives the best result: the streaks are removed and the line-shaped objects are conserved. However, the use of the prior introduces a certain amount of smoothing.

5.2.3 Measurements

Phantom 8 is a circular plexiglas phantom (figure 5.3 (a)) with thickness 1 cm and a diameter of 9.5 cm, similar to phantom 7 (software phantom) from the previous section. A number of small plexiglas cylinders, some of which contain amalgam fillings or line-shaped objects (candle-grease, air, super glue and wall-filler), are inserted in holes in the phantom. Figure 5.3 (b) shows the setup *with* amalgam fillings. Alternatively, the cylinders with amalgam fillings were replaced by plain plexiglas cylinders, yielding a setup without metal objects (not shown). Both setups were scanned with a Siemens Somatom Plus 4 CT-scanner, using sequential scan mode with fixed focal spot, a nominal tube voltage of 120 kV, a tube current of

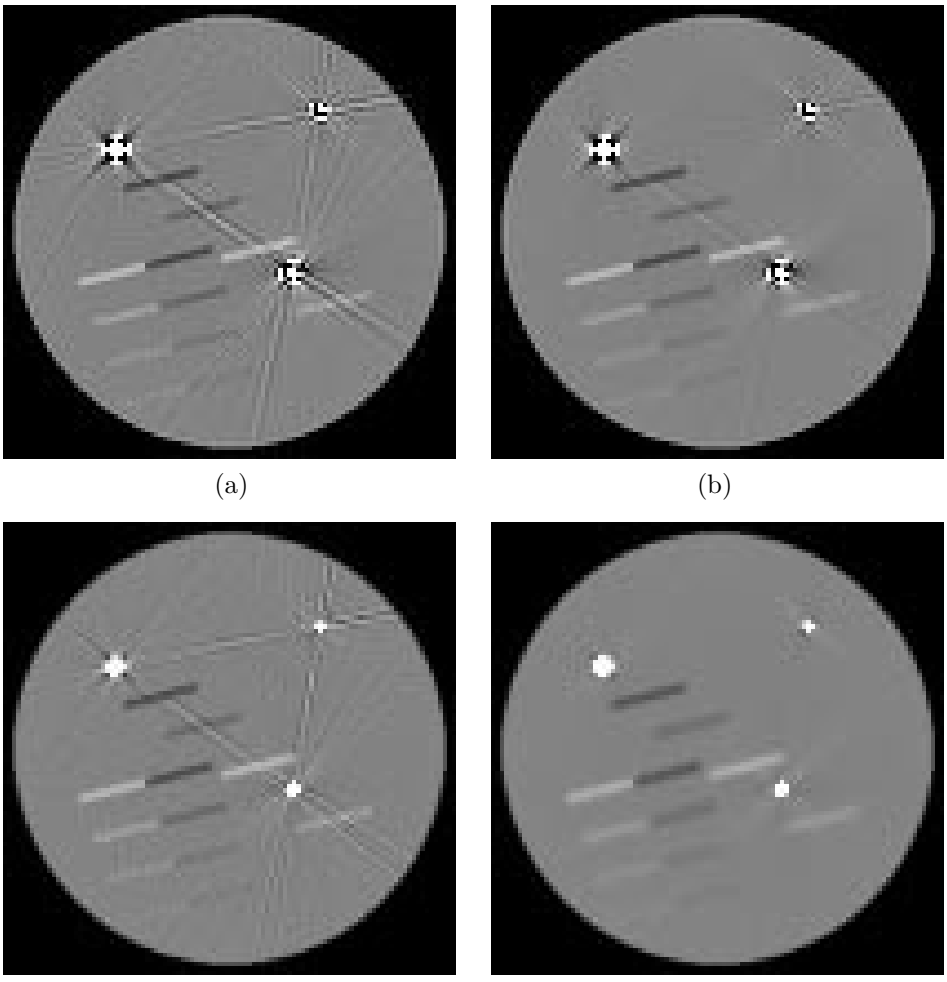

(a) (b)

(c) (d)

Figure 5.2: *Simulation of phantom 7 reconstructed with ML-TR: at single (a, b) and at double (c, d) resolution, without (a, c) and with (b, d) Huber prior.*

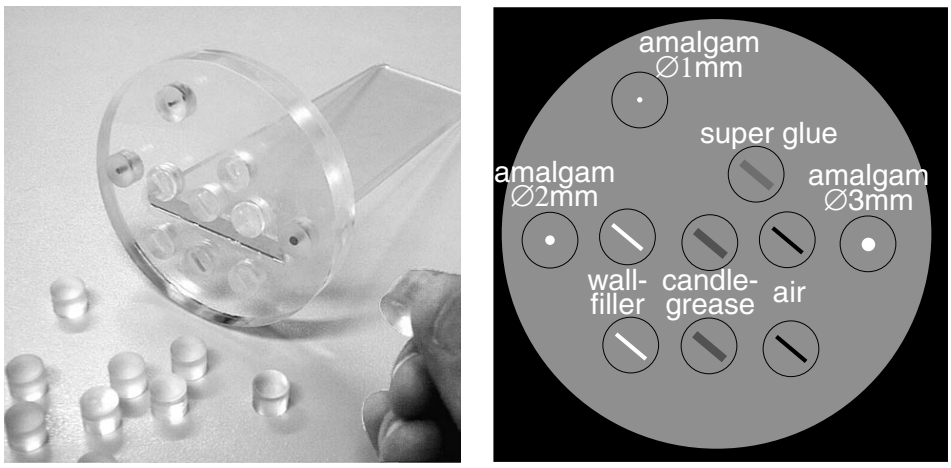

(a) (b)

Figure 5.3: *Phantom 8: (a) picture and (b) schematic representation.*

130 mA, a slice thickness of 1.0 mm, and a 0.75 s rotation. All measurements include standard first order beam hardening correction by the scanner. The raw data were transfered to a PC for further processing using our own reconstruction software. All measurement results are shown using a windowing interval $\mu = [0.0\,;\,0.4]\,\mathrm{cm}^{-1}$ (centered at $\mu_{\mathrm{plexiglas}}$), which corresponds to a window of 2000 HU and a level of 0 HU. The images are $10\,\mathrm{cm} \times 10\,\mathrm{cm}$ and 102×102 pixels.

Figure 5.4 shows the uncorrected FBP reconstructions of the measurements of phantom 8 without (a) and with (b) amalgam fillings. Figure 5.5 and figure 5.6 show ML-TR reconstructions of the measurements of phantom 8 with and without amalgam fillings, computed at normal resolution (top) and at double resolution followed by re-sampling (bottom), without prior (left) and with a Huber prior (right).

The results in figure 5.5 are similar to the simulations. All ML-TR reconstructions exhibit less streaks than the FBP reconstruction in figure 5.4 (b). Comparison of the images at the left to those at the right shows the importance of the prior for a good convergence. Comparison of top and bottom images shows the importance of the double resolution reconstruction. ML-TR *with* prior at *double* resolution (figure 5.5 (d)) gives the best result: streaks are reduced and the line-shaped objects are conserved. Again, some smoothing is introduced by using the prior. Also, there are some remaining streaks in the vicinity of the amalgam fillings. Close investigation has shown that these remaining streaks are due to a slight misalignment of the detector elements. This explains why these streaks are not present in the simulations. We found out later that the scanner itself allows to correct for this effect, but that this correction was probably switched off during the measurement of phantom 8. In all subsequent measurements we made sure that this correction was switched on. For the measurements without amalgam fillings (figure 5.6), the double resolution has little effect, and the prior only introduces some smoothing.

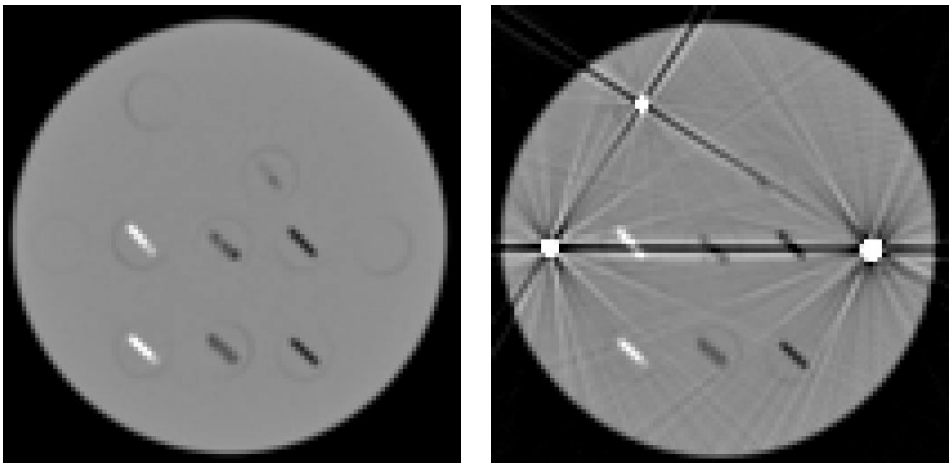

(a) (b)

Figure 5.4: *Phantom 8: (a) FBP without amalgam fillings, (b) FBP with amalgam fillings.*

5.2.4 Other algorithms

For comparison, the measurements were also reconstructed using the projection completion method [82, 91] and using maxium-likelihood methods (ML-EM and ML-TR) ignoring the missing data [148].

In our implementation of the projection completion method, the metal objects are segmented from an FBP reconstruction using a threshold of $\mu = 2$ cm^{-1}. The metal-only image is projected, resulting in a metal-only sinogram. Parts of the original sinogram corresponding to non-zero values in the metal-only sinogram are defined as missing data. These missing values are replaced by linear interpolation on a view-by-view basis. The resulting synthetic sinogram is reconstructed using FBP. Finally, the previously segmented metal image is added to the reconstruction.

For the maximum-likelihood methods ignoring the missing data, missing data are defined in the same way as in the projection-completion method. In each iteration, the error sinogram is made zero at the positions of missing data. At the end of the iterations, the previously segmented metal image is added to the reconstruction.

Figure 5.7 (a) shows the FBP reconstruction after projection completion using linear interpolation [82, 91]. Figure 5.7 (b) shows the ML-EM reconstruction ignoring missing data [148]. Figure 5.7 (c) shows the ML-TR reconstruction ignoring missing data. Figure 5.7 (d) repeats the reconstruction obtained with ML-TR at double resolution with Huber prior (figure 5.5 (d)).

For the three compared methods (a–c), the quality of the reconstruction in the vicinity of the metals compares favorably with ML-TR at double resolution with Huber prior. On the other hand new streaks are created at other locations in the image. We cannot conclude that our method gives better results than the

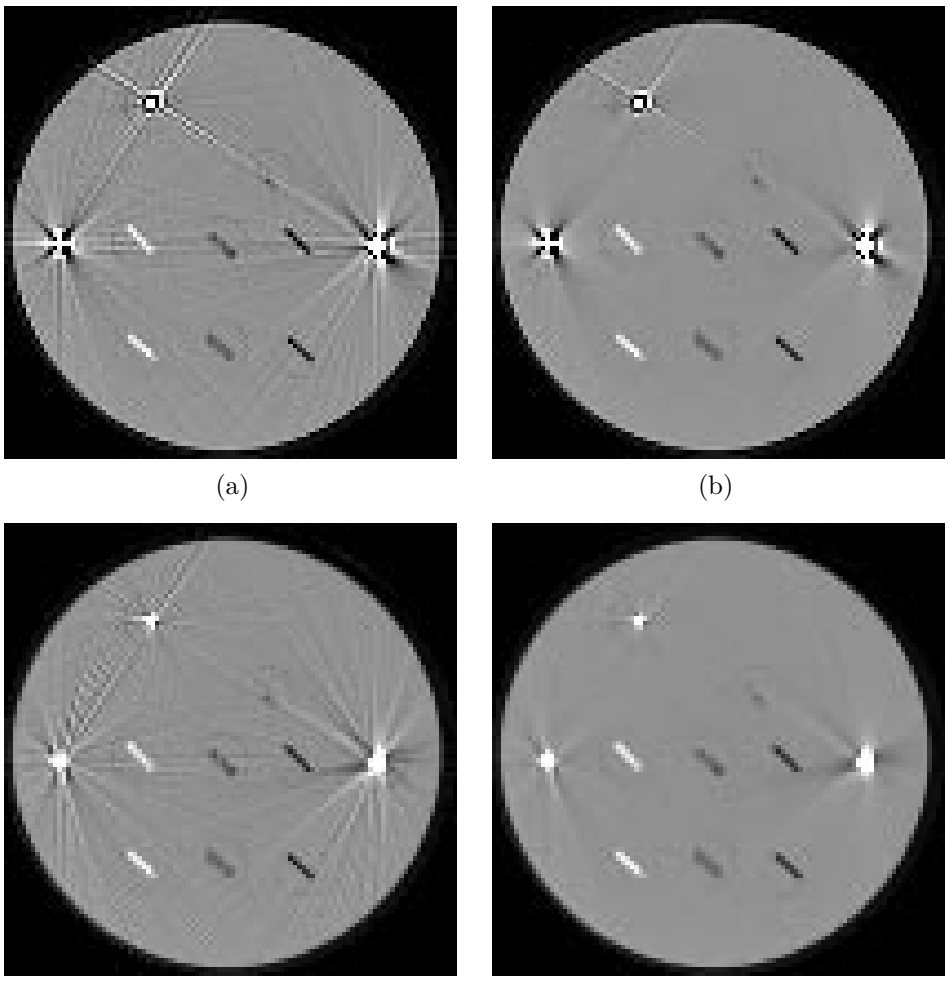

(a) (b)

(c) (d)

Figure 5.5: *Measurement of phantom 8 with amalgam fillings reconstructed with ML-TR : at single (a, b) and at double (c, d) resolution, without (a, c) and with (b, d) Huber prior.*

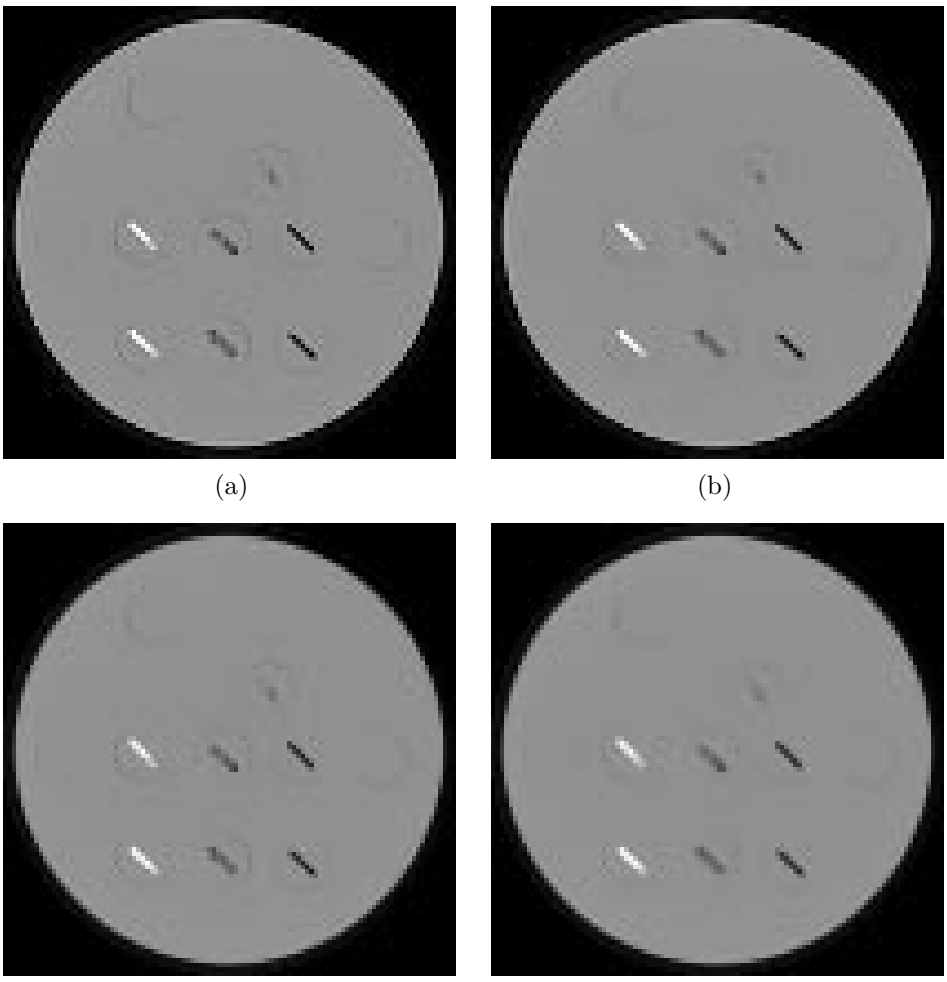

(a) (b)

(c) (d)

Figure 5.6: *Measurement of phantom 8 without amalgam fillings reconstructed with ML-TR: at single (a, b) and at double (c, d) resolution, without (a, c) and with (b, d) Huber prior.*

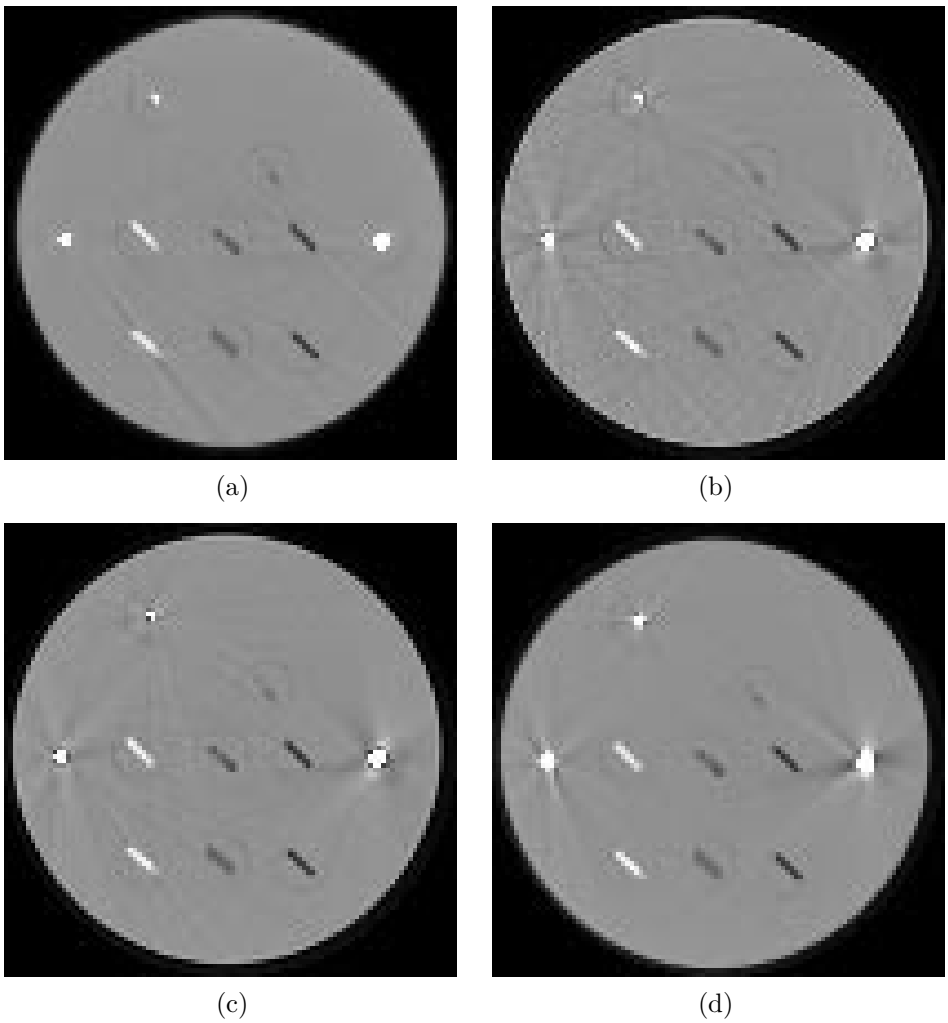

(a) (b)

(c) (d)

Figure 5.7: *Measurement of phantom 8 with amalgam fillings reconstructed with (a) FBP after projection completion, (b) ML-EM ignoring missing data, (c) ML-TR ignoring missing data, and (d) ML-TR at double resolution with Huber prior.*

other methods. Nevertheless, the results confirm our hypothesis that improving the accuracy of the acquisition model reduces metal artifacts. More investigation is required to further improve the model of the scanner geometry and to include explicit models for beam hardening, the NLPV effect, and scatter.

5.2.5 Conclusion for the MAP algorithm

Our simulations indicate that ML-TR reconstruction using a-priori knowledge and using an increased number of degrees of freedom results in effective artifact reduction. The model of the scanner geometry must be improved in order to reduce the remaining streaks. Including models for beam hardening, the NLPV effect, and scatter may allow to reduce the weight of the prior, offering better artifact reduction with less smoothing. For application in clinical routine, a strong reduction of the computational cost of the algorithm is required.

5.3 A polychromatic algorithm

This section is based on [26] and presents a new iterative maximum likelihood reconstruction algorithm for X-ray computed tomography. The algorithm prevents beam hardening artifacts by incorporating a polychromatic acquisition model. The continuous spectrum of the X-ray tube is modeled as a number of discrete energies. The energy dependence of the attenuation is taken into account by decomposing the linear attenuation coefficient into a photo-electric component and a Compton scatter component. The relative weight of these components is constrained based on prior material assumptions. Excellent results are obtained for simulations and for phantom measurements. Beam hardening artifacts are effectively eliminated. The relation with existing algorithms is discussed.

5.3.1 Existing beam hardening correction approaches

FBP is based on the assumption that every pixel can be characterized by a single parameter μ, the linear attenuation coefficient, and that the logarithm of the measurement is the line integral of μ. In reality, an X-ray tube emits a continuous spectrum, and the attenuation in every pixel is energy-dependent. This results in beam hardening, a phenomenon described in detail in section 3.4.2.

Many different solutions for beam hardening are found in the literature:

A first approach is to limit the amount of beam hardening by physically prefiltering the X-ray beams [7, 99] A second approach is to correct the measurements based on certain material assumptions. The method of *water correction* or *linearization correction* assumes that all substances in the scanning plane have the same energy dependence and corrects the measurements prior to reconstruction [7, 54, 99, 118]. The so-called *post-reconstruction* methods [39, 55, 59, 72, 74, 89, 100, 107, 124, 130] make a first reconstruction, from which a rough material

distribution is estimated. This material distribution allows to estimate the measurement error, based on either simulations or calibration measurements. A new reconstruction is then calculated from the corrected measurements. This process can be repeated several times. We implemented this approach for comparison with our approach (see section 5.3.3). A third approach is the dual energy approach [1, 2, 19, 33, 52, 118, 151]. Here, the linear attenuation coefficient is decomposed into a photo-electric and a Compton scatter component. A drawback of this approach is that it requires either two scans at different tube voltages or special detectors with two different energy windows.

Other approaches use image processing to remove beam hardening streaks from the reconstructed images [104, 141]. A conceptual overview of beam hardening correction approaches is given in [143].

5.3.2 Algorithm

We now introduce a polychromatic acquisition model, and we present a new algorithm IMPACT (Iterative Maximum-likelihood Polychromatic Algorithm for CT). IMPACT is an extension of ML-TR, described in chapter 4.

ML-TR uses the following acquisition model:

$$\hat{y}_i = b_i \cdot \exp(-\sum_{j=1}^{J} l_{ij}\mu_j), \tag{5.3}$$

where b_i is the number of photons that would be detected in the absence of absorber (blank scan), and l_{ij} is the effective intersection length of projection line i with pixel j. b_i is measured by a calibration scan.

A more accurate acquisition model is given by:

$$\hat{y}_i = \sum_{k=1}^{K} b_{ik} \cdot \exp(-\sum_{j=1}^{J} l_{ij}\mu_{jk}), \tag{5.4}$$

where k is an energy index and K is the total number of energies. μ_{jk} is the linear attenuation coefficient in pixel j at energy k and b_{ik} is the total energy that would be detected by detector i in the absence of absorber for incident photons of energy E_k. b_{ik} is given by

$$b_{ik} = I_{ik} \cdot S_k \cdot E_k, \tag{5.5}$$

where I_{ik} is the emitted source spectrum (number of photons), S_k is the detector sensitivity (dimensionless), and E_k is the photon energy (keV). The third factor is introduced because CT uses energy-counting detectors, compared to photon-counting detectors in nuclear medicine. Consequently, the measured quantity is not a number of photons but an energy, and it will not strictly follow a Poisson distribution. This fact is usually ignored, because the Poisson model is still a good approximation [48, 63]. Although in this work b_{ik} is independent of i, the index i

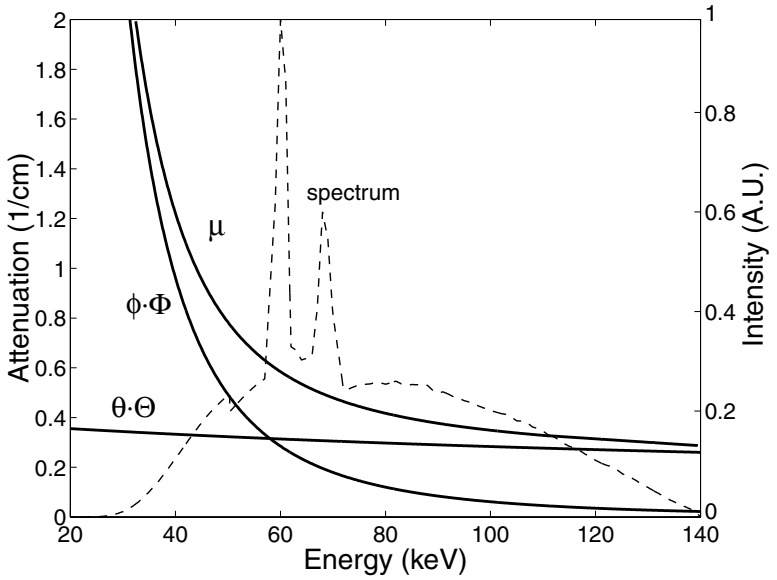

Figure 5.8: *Decomposition of the linear attenuation coefficient μ of bone into a photo-electric component and a Compton scatter component. The dashed line represents a simulated spectrum b_{ik} (normalized) provided by Siemens.*

could be exploited to incorporate source fluctuations and the effect of a bow-tie filter. The number of unknowns μ_{jk} in eq.(5.4) is $K \times J$, compared to J in eq.(5.3). This higher number of degrees of freedom leads to poor convergence. Hence, constraints must be introduced.

For any particular substance, the energy-dependent linear attenuation coefficient $\mu(E)$ can be approximated by a linear combination of a number of basic functions:

$$\mu(E) = a_1 f_1(E) + a_2 f_2(E) + \ldots + a_n f_n(E). \tag{5.6}$$

A good set of basic functions are the energy dependence $\Phi(E)$ of the photo-electric effect and the energy dependence $\Theta(E)$ of Compton scatter [1, 118]. This results in a decomposition of $\mu(E)$ into a photo-electric component and a Compton scatter component:

$$\mu(E) = \phi \cdot \Phi(E) + \theta \cdot \Theta(E). \tag{5.7}$$

Figure 5.8 illustrates this for the case of bone. We call ϕ the *photo-electric coefficient* and θ the *Compton coefficient*. The energy dependence of the photo-electric effect is approximated by

$$\Phi(E) = \frac{1/E^3}{1/E_0^3}, \tag{5.8}$$

where E_0 is a reference energy (e.g. $E_0 = 70$ keV). This is a good approximation except for substances that have a *K-edge* in the used spectral range, such as lead or glass ([87] p.77).

The energy dependence of Compton scatter is approximated by

$$\Theta(E) = \frac{f_{\mathrm{KN}}(E)}{f_{\mathrm{KN}}(E_0)}, \tag{5.9}$$

where f_{KN} is the Klein-Nishina function, given by:

$$\begin{aligned} f_{\mathrm{KN}}(E) =& \frac{1+\alpha}{\alpha^2} \cdot \left(\frac{2 \cdot (1+\alpha)}{1+2\alpha} - \frac{\ln(1+2\alpha)}{\alpha} \right) \\ &+ \frac{\ln(1+2\alpha)}{2\alpha} - \frac{1+3\alpha}{(1+2\alpha)^2}, \end{aligned} \tag{5.10}$$

with α = E / 511 keV.

For any substance with known $\mu(E)$ (data from the National Institute of Standards and Technology[2] based on [68] were used), ϕ and θ are calculated by applying a least squares fit to eq.(5.7) and using the analytic formulations of $\Phi(E)$ and $\Theta(E)$ (eq.(5.8), (5.9), and (5.10)). In practice, this fit is performed after discretization into K energy levels. From eq. (5.7), (5.8), and (5.9), it can be seen that ϕ and θ actually represent the photo-electric part and the Compton scatter part of the attenuation at $E_0 = 70$ keV. The calculated values of ϕ and θ and the values of $\mu_{70\mathrm{keV}}$ are shown in table 5.1 for some common substances.

Discretization of eq.(5.7) gives:

$$\mu_{jk} = \phi_j \cdot \Phi_k + \theta_j \cdot \Theta_k. \tag{5.11}$$

Φ_k and Θ_k represent the energy dependence of μ_{jk} and are *known*, dimensionless functions. ϕ_j and θ_j represent the material dependence and have dimension cm^{-1}. The acquisition model of eq.(5.4) becomes

$$\hat{y}_i = \sum_{k=1}^{K} b_{ik} \cdot \exp\Big(- \sum_{j=1}^{J} l_{ij} \cdot \big[\phi_j \cdot \Phi_k + \theta_j \cdot \Theta_k \big] \Big). \tag{5.12}$$

The number of unknowns (ϕ_j and θ_j) is now $2J$.

Figure 5.9 (a) shows a plot of ϕ versus θ, and figure 5.9 (b) is a zoomed plot for the dashed region. Most substances lie in the neighborhood of the piecewise-linear ϕ-θ-curve defined by the set of base substances [air, water, bone, iron] (solid line). We now assume that all substances lie *on* this ϕ-θ-curve. This assumption implies that the energy dependence of the attenuation is required to be a linear combination of the energy dependences of two adjacent base substances.

Figure 5.9 (c) shows a plot of the monochromatic attenuation $\mu_{70\ \mathrm{keV}}$ versus ϕ and θ, and figure 5.9 (d) is a zoomed plot for the dashed region. Again, the set of

[2] http://physics.nist.gov/PhysRefData/

Table 5.1: *Photo-electric coefficient ϕ, Compton coefficient θ and monochromatic linear attenuation coefficient μ_{70keV} for a number of common substances.*

	θ (1/cm)	ϕ (1/cm)	$\mu_{70\text{keV}}$ (1/cm)
air	0.0002	1.7e-05	0.0002
fat	0.1631	0.0080	0.1717
soft tissue	0.1777	0.0148	0.1935
blood	0.1778	0.0154	0.1942
breast	0.1818	0.0118	0.1945
water	0.1793	0.0144	0.1946
brain	0.1818	0.0155	0.2022
muscle	0.1793	0.0155	0.2032
lung	0.1857	0.0158	0.2036
ovary	0.1867	0.0156	0.2038
plexiglas	0.2072	0.0107	0.2187
bone	0.3109	0.1757	0.4974
Al	0.4274	0.2125	0.6523
Ti	0.7189	1.8201	2.6530
Fe	1.3904	5.32734	7.0748

base substances define a μ-ϕ-curve and a μ-θ-curve and all substances are assumed to lie on them. For a given $\mu_{70\text{ keV}}$, these functions unambiguously determine the values of ϕ and θ. This means that ϕ_j and θ_j in eq.(5.12) can be substituted by the functions $\phi(\mu_j)$ and $\theta(\mu_j)$, resulting in the following acquisition model:

$$\hat{y}_i = \sum_{k=1}^{K} b_{ik} \cdot \exp\Big(- \sum_{j=1}^{J} l_{ij} \big[\phi(\mu_j) \cdot \Phi_k + \theta(\mu_j) \cdot \Theta_k\big]\Big), \tag{5.13}$$

where $\phi(\mu_j)$ and $\theta(\mu_j)$ are known functions of μ_j, and μ_j now represents the monochromatic linear attenuation coefficient at 70 keV in pixel j. The number of unknowns μ_j in eq.(5.13) is now J. This equation is implemented more efficiently by bringing Φ_k and Θ_k outside the summation over j (projection):

$$\hat{y}_i = \sum_{k=1}^{K} b_{ik} \cdot \exp\Big(- \Phi_k \sum_{j=1}^{J} l_{ij}\phi(\mu_j) - \Theta_k \sum_{j=1}^{J} l_{ij}\theta(\mu_j)\Big), \tag{5.14}$$

resulting in two projections instead of K. Substituting eq.(5.14) in eq.(4.8) and applying eq.(4.15) results in the IMPACT algorithm:

$$\mu_j^{n+1} = \mu_j^n + \frac{\phi'_j \cdot \sum_{i=1}^{I} l_{ij} e_i Y_i^{\Phi} + \theta'_j \cdot \sum_{i=1}^{I} l_{ij} e_i Y_i^{\Theta}}{\phi'_j \cdot \sum_{i=1}^{I} l_{ij} M_i + \theta'_j \cdot \sum_{i=1}^{I} l_{ij} N_i}, \tag{5.15}$$

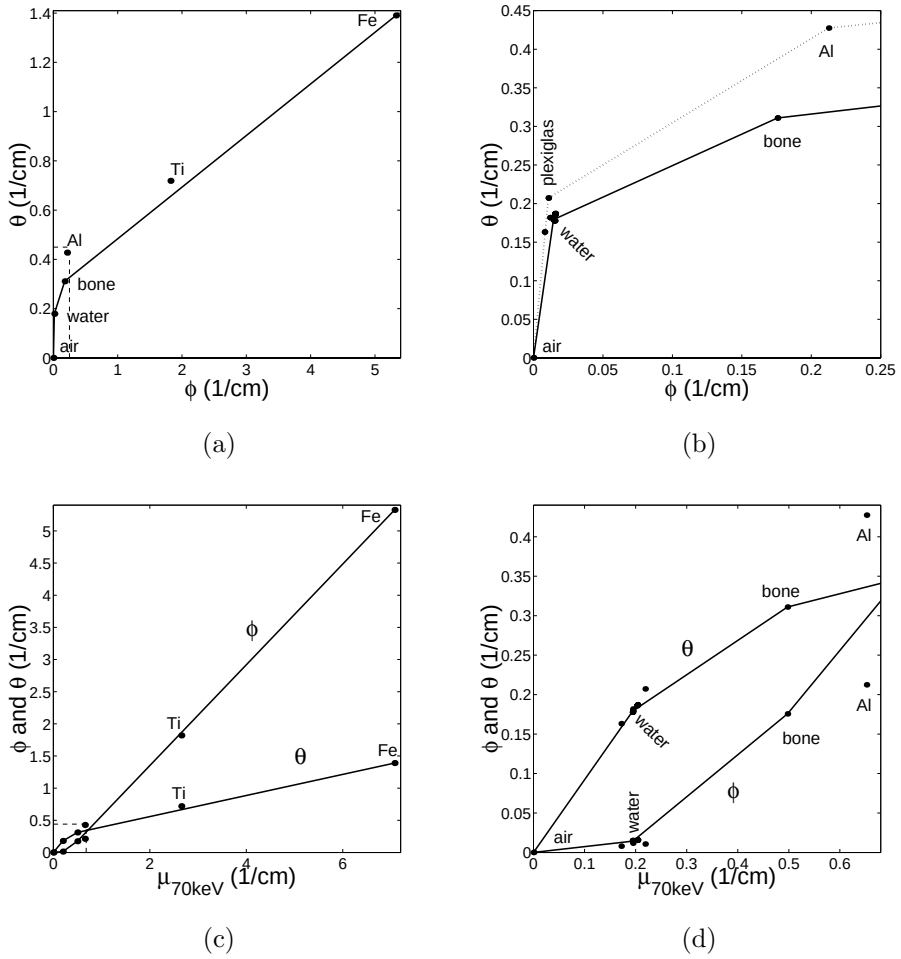

Figure 5.9: *(a) Photo-electric coefficient ϕ versus Compton coefficient θ for the set of base substances [air, water, bone, iron]. (b) Same as (a) but zoomed to the dashed region and including the other substances from table 5.1. (c) Monochromatic linear attenuation coefficient μ_{70keV} versus ϕ and θ for the set of base substances [air, water, bone, iron]. (d) Same as (c) but zoomed to the dashed region and including the other substances from table 5.1.*

where

$$\phi'_j = \left(\frac{\partial \phi}{\partial \mu}\right)\Big|_{\mu_j^n}$$

$$\theta'_j = \left(\frac{\partial \theta}{\partial \mu}\right)\Big|_{\mu_j^n}$$

$$e_i = 1 - \frac{y_i}{\hat{y}_i}$$

$$M_i = \Big(\sum_{h=1}^{J} l_{ih}\phi'_h\Big) \cdot \Big(Y_i^{\Phi\Phi} \cdot e_i + \frac{y_i \cdot (Y_i^{\Phi})^2}{\hat{y}_i^2}\Big) + \Big(\sum_{h=1}^{J} l_{ih}\theta'_h\Big) \cdot \Big(Y_i^{\Phi\Theta} \cdot e_i + \frac{y_i \cdot Y_i^{\Phi} \cdot Y_i^{\Theta}}{\hat{y}_i^2}\Big)$$

$$N_i = \Big(\sum_{h=1}^{J} l_{ih}\phi'_h\Big) \cdot \Big(Y_i^{\Phi\Theta} \cdot e_i + \frac{y_i \cdot Y_i^{\Phi} \cdot Y_i^{\Theta}}{\hat{y}_i^2}\Big) + \Big(\sum_{h=1}^{J} l_{ih}\theta'_h\Big) \cdot \Big(Y_i^{\Theta\Theta} \cdot e_i + \frac{y_i \cdot (Y_i^{\Theta})^2}{\hat{y}_i^2}\Big)$$

$$Y_i^{\Phi} = \sum_{k=1}^{K} \Phi_k \cdot \hat{y}_{ik}$$

$$Y_i^{\Theta} = \sum_{k=1}^{K} \Theta_k \cdot \hat{y}_{ik}$$

$$Y_i^{\Phi\Phi} = \sum_{k=1}^{K} \Phi_k \cdot \Phi_k \cdot \hat{y}_{ik}$$

$$Y_i^{\Phi\Theta} = \sum_{k=1}^{K} \Phi_k \cdot \Theta_k \cdot \hat{y}_{ik}$$

$$Y_i^{\Theta\Theta} = \sum_{k=1}^{K} \Theta_k \cdot \Theta_k \cdot \hat{y}_{ik}$$

$$\hat{y}_{ik} = b_{ik} \cdot \exp\Big(-\Phi_k \sum_{j=1}^{J} l_{ij}\phi(\mu_j^n) - \Theta_k \sum_{j=1}^{J} l_{ij}\theta(\mu_j^n)\Big),$$

Intermediate results are given in appendix A.4. At the points of inflection, ϕ'_j and θ'_j are defined as

$$\begin{aligned} \phi'_j &= \frac{1}{2}\lim_{\epsilon\to 0}\big[(\frac{\partial\phi}{\partial\mu})\big|_{\mu_j^n-\epsilon} + (\frac{\partial\phi}{\partial\mu})\big|_{\mu_j^n+\epsilon}\big] \\ \theta'_j &= \frac{1}{2}\lim_{\epsilon\to 0}\big[(\frac{\partial\theta}{\partial\mu})\big|_{\mu_j^n-\epsilon} + (\frac{\partial\theta}{\partial\mu})\big|_{\mu_j^n+\epsilon}\big]. \end{aligned} \tag{5.16}$$

Finally, the result is convolved with a Gaussian smoothing kernel with standard deviation σ to suppress Gibbs overshoots at sharp edges [140].

The resulting image represents the monochromatic linear attenuation coefficient at 70 keV. Applying the functions $\phi(\mu_j)$ and $\theta(\mu_j)$ to these images yields the photoelectric and Compton scatter images at 70 keV. Using eq.(5.7), reconstructions at other energies (even outside the used spectrum) are obtained.

Every iteration requires 4 projections (projection of ϕ, θ, ϕ', and θ'), and 4 backprojections (backprojection of $e_i Y_i^{\Phi}$, $e_i Y_i^{\Theta}$, M_i, and N_i).

5.3.3 Post-reconstruction approach

We implemented the post-reconstruction approach for comparison with IMPACT. Our implementation is essentially the version of Fuchs et al [39]. All other methods [55, 59, 72, 74, 89, 100, 107, 124, 130] are either limited to two or three substances, or apply some extra approximations because of limited computational power at the time they were invented. Similar to IMPACT, a set of base substances (e.g. [air, water, bone, iron]) is chosen, assuming that every pixel contains a mixture of two adjacent base substances. An initial FBP reconstruction is calculated from the original sinogram. For every substance, an image containing the substance concentrations is segmented and each image is projected into a substance sinogram. Every substance sinogram pixel contains the total amount of that substance along the corresponding projection line. For every sinogram pixel, the monochromatic projections (at E_0) and the polychromatic projections (based on a K-energy spectrum) are calculated. The difference between the monochromatic and the polychromatic sinogram is added to the original sinogram and a new FBP reconstruction is obtained. This process is repeated N times. In the remainder, we refer to this method as IBHC (iterative beam hardening correction). In our implementation, computation time increases linearly with the number of substances considered but is still much lower than for maximum likelihood or related iterative algorithms.

5.3.4 Methods

5.3.4.1 Simulations

Our CT-simulator is described and validated in chapter 3. We defined 4 circular water phantoms, each with a diameter of 19 cm. Phantom 9 consists of water only and is used to study the cupping artifact in the presence of one single substance. Phantom 10 contains 4 circular bone regions (ø = 3 cm and 1 cm) and is used to study beam hardening in the presence of at least two different substances. Phantom 11 contains 8 circular regions (ø = 3 cm) of fat, aluminum, plexiglas, lung, brain, bone, blood, and soft tissue (in clockwise order and starting from the top). This is used to investigate how critical is the set of base substances assumed by IMPACT and IBHC. Phantom 12 is similar to phantom 10, but the two smallest cylindrical inserts are now made of iron (ø = 1 cm). This phantom was designed to study beam hardening in the presence of metal objects.

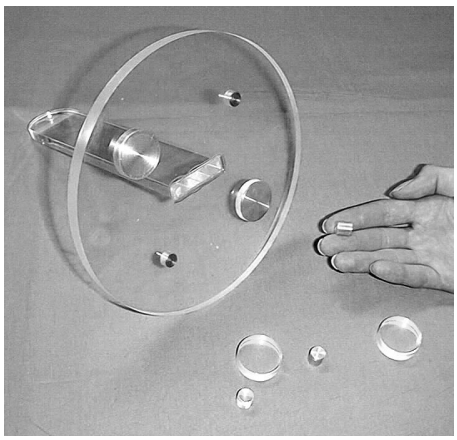

Figure 5.10: *Picture of the plexiglas phantom.*

Simulation parameters were adjusted to the Siemens Somatom Plus 4 CT-scanner with fixed focal spot and a 0.75 s rotation. Both monochromatic and polychromatic (by summing photons at 50 discrete energy levels) simulations were performed. A simulated spectrum b_{ik} provided by Siemens and corresponding to a nominal tube voltage of 140 kV was used (figure 5.8). Generally, no noise or scatter was included, because we want to focus on beam hardening artifacts. For phantom 12, an extra simulation was performed *with* noise ($b_i = 10^5$ photons) to investigate the importance of the noise model in the presence of metal objects.

5.3.4.2 Measurements

Three phantoms were scanned on a Siemens Somatom Plus 4 CT-scanner. Phantom 13 is a circular plexiglas phantom (figure 5.10) with thickness 1 cm, a diameter of 19 cm, and containing 4 aluminum cylinders (ø = 1 cm and 3 cm). This phantom is comparable to software phantom 10. We chose plexiglas and aluminum instead of water and bone for practical reasons. This phantom is used to study beam hardening in the absence of metal objects. Phantom 14 is similar to phantom 13, but the two smallest cylindrical inserts are now made of iron (ø = 1 cm). This phantom is comparable to software phantom 12 and it is used to study beam hardening in the presence of metal objects. Phantom 15 is a skull phantom (borrowed from Siemens): a human skull filled and surrounded by plexiglas. The skull phantom is used to study beam hardening on a clinically more relevant phantom.

We used sequential scan mode with fixed focal spot, a nominal slice thickness of 1.0 mm, a 0.75 s rotation, a nominal tube voltage of 140 kV or 120 kV (skull), and a tube current of 206 mA or 240 mA (skull). The raw data were transfered to a PC for further processing using our own reconstruction software.

5.3.4.3 Reconstruction

All simulations and measurements were reconstructed with:

- FBP: using a Hamming window with a cutoff frequency of half the maximum frequency.
- ML-TR: using 50 iterations of 100 subsets + 50 iterations of 10 subsets [67], $\sigma = 0.9$ pixels. σ is the standard deviation of the Gaussian smoothing kernel and was chosen so that ML-TR and IMPACT resulted in images with the same degree of edge smoothing as the FBP and IBHC reconstructions.
- IMPACT: using 50 iterations of 100 subsets + 50 iterations of 10 subsets, $\sigma = 0.9$ pixels, $K = 20$, $E_0 = 70$ keV. Unless stated differently, [air, water, bone, iron] was used as set of base substances for the simulations (solid line in figure 5.9 (b)) and [air, plexiglas, aluminum, iron] was used as set of base substances for the measurements (dotted line in figure 5.9 (b)).
- IBHC: $N = 5$, $K = 20$, $E_0 = 70$ keV. The same sets of base substances were used as for IMPACT.

A simulated spectrum b_{ik} provided by Siemens (figure 5.8) was used for both IMPACT and IBHC.

5.3.5 Results

5.3.5.1 Simulations

All simulation results are shown using a windowing interval $\mu = [0.175\,;\,0.215]\,\mathrm{cm}^{-1}$ (centered at μ_{water}), which corresponds to a window of 200 HU and a level of 0 HU. The images are $20\,\mathrm{cm} \times 20\,\mathrm{cm}$ and 256×256 pixels.

Figure 5.11 shows the reconstructions of phantom 9. The white curves represent the middle rows of the respective images. The dotted white curves represent FBP of the monochromatic simulation, which is used as reference. For the polychromatic simulation, both FBP (a) and ML-TR (not shown) result in a substantial amount of cupping: the values are depressed toward the center of the object. This cupping is entirely eliminated both with IMPACT (b) and IBHC (not shown). The perfect overlap of the white curves in (b) shows that the images are also quantitatively correct.

Figure 5.12 shows the reconstructions of phantom 10. FBP of the monochromatic simulation (a) is used as reference. For the polychromatic simulation, both FBP (b) and ML-TR (not shown) exhibit severe artifacts: the bone inserts are connected by dark streaks. These streaks are effectively eliminated both with IMPACT (c) and IBHC (d). IMPACT requires at least 50 iterations for convergence, IBHC only 2.

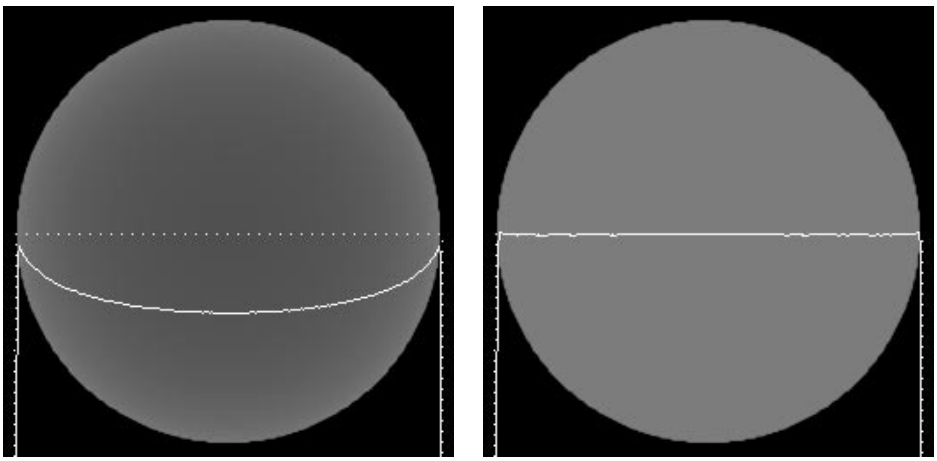

(a) (b)

Figure 5.11: *Phantom 9 (simulation): (a) FBP, (b) IMPACT. The white curves represent the middle rows of the respective images. The dotted white curves represent FBP of the monochromatic simulation.*

Figure 5.13 shows the reconstructions of phantom 11. FBP of the monochromatic simulation (a) is used as reference. For the polychromatic simulation, both FBP (b) and ML-TR (not shown) exhibit severe artifacts: the bone and aluminum inserts are connected by dark streaks. These streaks are reduced but not eliminated both with IMPACT (c) and with IBHC (d). Using an extended set of base substances [air, water, plexiglas, bone, aluminum, iron] beam hardening artifacts are effectively eliminated both with IMPACT (e) and IBHC (f). It appears that aluminum and plexiglas are too far separated from the ϕ-θ-curve defined by [air, water, bone, iron], while all human tissues (fat, lung, brain, blood, soft tissue, ...) are sufficiently close to water.

Figure 5.14 shows the reconstructions of phantom 12. FBP of the monochromatic simulation (a) is used as reference. It shows some streak artifacts connecting the metal and bone inserts. These streaks are not due to beam hardening, but to other effects such as the NLPV effect [75] and aliasing [8, 22, 142]. For the polychromatic simulation, both FBP (b) and ML-TR (not shown) exhibit severe artifacts: the bone and metal inserts are connected by dark streaks. The streaks that were present in (b) but not in (a) are eliminated both with IMPACT (c) and IBHC (e). The remaining streaks in (c) and (e) are similar to the streaks in (a), which indicates that the beam hardening artifacts are effectively eliminated. (d) and (f) show the IMPACT and IBHC results for the simulation *with* noise ($b_i = 10^5$ photons). In both images beam hardening artifacts are partially masked by noise artifacts. Clearly, the IMPACT reconstruction benefits from the correct noise model resulting in less severe noise artifacts. This is shown quantitatively by calculating the standard deviation in an excentric circular water region. This resulted in a standard

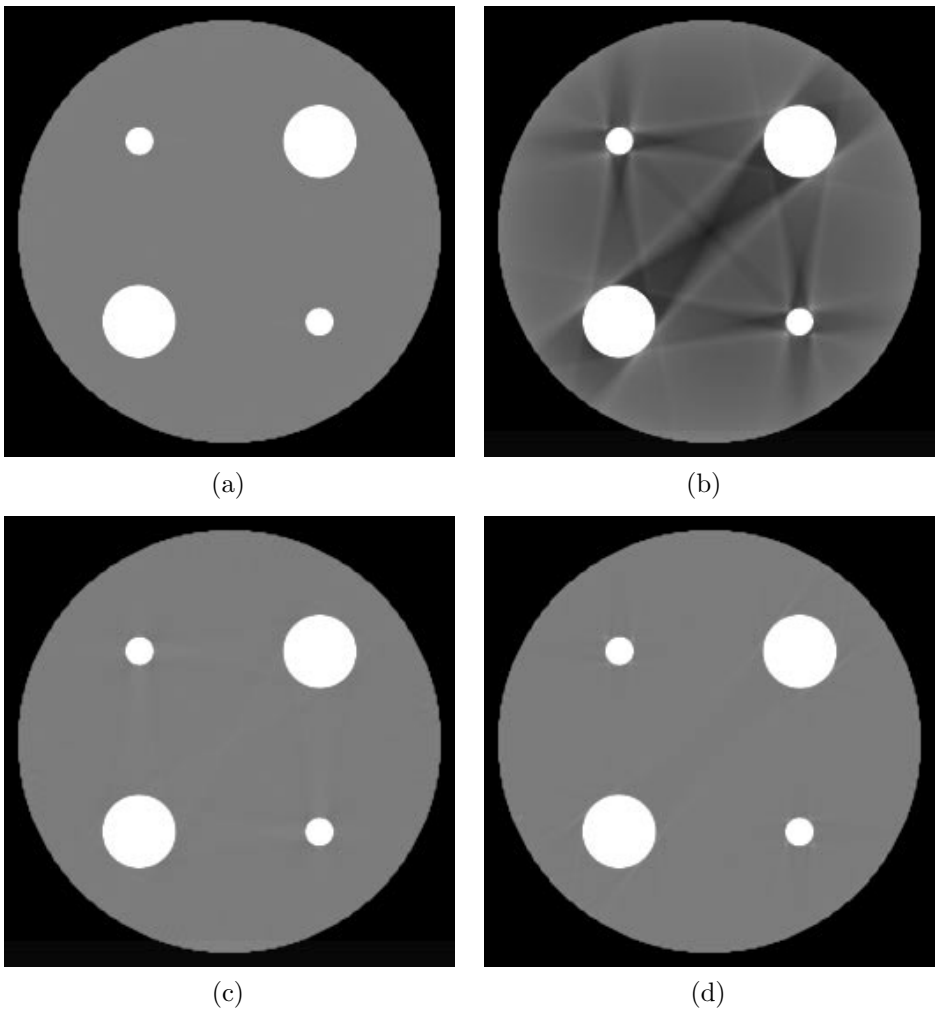

Figure 5.12: *Phantom 10 (simulation): (a) FBP (mono), (b) FBP, (c) IMPACT, (d) IBHC.*

deviation of 0.0028 cm^{-1} for IMPACT and 0.0039 cm^{-1} for IBHC.

5.3.5.2 Measurements

All measurement results are shown using a windowing interval $\mu = [0.20\,;\,0.24]\,\mathrm{cm}^{-1}$ (centered at $\mu_{\mathrm{plexiglas}}$), which corresponds to a window of 200 HU and a level of 125 HU. The images are $20\,\mathrm{cm} \times 20\,\mathrm{cm}$ and 256×256 pixels.

The left column of figure 5.15 shows the reconstructions of phantom 13. The FBP reconstruction (a) exhibits a number of dark beam hardening streaks. The streaks are strongly reduced both with IMPACT (c) and IBHC (e).

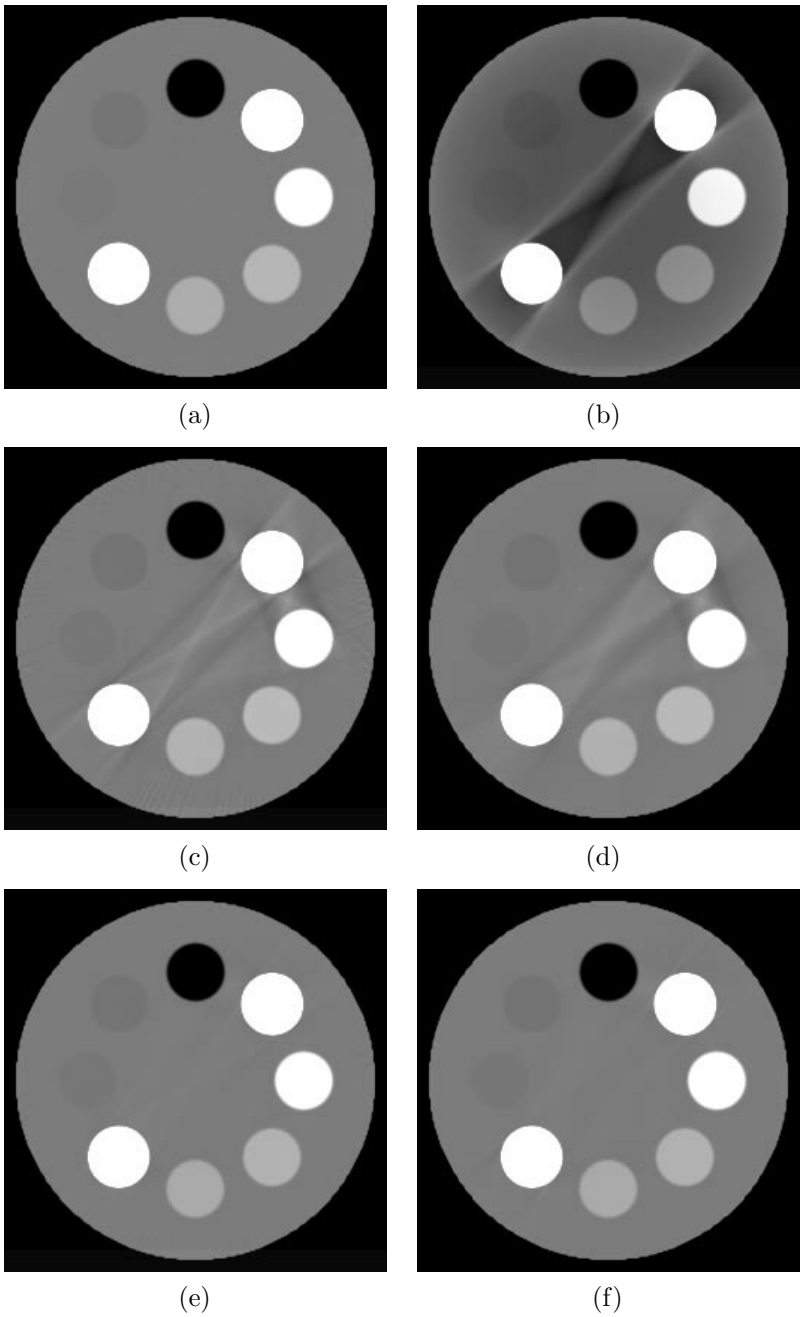

Figure 5.13: *Phantom 11 (simulation): (a) FBP (mono), (b) FBP, (c) IMPACT, (d) IBHC, (e) IMPACT with extended set of base substances, (f) IBHC with extended set of base substances.*

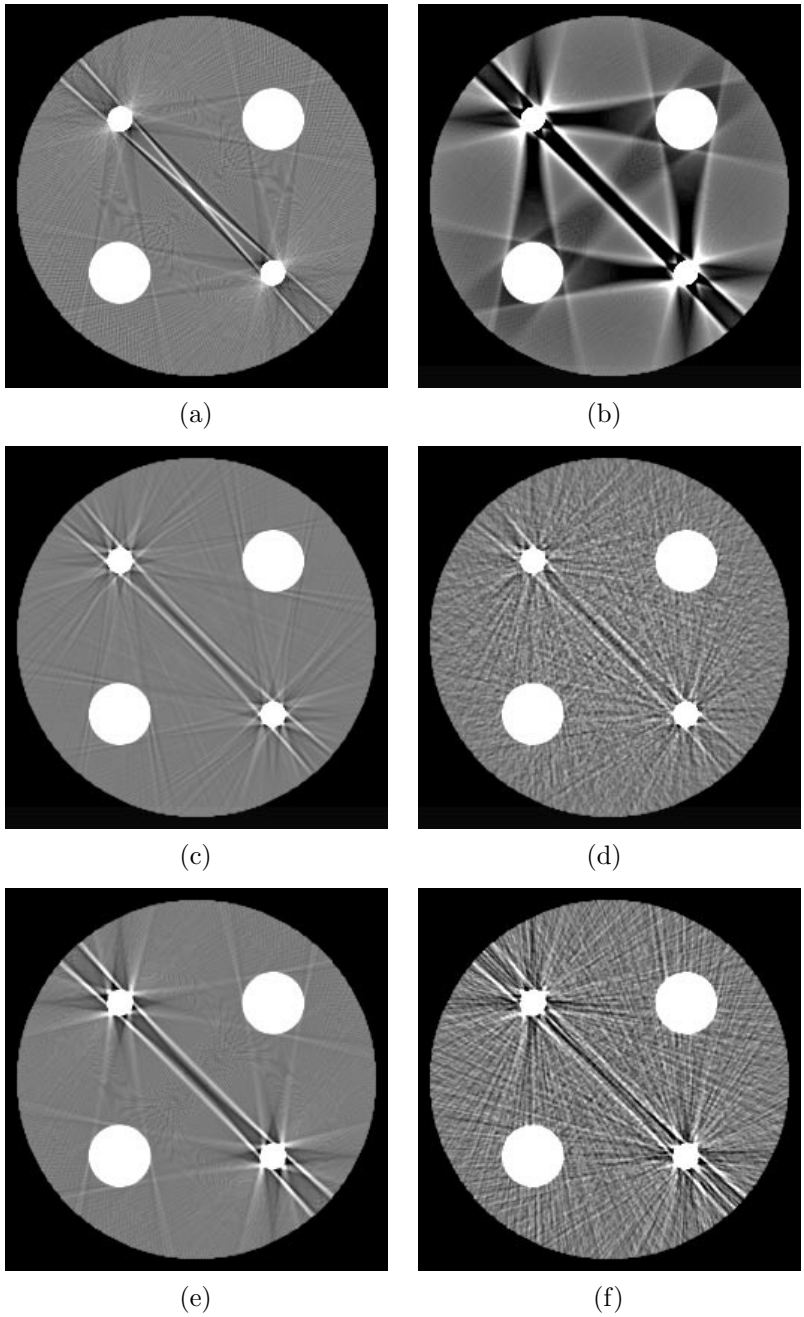

Figure 5.14: *Phantom 12 (simulation): (a) FBP (mono), (b) FBP, (c) IMPACT, (d) IMPACT (with noise), (e) IBHC, (f) IBHC (with noise).*

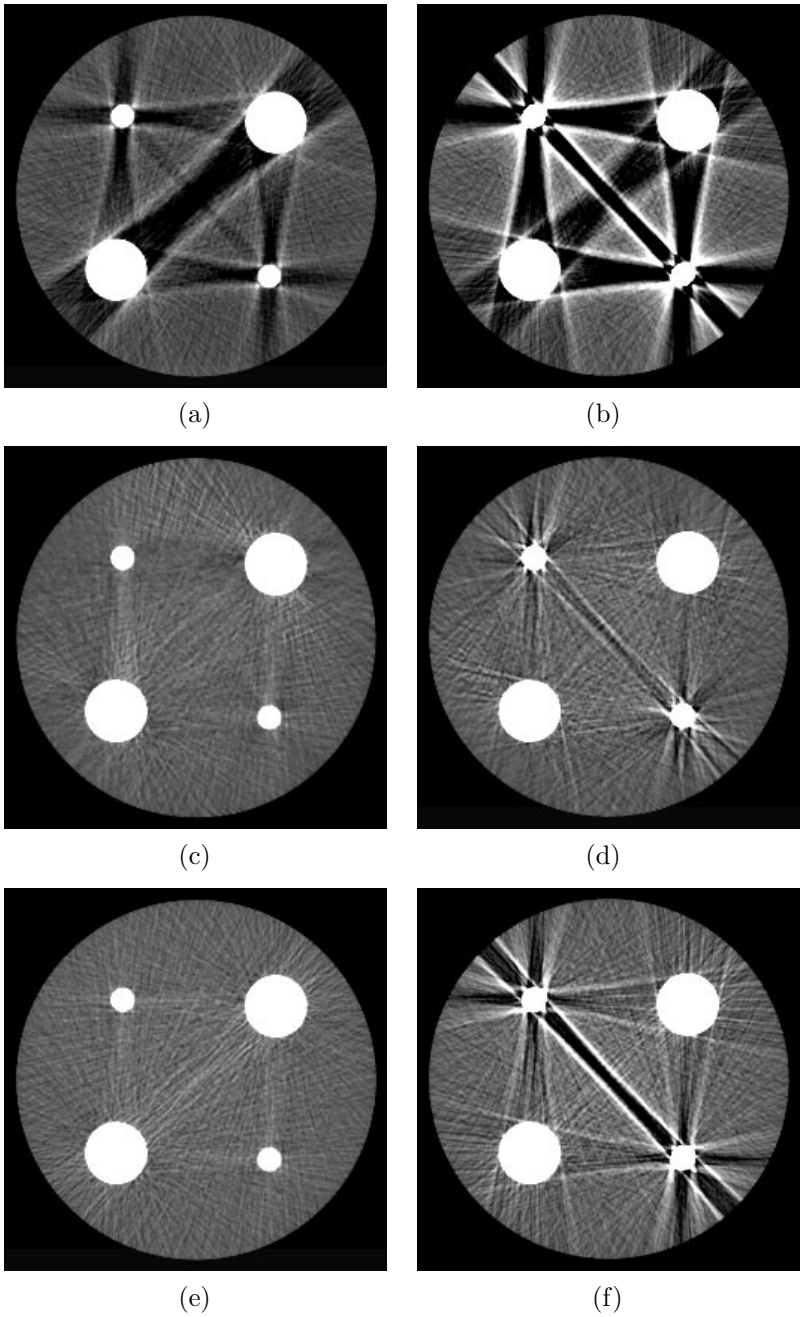

Figure 5.15: *Phantom 13 and phantom 14 (measurements): (a-b) FBP, (c-d) IMPACT, (e-f) IBHC.*

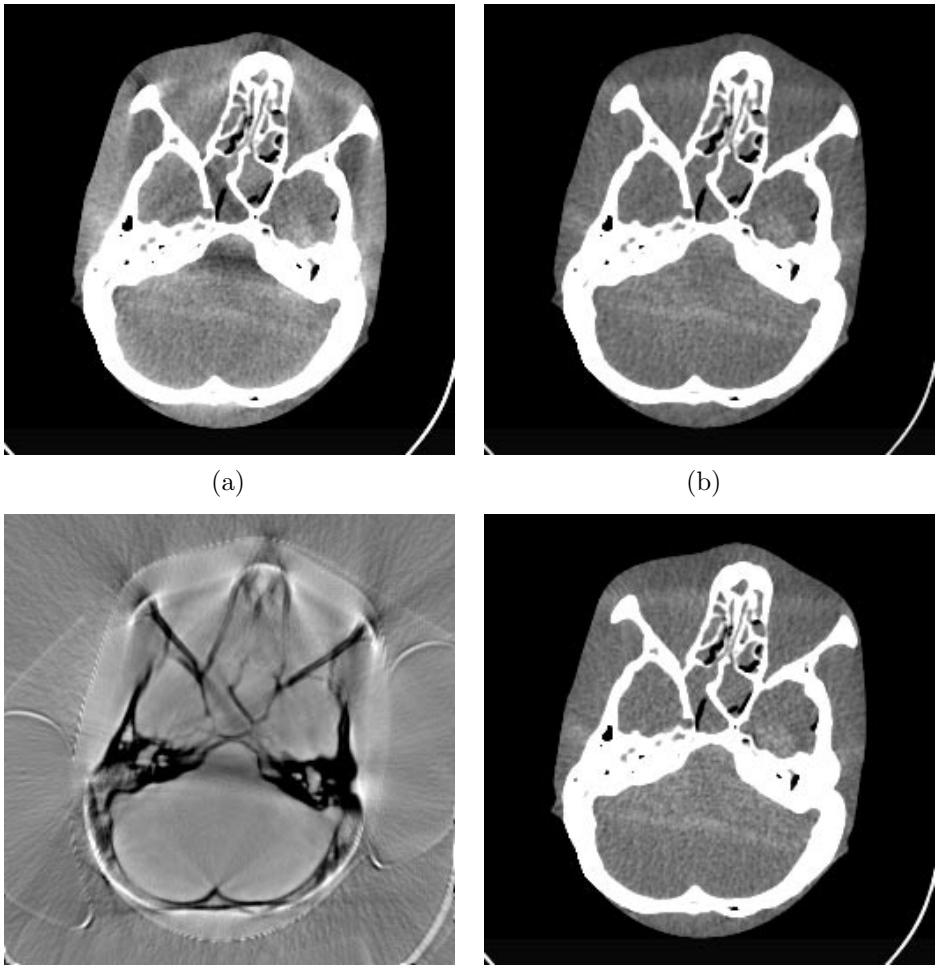

(a) (b)

(c) (d)

Figure 5.16: *Phantom 15 (measurement): (a) FBP, (b) IMPACT, (c) substraction of IMPACT and FBP, (d) IBHC.*

The right column of figure 5.15 shows the reconstructions of phantom 14. The FBP reconstruction (b) exhibits severe streak artifacts. The dark streaks are reduced both with IMPACT (d) and IBHC (f). Comparison with phantom 12 indicates that the remaining streaks are mainly due to other effects, such as noise, scatter, the NLPV effect, and aliasing. The remaining dark streak in (f) – probably due to scatter – is more prominent than in (d). This also suggests that IMPACT benefits from its correct noise model, which makes IMPACT robust against errors corresponding to strongly attenuated measurements.

Figure 5.16 shows the reconstructions of phantom 15. The FBP reconstruction

(a) exhibits dark beam hardening streaks. These streaks are effectively eliminated with IMPACT (b) and IBHC (d). [air, plexiglas, bone, iron] was chosen as set of base substances. Substracting IMPACT from FBP shows where the correction for beam hardening artifacts is most prominent (c). It also shows a strong reduction of the background noise. Note also that the bone regions are dark. This is mainly due to the fact that the IMPACT reconstruction represents values at 70 keV, while the FBP reconstruction represents averages over the entire spectrum.

5.3.6 Discussion

We have derived a new algorithm that combines three existing approaches. Firstly, it is a maximum likelihood iterative algorithm, which allows to use a correct noise model and an acquisition model that can be extended to other sources of artifacts, in this case to polychromaticity. Secondly, similar to the dual energy approach, the attenuation coefficient is decomposed into a photo-electric and a Compton scatter component. This is a natural decomposition that strongly reduces the number of degrees of freedom without loss of generality. And thirdly, similar to IBHC, the domain of the linear attenuation coefficient is confined to mixtures of known substances.

The quality of the IMPACT reconstructions is, in the absence of metal objects, not better than the IBHC reconstructions: both result in effective beam hardening correction. The results of phantom 12 and 13 indicate that, in the presence of metal objects, IMPACT benefits from its correct noise model resulting in less severe noise and other artifacts. A more extended evaluation of the algorithm with respect to noise, spatial resolution, quantitative accuracy, and degree of artifacts is required after including models for scatter and the NLPV effect.

One important parameter is the assumed set of base substances. The simulations of phantom 11 show that this set is not very critical provided that the substances in the scanning plane are not too far separated from the assumed ϕ-θ-relationship. It is advisable to include in the ϕ-θ-relationship all substances that are known to be present in the scanning plane. Unlike in IBHC, the number of these substances can become large without increase in algorithmic complexity or computational load. This also suggests a way of increasing the speed of IBHC: decomposing the linear attenuation coefficient into a photo-electric and Compton scatter components – just like in IMPACT – amounts in two projections per iteration instead of a projection per iteration for each modeled substance.

Another important parameter is the used spectrum. As shown by the results, the simulated spectrum provided by the manufacturer results in effective beam hardening correction. The number of energy levels K can be increased with only marginal increase in computation time. The results show that using $K = 20$ is sufficient for an effective beam hardening correction. For larger objects it could be opportune to take into account the non-uniformity of the spectrum due to the bow-tie filter.

The main drawback of IMPACT is the high computation time. Therefore, it is

probably advisable to use IBHC as long as no metal artifacts are present. As a first order approximation we can write reconstruction time as

$$t \sim \frac{\text{nriter} \cdot \text{nrdet} \cdot \text{nrviews} \cdot \text{imsize} \cdot \text{nrslices} \cdot \text{complexity}}{\text{CPU}} \tag{5.17}$$

where nriter is the number of iterations, nrdet is the number of detector elements, nrviews is the number of views, imsize is the number of rows or columns in the reconstruction, nrslices is the number of slices, complexity is the number of (back)projections per iteration and CPU is the CPU-speed. The complexity is 1 for FBP, 3 for ML-TR (or 2 if the denominator is kept constant), 8 for IMPACT, and $(1 + \text{number of materials} + 1/\text{nriter})$ for IBHC. Typically, using a Pentium III-800 Linux PC, computation time is a few hours for nrdet=768, nrviews=1056, nriter=100, imsize=512, nrslices=1, and complexity=8. This may prevent IMPACT from being used in clinical routine the next few years.

In our opinion, the main contribution of this work is the incorporation of a polychromatic model into a maximum likelihood iterative reconstruction algorithm. This allows to extend existing maximum likelihood approaches with beam hardening correction. The method requires only one scan (in contrast with the dual energy approach), and both the number of discrete energies and the number of substances taken into account can be increased with only marginal increase in computation time (in contrast with IBHC). We have shown in section 5.2 that ML-TR is promising for metal artifact reduction, mainly thanks to the noise model. We now have extended this method with a model for polychromaticity. It is confirmed that improving the acquisition model results in reduced artifacts. The algorithm can further be extended by including other effects such as scatter and the NLPV effect in the acquisition model. A common advantage of IMPACT and IBHC is that the monochromatic reconstructions allow a direct quantitative interpretation, compared to classical images, which are averages over the used spectrum. The difference between IMPACT and other beam hardening correction approaches (IBHC in particular) can be summarized as follows. Instead of correcting the data in order to obey certain assumptions imposed by the reconstruction algorithm, the reconstruction process is adapted to the data by incorporating a more accurate acquisition model. Polychromatic data are not transformed into monochromatic data, but the algorithm takes into account that the measurements actually are polychromatic.

5.3.7 Conclusion for IMPACT

We have presented an iterative maximum likelihood algorithm for CT (IMPACT) that prevents beam hardening artifacts. Excellent results were obtained on simulations and phantom measurements. The algorithm has been compared to the post-reconstruction approach, and the degree of beam hardening correction was comparable for both algorithms. In the presence of metal objects, IMPACT benefits from its Poisson noise model, resulting in less severe noise and other artifacts. This indicates that metal artifact reduction is a promising application for this new algorithm. Section 5.2 has investigated the importance of the correct noise model.

This section has addressed a second important cause of metal artifacts, namely beam hardening. The algorithm should further be extended to include a prior, a model for scatter, and a model for the NLPV effect. A strong reduction of computation time is required before it can be used routinely.

5.4 Transaxial NLPV effect

This section is based on [27] and presents three algorithms for correction of the tNLPV effect. The origin of the tNLPV effect is discussed in detail in section 3.4.3.3. In [75] two possible correction methods for the tNLPV effect are proposed. The averaging over the rotation interval is not taken into account and the correction methods are limited by the assumption that a beam is made up of a set of parallel lines. In [10] a maximum-likelihood algorithm using a simple finite beam-width model is presented, aiming at improved imaging of low-contrast tissue sub-structures, increased spatial resolution, and low dose reconstruction. In this section, three new correction methods are presented, taking into account both the finite rotation intervals and the actual size of the focal spot and the detector elements. The first method consists of a pre-correction step applied directly to the measured sinogram. The two other methods are adaptations of ML-TR (section 4.3), and can be generalized for other iterative algorithms. A number of software phantoms with sharp edges were simulated and reconstructed using FBP and using the three presented correction methods. All three methods result in substantial artifact reduction.

5.4.1 Algorithms

5.4.1.1 Algorithm 1

Consider the projections p_i for all scanned X-ray beams i. Physically, these are obtained by intensity-averaging the samples p_{is} for all projection line samples s of beam i:

$$p_i = -\ln \frac{1/S \sum_{s=1}^{S} I_0 \cdot \exp(-p_{is})}{I_0}, \tag{5.18}$$

where S is the product of the number of source samples F, the number of detector samples D, and the number of view or rotation samples V (see figures 3.4 and 3.6). What we would like to have, are the attenuation-averaged projections $\bar{p}_i$:

$$\bar{p}_i = 1/S \sum_{s=1}^{S} p_{is}. \tag{5.19}$$

Assuming we knew p_{is}, we could directly calculate $\bar{p}_i$. Unfortunately, p_{is} is not observable, but we can estimate it from p_i, and iteratively update the estimate by comparing the calculated measurement $\hat{p}_i$ with the actual measurement p_i. This is schematically depicted in figure 5.17. We now redefine the samples s by assuming

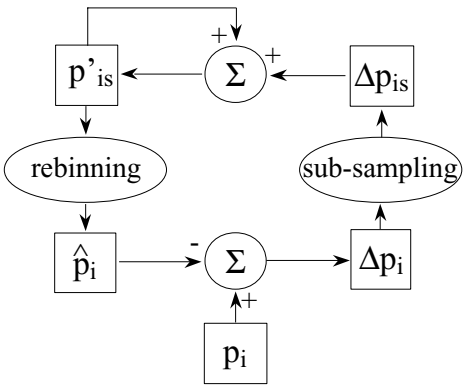

Figure 5.17: *Algorithm 1: iteration scheme for estimating* p'_{is}.

that every detector elements is made up of D smaller detector elements, and that every view is made up of V views with a fraction of the original rotation interval. The finite size of the source is taken into account differently (see below). We explain the steps in figure 5.17 in more detail:

1. The first estimate of p'_{is} is obtained by sub-sampling the measured sinogram p_i using bilinear interpolation.

2. p'_{is} is rebinned to $\hat{p}_i$ by intensity-averaging the corresponding pixels. This requires some more explanation. Going over to matrix notation, $\hat{p}_i$ becomes a matrix $\hat{P}$ with M rows and N columns, and p'_{is} becomes a matrix P' with $M \cdot V$ rows and $N \cdot D$ columns. $\hat{P}$ is calculated from P' as follows:

$$\hat{P} = -\ln\big(< \exp(-P') > \big), \tag{5.20}$$

   where <> is an averaging operation within the original sinogram pixels, depicted more in detail in figure 5.18. Each row (or view) is obtained as an average over all view samples. Each column (detector element) is obtained as a weighted average over all detector samples. Here we use a trapezoidal weighting mask which is obtained as the convolution of two rectangular masks: one for the width of the detector elements and one for the width of the focal spot, taking into account the geometric magnification.

3. The error sinogram $\Delta p_i = p_i - \hat{p}_i$ is calculated and sub-sampled using bilinear interpolation, giving Δp_{is}.

4. Δp_{is} is added to the current estimate p'_{is}.

5. After a number of iterations, p'_{is} is rebinned using attenuation-averaging, resulting in a corrected sinogram $\bar{p}_i$. In matrix notation:

$$\bar{P} =< P' > . \tag{5.21}$$

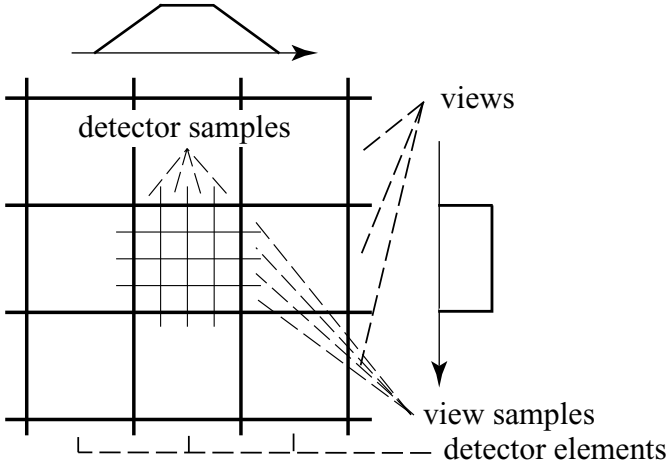

Figure 5.18: *The averaging operation used in algorithm 1. Each row (or view) is obtained as an average over all view samples. Each column (detector element)is obtained as a weighted average over all detector samples.*

This method is actually an iterative deconvolution approach. There is not enough information to recover the sub-sampled projections p_{is}. In fact, the number of solutions is infinite. However, assuming that the p_{is} is a relatively smooth function, we hypothesize that the bilinear interpolation approach results in a reasonable recovery of p_{is},allowing to at least partially reduce the error $p_i - \bar{p}_i$.

5.4.1.2 Algorithm 2

Algorithms 2 and 3 are extensions of ML-TR (section 4.3). We now replace the calculation of $\hat{y}_i$ in eq.(4.2) with a more correct calculation using the sub-sampled projections:

$$\hat{y}_i = \sum_{s=1}^{S} \frac{b_i}{S} \cdot \exp(-\sum_{j=1}^{J} l_{ijs}\mu_j), \tag{5.22}$$

where l_{ijs} is the effective intersection length of projection line sample s in beam i with pixel j. The number of pixels J is adjusted so that the pixel size is comparable to the distance between the beam samples. After a number of iterations, the result is convolved with a Gaussian smoothing kernel and rebinned to normal resolution. The Gaussian smoothing is used as equivalent of the Hamming window used with FBP.

5.4.1.3 Algorithm 3

A more fundamental approach is to start from the acquisition model in eq.(5.22), and to repeat the derivation of ML-TR for this new acquisition model. Substituting

eq.(5.22) in eq.(4.8) and applying eq.(4.15) results in

$$\mu_j^{n+1} = \mu_j^n + \frac{\sum_{i=1}^{I}\sum_{s=1}^{S} l_{ijs}\cdot \hat{y}_{is}(1-y_i/\hat{y}_i)}{\sum_{i=1}^{I}\sum_{s=1}^{S} l_{ijs}\cdot\left[\sum_{h=1}^{J} l_{ih}\right]\cdot \hat{y}_{is}}, \tag{5.23}$$

where

$$\hat{y}_{is} = \frac{b_i}{S}\cdot\exp(-\sum_{j=1}^{J} l_{ijs}\mu_j).$$

Intermediate results are given in appendix A.5. Again, the number of pixels J is adjusted so that the pixel size is comparable to the distance between the beam samples, and after a number of iterations, the result is convolved with a Gaussian smoothing kernel and rebinned to normal resolution.

5.4.2 Simulations

Our CT-simulator is described and validated in chapter 3. Three software phantoms were simulated. Phantom 16 (figure 5.19 (a)) consists of a bone triangle ($\mu_{\text{bone}} = 0.4974\ \text{cm}^{-1}$) surrounded with a number of circular details ($\mu_{\text{details}} = 0.0249\ \text{cm}^{-1}$); the background is air ($\mu_{\text{air}} \approx 0.0\ \text{cm}^{-1}$). Phantom 17 (figure 5.19 (c)) is the inverse of phantom 16, obtained by subtracting phantom 16 from a circular bone object ($\varnothing = 4.8$ cm). It is included to show that artifact reduction is not limited to regions of low attenuation. Phantom 18 (figure 5.19 (e)) is a circular water phantom containing two iron inserts ($\varnothing = 0.25$ cm, $\mu = 7.0748\ \text{cm}^{-1}$), two circular bone inserts ($\varnothing = 0.75$ cm, $\mu = 0.4974\ \text{cm}^{-1}$), and two details ($\varnothing = 0.25$ cm, $\mu_{\text{plexiglas}} = 0.2187\ \text{cm}^{-1}$, and $\mu_{\text{fat}} = 0.1717\ \text{cm}^{-1}$). This allows to evaluate the algorithms in the presence of metal artifacts.

Simulations were performed with and without the tNLPV effect, by using intensity-averaging and attenuation-averaging (see above). Monochromatic simulations were performed. No noise or scatter was included. The simulations without the tNLPV effect were reconstructed with FBP. The simulations with the tNLPV effect were reconstructed with FBP and with the three proposed algorithms. Simulation parameters were adjusted to the Siemens Somatom Plus 4, but restricted to a FOV of 5 cm to save computation time. The number of detectors is 95 and the number of views 402. The number of samples is 4 for the source, 8 for the detector elements and 6 for the rotation interval. No cross-talk or afterglow were included.

FBP was performed using a Hamming window with a cutoff frequency of half the sampling frequency. σ, the standard deviation of the Gaussian post-smoothing kernel applied to the iterative methods, was chosen 1.185 pixels so that the images had the same degree of edge smoothing as the FBP reconstructions (with Hamming window). This was determined by visual comparison of profiles through the images. Algorithms 2 and 3 were performed using 256×256 pixels. We used the following iteration scheme: $400 \times 10 + 400 \times 6 + 400 \times 3 + 400 \times 2 + 400 \times 1$, where every first number denotes the number of iterations and every second number denotes the number of subsets. All shown results are 5 cm $\times$ 5 cm and 64×64 pixels, and use a windowing interval of 0.02 cm^{-1}, corresponding to circa 100 HU.

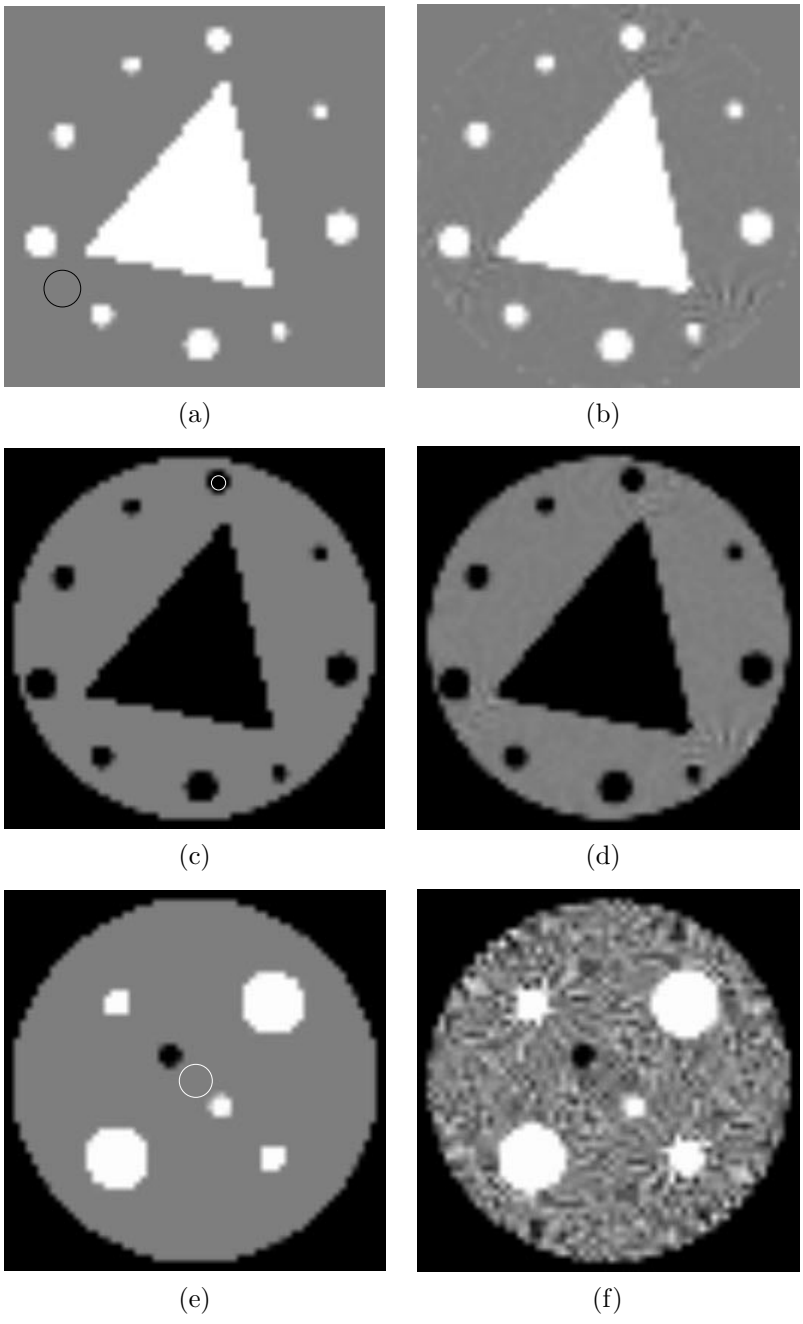

Figure 5.19: *Software phantoms (left) and FBP reconstructions of the simulations without the tNLPV effect (right): (a-b) phantom 16 windowed in interval μ = [-0.01 ; 0.01] cm^{-1}, (c-d) phantom 17 windowed in interval μ = [0.4874 ; 0.5074] cm^{-1}, and (e-f) phantom 18 windowed in interval μ = [0.1846 ; 0.2046] cm^{-1}.*

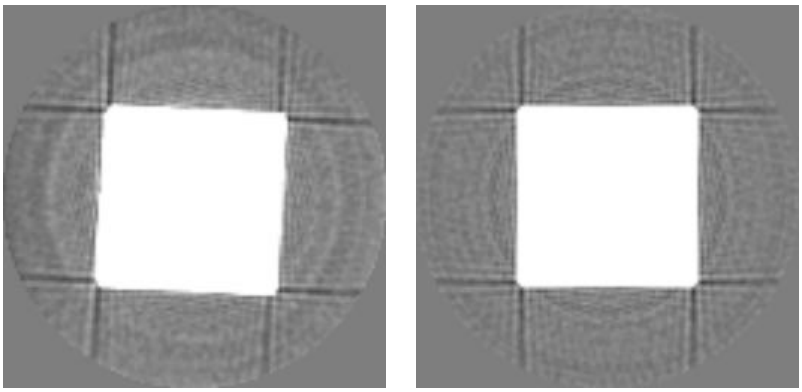

(a) (b)

Figure 5.20: *FBP reconstructions of phantom 19 windowed in interval μ = [-0.01 ; 0.01] cm^{-1}: (a) measurement and (b) simulation.*

5.4.3 Measurements

Phantom 19, a square plexiglas plate with thickness 1 cm and sides of 3 cm, was scanned on a Siemens Somatom Plus 4 CT-scanner. We used sequential scan mode with fixed focal spot, a nominal slice thickness of 1.0 mm, a 0.75 s rotation, a nominal tube voltage of 140 kV, and a tube current of 206 mA. The raw data were transfered to a PC for further processing using our own reconstruction software. For comparison we also simulated phantom 19 using the same parameters as for the measurement. Both were reconstructed using FBP with a Hamming window with a cutoff frequency of half the sampling frequency, a FOV of 6.7 cm, and 128 $\times$ 128 pixels. The results are shown in figure 5.20 using a windowing interval of 0.02 cm^{-1}. In addition to the NLPV artifacts, some low-level aliasing artifacts and ring artifacts are seen. The latter are due to drift in sensitivity of the different detector elements. This effect was also included in the simulations as random variations in detector sensitivity with a standard deviation of 0.05 %.

In a first attempt to validate the proposed correction approach on measurements, we applied algorithm 3 to the measurement of phantom 19. Recently, the gas ionization detectors in the Somatom Plus 4 have been replaced by solid-state detectors. Therefore, we can no longer use the amounts of detector crosstalk and afterglow determined in chapter 3. For now, we assume that both are zero. Nevertheless, all described algorithms are very easily extended to accommodate for these effects. A large number of iterations were performed using 512 $\times$ 512 pixels. A Gaussian post-smoothing kernel with $\sigma = 3$ was applied so that the images had the same degree of edge smoothing as the FBP reconstructions, and the images were rebinned to 128 $\times$ 128 pixels.

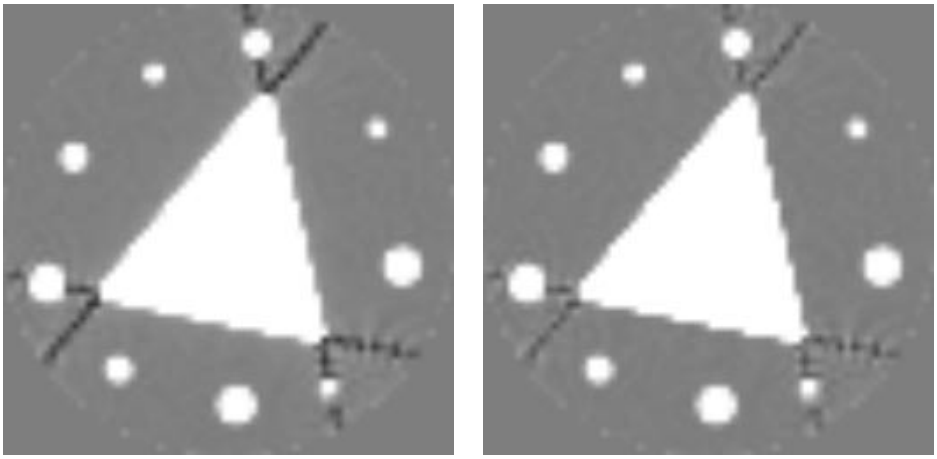

(a) (b)

(c) (d)

Figure 5.21: *Results for phantom 16 windowed in interval μ = [-0.01 ; 0.01] cm^{-1}: (a) FBP, (b-d) algorithms 1 to 3.*

5.4.4 Results and discussion

Figure 5.19 (b, d, f) shows the filtered backprojection reconstructions of the simulation without the tNLPV effect. The only artifacts that are seen are due to aliasing [8, 22, 77, 142, 150]. Aliasing is always present, but is usually not seen. In these cases it is, due to the small windowing interval and due to the presence of strong gradients.

Figure 5.21 shows the results for phantom 16. The uncorrected image (a) shows dark streaks tangent to the edges of the triangle, as expected. With algorithm 1, the streaks are partially reduced (b). Algorithms 2 and 3 offer the best results (c-d).

phantom 16	min	mean	max
FBP -	-1.4288	0.0602	1.5530
FBP +	-6.0115	-0.5660	1.5311
alg 1	-3.7823	-0.0996	1.9691
alg 2	-0.6059	-0.0284	0.3584
alg 3	-1.2209	-0.0672	0.6880

Table 5.2: *Normalized values of the ROI drawn in figure 5.19 (a), for the FBP reconstruction without (FBP -) and with tNLPV effect (FBP +), and the results of algorithms 1, 2, and 3.*

The streaks are almost completely gone (taking into account the narrow windowing). Remarkably, the result for algorithm 2 is even better than for algorithm 3 for the same number of iterations. We attribute this to the fact that the convergence depends on the degree of smoothing in the backprojector. It is a well-established fact that amplifying the high-frequencies (or equivalently, removing a smoothing operation) in the backprojection results in increased convergence speed [114]. For a preliminary quantitative evaluation, we calculated the minimum, mean and maximum value of the region of interest (ROI) drawn in figure 5.19 (a) for all algorithms. The values were normalized for easier comparison: the mean value obtained for the reference image was subtracted from all values followed by a multiplication by 1000:

$$\text{value}_{\text{table}} = (\text{value}_{\text{orig}} - \text{mean}_{\text{ref}}) * 1000. \tag{5.24}$$

Table 5.2 shows the calculated values for the FBP reconstruction without (FBP -) and with tNLPV effect (FBP +), and the results of algorithms 1, 2, and 3. The mean values confirm that the tNLPV effect causes a negative error which is reduced by the three proposed algorithms. The minimum and maximum values show that the correction algorithms effectively modify all erroneous values toward the ideal value. Moreover, they indicate that algorithms 2 and 3 offer a strongly reduced variance.

Figure 5.22 shows the results for phantom 17. Again, the uncorrected image (a) shows dark streaks tangent to the edges of the triangle, as expected. With algorithm 1, the streaks are partially reduced (b). Algorithms 2 and 3 offer the best results (c-d). The streaks are almost completely gone. The result with algorithm 2 is again slightly better than with algorithm 3. The minimum, mean and maximum value of the ROI drawn in figure 5.19 (c) was calculated for all algorithms. Table 5.3 shows the normalized values, analogously to phantom 16. The conclusions are identical to those for phantom 16.

Figure 5.23 shows the results for phantom 18. In the uncorrected image (a), the artifacts due to the tNLPV effect are slightly masked by the aliasing artifacts. With algorithm 1, the tNLPV streaks are partially reduced (b). Algorithms 2 and 3 not only offer the best reduction of the tNLPV artifacts, but they also show a strong reduction of the aliasing artifacts (c-d). These results still show some remaining streaks, despite the large number of iterations. This indicates that, even without

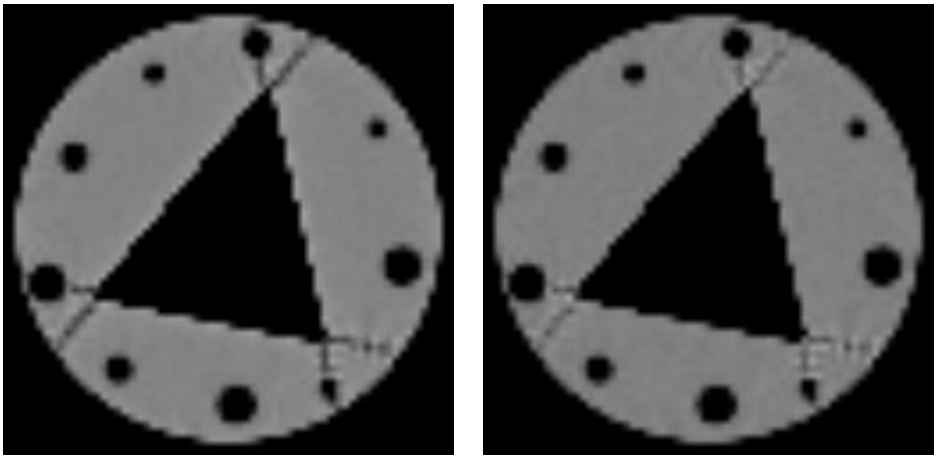

(a) (b)

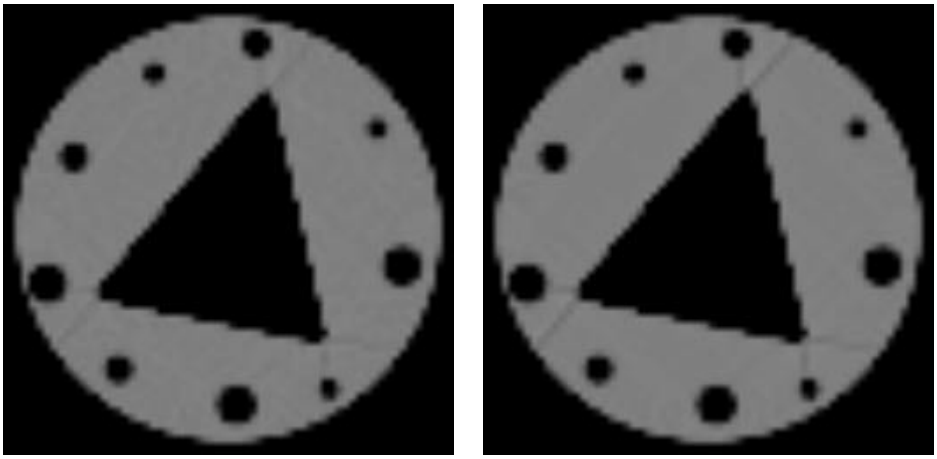

(c) (d)

Figure 5.22: *Results for phantom 17 windowed in interval μ = [0.4874 ; 0.5074] cm^{-1}: (a) FBP, (b-d) algorithms 1 to 3.*

noise, beam hardening and scatter, the inclusion of prior information (like in section 5.2) will be required for a complete reduction of metal artifacts. The minimum, mean and maximum value of the ROI drawn in figure 5.19 (e) was calculated for all algorithms. Table 5.4 shows the normalized values. The results confirm that the three proposed algorithms result in a substantial artifact reduction.

Figure 5.24 shows the results for phantom 19: (a) the reconstruction with algorithm 3 and (b) the subtraction of the reconstruction with algorithm 3 from the FBP reconstruction. The difference image shows that the NLPV is strongly reduced. Still, the NLPV effect is not entirely eliminated. Improved modeling of the detector cross-talk and other geometrical factors, in combination with some prior

phantom 17	min	mean	max
FBP -	-2.6890	0.1920	2.6540
FBP +	-6.7550	-1.6420	1.9780
alg 1	-5.0760	-0.5570	2.9280
alg 2	-0.0880	0.3970	1.4240
alg 3	-0.7270	0.2050	1.3120

Table 5.3: *Normalized values of the ROI drawn in figure 5.19 (c), for the FBP reconstruction without (FBP -) and with tNLPV effect (FBP +), and the results of algorithms 1, 2, and 3.*

phantom 18	min	mean	max
FBP -	-6.3270	-1.3220	2.2900
FBP +	-13.2390	-2.2720	17.6420
alg 1	-5.8780	-1.6890	5.1860
alg 2	-1.3060	-0.0380	2.5360
alg 3	-1.0950	-0.0250	2.9730

Table 5.4: *Normalized values of the ROI drawn in figure 5.19 (e), for the FBP reconstruction without (FBP -) and with tNLPV effect (FBP +), and the results of algorithms 1, 2, and 3.*

information, may improve these very preliminary results.

Although algorithms 2 and 3 are clearly superior to algorithm 1 with regard to artifact reduction, a strong reduction of computation time is required before they can be used routinely. Algorithm 1 offers only partial artifact correction, but has the advantage that it can be used as a pre-processing step in combination with any existing reconstruction algorithm. Finally, so far we have assumed that all beam samples have equal weights. In particular, the focal spot is modeled as a uniformly radiating straight line, and the detection sensitivity is independent of the beam sample. However, both the simulations and the correction algorithms could easily be made more realistic, for instance by using a Gaussian-shaped emission profile.

5.4.5 Conclusion for *t*NLPV correction

Three algorithms for correction of the *t*NLPV effect are presented. The algorithms were applied to simulations. Until now, only algorithm 3 was applied to a measurement. Algorithm 1 allows a substantial reduction of the *t*NLPV artifacts, and consists of a pre-correction step applied directly to the measured sinogram. Algorithms 2 and 3 give the best results at the expense of high computation time. In the presence of metal objects, the *t*NLPV artifacts are accompanied by relatively strong aliasing artifacts. In this case, algorithms 2 and 3 are clearly superior to algorithm 1. Still, we expect that inclusion of prior information is required for

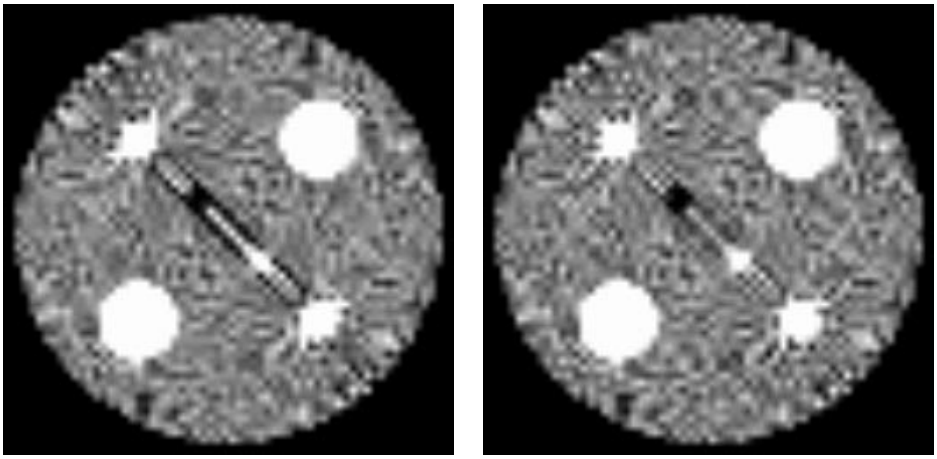

(a) (b)

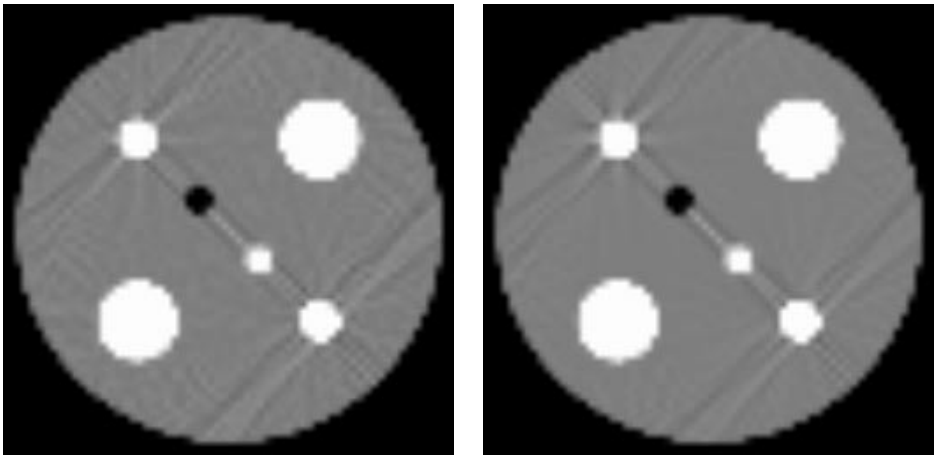

(c) (d)

Figure 5.23: *Results for phantom 18 windowed in interval μ = [0.1846 ; 0.2046] cm^{-1}: (a) FBP, (b-d) algorithms 1 to 3.*

complete metal artifact reduction. Appropriate use of prior information may also decrease the computation time of the iterative algorithms.

5.5 Conclusion

In this chapter we have addressed three out of four important causes of metal artifacts, as determined in chapter 3. In section 5.2 we showed that effective reduction of metal artifacts is obtained by taking into account the Poisson noise characteristics of the measurement, combined with a prior and increased resolution. In section 5.3

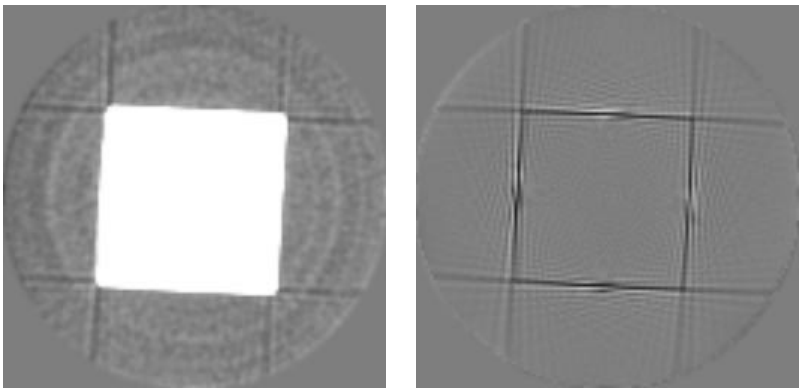

(a) (b)

Figure 5.24: *Results for phantom 19 windowed in interval μ = [-0.01 ; 0.01] cm^{-1}: (a) reconstruction with algorithm 3 and (b) subtraction of the reconstruction with algorithm 3 from the FBP reconstruction.*

the polychromatic nature of the measurements is taken into account resulting in excellent beam hardening correction. In section 5.4 a strong reduction of the trans-axial NLPV artifact is obtained, by incorporating the finite beam width and the finite rotation interval in the acquisition model.

More research is required to implement methods for scatter estimation. Also, all algorithms must be validated on clinical examples. To set the seal on this work, the different correction approaches must be combined and the most appropriate prior must be determined. A combined acquisition model, modeling both noise, beam hardening, the NLPV effect, and scatter, is given by

$$\hat{y}_i = \sum_{s=1}^{S} \sum_{k=1}^{K} b_{isk} \cdot \exp\Big(- \sum_{j=1}^{J} l_{ijs} \big[\phi(\mu_j) \cdot \Phi_k + \theta(\mu_j) \cdot \Theta_k \big] \Big) + S_i. \tag{5.25}$$

Following the same derivation as in section 4.3 and including a prior, the following update formula is obtained

$$\mu_j^{n+1} = \mu_j^n + \frac{\phi_j' \cdot \sum_{i=1}^{I} \sum_{s=1}^{S} l_{ijs} e_i Y_{is}^{\Phi} + \theta_j' \cdot \sum_{i=1}^{I} \sum_{s=1}^{S} l_{ijs} e_i Y_{is}^{\Theta} + P}{\phi_j' \cdot \sum_{i=1}^{I} \sum_{s=1}^{S} l_{ijs} M_{is} + \theta_j' \cdot \sum_{i=1}^{I} \sum_{s=1}^{S} l_{ijs} N_{is}}, \tag{5.26}$$

where

$$\phi_j' = \big(\frac{\partial \phi}{\partial \mu}\big)\big|_{\mu_j^n}$$

$$\theta_j' = \big(\frac{\partial \theta}{\partial \mu}\big)\big|_{\mu_j^n}$$

$$e_i = 1 - \frac{y_i}{\hat{y}_i}$$

$$P = \beta \sum_{h=1}^{J} \frac{\partial V}{\partial \mu}(\mu_h - \mu_j)$$

$$\begin{aligned} M_{is} = &\big(\sum_{h=1}^{J} l_{ih}\phi'_h\big) \cdot \big(Y_{is}^{\Phi\Phi} \cdot e_i + \frac{y_i \cdot Y_{is}^{\Phi} \cdot Y_i^{\Phi}}{\hat{y}_i^2}\big) \\ &+ \big(\sum_{h=1}^{J} l_{ih}\theta'_h\big) \cdot \big(Y_{is}^{\Phi\Theta} \cdot e_i + \frac{y_i \cdot Y_{is}^{\Phi} \cdot Y_i^{\Theta}}{\hat{y}_i^2}\big) \end{aligned}$$

$$\begin{aligned} N_{is} = &\big(\sum_{h=1}^{J} l_{ih}\phi'_h\big) \cdot \big(Y_{is}^{\Phi\Theta} \cdot e_i + \frac{y_i \cdot Y_{is}^{\Theta} \cdot Y_i^{\Phi}}{\hat{y}_i^2}\big) \\ &+ \big(\sum_{h=1}^{J} l_{ih}\theta'_h\big) \cdot \big(Y_{is}^{\Theta\Theta} \cdot e_i + \frac{y_i \cdot Y_{is}^{\Theta} \cdot Y_i^{\Theta}}{\hat{y}_i^2}\big) \end{aligned}$$

$$Y_{is}^{\Phi} = \sum_{k=1}^{K} \Phi_k \cdot \hat{y}_{isk}$$

$$Y_{is}^{\Theta} = \sum_{k=1}^{K} \Theta_k \cdot \hat{y}_{isk}$$

$$Y_i^{\Phi} = \sum_{s=1}^{S} Y_{is}^{\Phi}$$

$$Y_i^{\Theta} = \sum_{s=1}^{S} Y_{is}^{\Theta}$$

$$Y_{is}^{\Phi\Phi} = \sum_{k=1}^{K} \Phi_k \cdot \Phi_k \cdot \hat{y}_{isk}$$

$$Y_{is}^{\Phi\Theta} = \sum_{k=1}^{K} \Phi_k \cdot \Theta_k \cdot \hat{y}_{isk}$$

$$Y_{is}^{\Theta\Theta} = \sum_{k=1}^{K} \Theta_k \cdot \Theta_k \cdot \hat{y}_{isk}$$

$$\hat{y}_{isk} = b_{isk} \cdot \exp\Big(- \Phi_k \sum_{j=1}^{J} l_{ijs} \cdot \phi(\mu_j^n) - \Theta_k \sum_{j=1}^{J} l_{ijs} \cdot \theta(\mu_j^n)\Big),$$

Intermediate results are given in appendix A.6. At the points of inflection, ϕ'_j and θ'_j are defined as

$$\begin{aligned} \phi'_j &= \frac{1}{2} \lim_{\epsilon \to 0} \big[(\frac{\partial \phi}{\partial \mu})\big|_{\mu_j^n - \epsilon} + (\frac{\partial \phi}{\partial \mu})\big|_{\mu_j^n + \epsilon} \big] \\ \theta'_j &= \frac{1}{2} \lim_{\epsilon \to 0} \big[(\frac{\partial \theta}{\partial \mu})\big|_{\mu_j^n - \epsilon} + (\frac{\partial \theta}{\partial \mu})\big|_{\mu_j^n + \epsilon} \big]. \end{aligned} \tag{5.27}$$

Finally, the result must be convolved with a Gaussian smoothing kernel with standard deviation σ to suppress Gibbs overshoots at sharp edges [140]. All MLTR algorithms presented in the previous sections are special cases of this global approach:

- The MAP algorithm from section 5.2 is obtained by choosing $K = 1$, $S = 1$, and $S_i \equiv 0$.
- IMPACT from section 5.3 is obtained by choosing $\beta = 0$, $S = 1$, and $S_i \equiv 0$.
- The tNLPV algorithm from section 5.4.1.3 is obtained by choosing $K = 1$, $\beta = 0$, and $S_i \equiv 0$.
- Finally, the scatter algorithm from section 4.5 is obtained by choosing $K = 1$, $\beta = 0$, and $S = 0$.

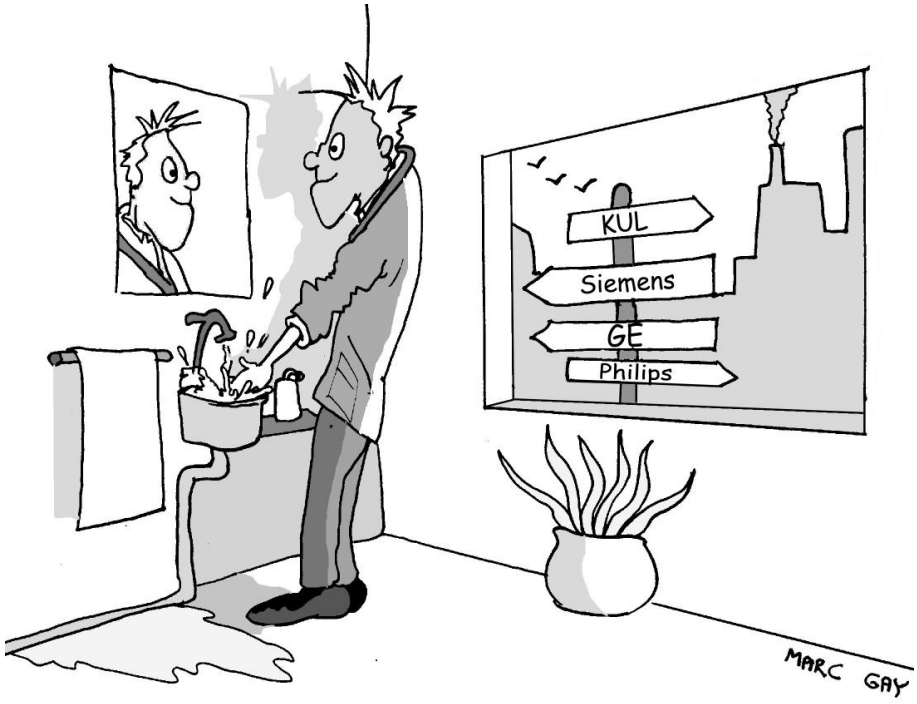
KUL
Siemens
GE
Philips
MARC GAY

Chapter 6

General conclusions

6.1 Main contributions

In this thesis we have tried to contribute to the field of metal artifact reduction in computed tomography

- by performing a profound investigation of metal artifacts and their origin,
- and by investigating the potential application of iterative reconstruction for reduction of metal artifacts.

Our attention to metal artifacts was drawn in an explorative study on the use of iterative reconstruction for spiral CT [109]. We decided to tackle the problem of metal artifacts in a fundamental way. First of all, we needed to know the origin of metal artifacts. Many causes of (non-metal) artifacts are found in the literature. In order to determine which of those causes are most important for metal artifacts, a thorough analysis of the acquisition and reconstruction in CT was required, including simulations and measurements.

We developed a high-resolution 2D CT-simulator [24], taking into account the finite X-ray beam width, the continuous rotation of the scanner, and a realistic X-ray spectrum. The simulator has proven to be very realistic. It allowed us to estimate a number of technological parameters such as afterglow and detector cross-talk. The simulator has two major limitations: it is limited to 2D, and it does not include accurate scatter simulation. Although we concentrated on simulating the Siemens Somatom Plus 4 CT-scanner, the simulator is applicable to any fan-beam CT-scanner, including micro-CT-scanners.

In order to analyze measurements on a real CT-scanner, we had to figure out how to transfer and decode raw data and images from a CT-scanner. We concentrated on the Siemens Somatom Plus 4 CT-scanner, as this was the newest available CT-scanner at the moment, and because Siemens was willing to provide us with the necessary information. A number of existing reconstruction algorithms (FBP, ML-EM, ML-TR, IBHC, ...) were implemented and – where necessary – adapted to

a fan-beam geometry. This included writing a rebinner, as well as a fan-beam projector-backprojector.

Simulations and measurements allowed us to understand the origin of the different types of artifacts. The most important causes of metal artifacts were found to be noise, beam hardening, the NLPV effect, and scatter [24]. In the absence of metal objects, all these effects still result in artifacts, but to a lesser extent. Consequently, all algorithms designed to correct one of the causes of metal artifacts have potentially a much broader range of application.

In a second part of this work, we have tried to develop algorithms for correcting the different causes of metal artifacts. More in particular we have investigated the use of iterative reconstruction for reduction of metal artifacts. We hypothesized that using a more accurate acquisition model would result in reduced artifacts. We based ourselves on the ML-TR algorithm [110], which uses a Poisson noise model.

1. We developed a MAP method [25]. By using a Poisson noise model, we try to minimize the artifacts that are due to noise. This noise model also makes the algorithm more robust against other sources of artifacts. We used a Markov random field prior to take incorporate a-priori knowledge. And we applied increased sampling in the reconstructed image to increase the number of degrees of freedom. Good results were obtained for simulations and phantom measurements. Streak artifacts were reduced while small line-shaped details were preserved. The MAP algorithm was compared with the projection completion method, and with iterative reconstruction ignoring the projections through metal objects.

2. We extended the acquisition model to take into account the polychromatic nature of CT, for reduction of beam hardening artifacts [26]. This resulted in a new iterative maximum likelihood polychromatic algorithm for CT (IMPACT). Excellent results were obtained on simulations and phantom measurements. The algorithm was compared to the post-reconstruction approach, and the degree of beam hardening correction was comparable for both algorithms. In the presence of metal objects, IMPACT performed clearly better, thanks to the accurate noise model.

3. Three algorithms were developed for reduction of the NLPV effect [27], taking into account both the finite rotation intervals and the actual size of the focal spot and the detector elements. The first method consists of a pre-correction step applied directly to the measured sinogram, combined for instance with FBP. The two other methods are adaptations of ML-TR, modeling the finite beam width and the finite rotation intervals. Good results were obtained for simulations and for a measurement. All three methods result in substantial artifact reduction. In the presence of metal objects, the iterative algorithms were clearly superior.

4. Finally, we derived a global algorithm taking into account all causes of metal artifacts. All proposed correction algorithms can be derived from it as special cases.

6.2 Suggestions for future work

6.2.1 Scatter

From the four most important causes of metal artifacts determined in chapter 3, three have been addressed in chapter 5: noise, beam hardening, and the NLPV effect. Scatter, the fourth important cause, requires further research. Iterative algorithms taking into account scatter - like presented in section 4.5 - require an estimate of the scatter contribution. We now give an overview of existing scatter models, we propose a new scatter simulator, and we suggest a framework for reduction of scatter artifacts.

In [43], it is shown that the scatter contribution can be well approximated by a constant, i.e. independent of detector element or view number. This is justified by recognizing that the scatter profiles are relatively smooth compared to the total measured intensity profiles. Also in [43], an analytic formulation of the scatter is presented, yet limited to cylindrical phantoms.

A slightly more complicated scatter model is derived in [49] and improved in [115]. In [49], it is shown that scatter can be modeled as

$$S_i \sim \mathcal{S}(I_i \cdot p_i), \tag{6.1}$$

where I_i and p_i are the detected intensity and attenuation respectively in sinogram pixel i, and $\mathcal{S}$ represents a smoothing operation where all sinogram rows are convolved with a rectangular or trapezoidal kernel.

Even more reliable scatter estimates are obtained by Monte Carlo simulation [16, 17, 86, 93]. A main drawback here is the high computation time.

We propose a simple scatter simulator in appendix A.7. It is more accurate than the model proposed by [49] and [115], in the sense that it takes into account the actual scatterer distribution. Consequently, we expect that the resulting scatter profiles will be a better approximation than with the simpler methods. It is too simple, in the sense that it does not take into account the energy-dependence of the scatter fraction and of the scatter angle, and it is limited to 2D. This scatter simulator will have to be validated using measurements and/or Monte Carlo simulations. It can then be combined with the CT-simulator to provide a more realistic scatter simulation. For reduction of scatter we propose to use the method presented in section 4.5 and included in the global approach (section 5.5). For estimation of the scatter contribution, the proposed scatter simulator can be used. This leads to the following procedure:

1. perform a number of iterations without scatter correction or with a simplified scatter estimation,
2. estimate the scatter contribution using the scatter simulator and based on the intermediate reconstruction,
3. perform a number of iterations with scatter correction, and if necessary repeat step 2.

6.2.2 Extension to 3D

Most work presented in this thesis is limited to 2D. In real CT-scanners, the third dimension can not be neglected:

1. The third dimension forms the basis of the axial NLPV effect (section 3.4.3.4). The axial NLPV effect is essentially very similar to the tNLPV effect. Correction of the axial NLPV effect requires a 3D approach, resulting in much larger computation times. But the axial NLPV effect can also be limited (although not eliminated) by using narrower slice collimation, avoiding the requirement of a 3D approach.

2. In spiral CT, as the patient shifts through the gantry, the X-ray tube follows a helical orbit with respect to the patient. This 3D situation is reduced to a 2D reconstruction problem using interpolation (see section 2.6), at the expense of longitudinal smoothing and spiral artifacts. The spiral CT study in section 4.9 indicated that iterative reconstruction might offer a solution for these problems using non-linear constraints. However, with the advent of multi-slice CT, longitudinal sampling and resolution are no longer a problem, and a 3D approach is no longer necessary provided that the cone angle is small enough.

3. CT-scanner technology is steadily evolving, and within a few years full cone-beam scanners will probably be commercially available. A lot of research is being done in cone-beam reconstruction. Here also, 3D iterative reconstruction is an option to consider.

The previous arguments allow to conclude that 3D iterative reconstruction might be useful but is not necessary. In both cases, all work presented in this thesis remains valid. Noise, beam hardening, the NLPV effect, and scatter are inherent physical phenomena and apply to all types of CT-scanners. If the 3D acquisition is reduced to a number of 2D reconstruction problems, the presented correction algorithms can be applied directly. If 3D reconstruction is required, the presented correction algorithms can be extended to 3D.

6.2.3 Global approach

Once the work on scatter estimation is completed, the global approach can be implemented. One aspect that will need further investigation is the choice of prior parameters (prior type, prior weight, ...) that give the best reconstructions. For application in clinical routine, a strong reduction of the computational cost of the proposed algorithms will be required. We have focussed on a fundamental solution to the problem, rather than worrying about computation times. All reconstruction algorithms presented in this thesis are essentially adaptations of the objective function (see chapter 4), and we have not tried to improve the optimization strategy. We are convinced that improved optimization techniques, additional acceleration

tricks, more efficient programming, faster computers and hardware implementation will bring maximum likelihood iterative reconstruction in CT within reach. Our hope and expectation is that the proposed global approach will allow reduction of metal artifacts far beyond the point that is possible today.

Appendix A

Proofs and derivations

A.1 Proof of the projection theorem

By definition, the 2D FT of $f(x, y)$ is:

$$F(k_x, k_y) = \int_{-\infty}^{\infty} \int_{-\infty}^{\infty} f(x, y)\ e^{-2\pi i(k_x x + k_y y)}\ dx\ dy.$$

Using eq.(2.22) this becomes

$$F(k_x, k_y) = \int_{-\infty}^{\infty} \int_{-\infty}^{\infty} f(x, y)\ e^{-2\pi i(k \cdot \cos\theta \cdot x + k \cdot \sin\theta \cdot y)}\ dx\ dy.$$

Using transformation formulas (2.8) and (2.9), the integration variables x and y can be substituted by r and s:

$$F(k_x, k_y) = \int_{-\infty}^{\infty} \int_{-\infty}^{\infty} f(r \cdot \cos\theta - s \cdot \sin\theta, s \cdot \cos\theta + r \cdot \sin\theta) \cdot e^{-2\pi i(k \cdot \cos\theta(r \cdot \cos\theta - s \cdot \sin\theta) + k \cdot \sin\theta(s \cdot \cos\theta + r \cdot \sin\theta))}\ ds\ dr.$$

Since $\cos^2\theta + \sin^2\theta = 1$ this reduces to:

$$F(k_x, k_y) = \int_{-\infty}^{\infty} \int_{-\infty}^{\infty} f(r \cdot \cos\theta - s \cdot \sin\theta, s \cdot \cos\theta + r \cdot \sin\theta)\ e^{-2\pi i(k \cdot r)}\ ds\ dr.$$

$e^{-2\pi i(k \cdot r)}$ is independent of s and can be placed outside the inner integral:

$$F(k_x, k_y) = \int_{-\infty}^{\infty} e^{-2\pi i(k \cdot r)} \Big[\int_{-\infty}^{\infty} f(r \cdot \cos\theta - s \cdot \sin\theta, s \cdot \cos\theta + r \cdot \sin\theta)\ ds \Big]\ dr.$$

From eq.(2.13) it is clear that the inner integral is the projection $p(r,\theta)$:

$$F(k_x,k_y)=\int_{-\infty}^{\infty} p(r,\theta)\ e^{-2\pi i(k\cdot r)}\ dr.$$

By definition the right hand side is the 1D FT of $P(k,\theta)$:

$$F(k_x,k_y)=P(k,\theta).$$

A.2 Derivation of fan-beam FBP

Substituting eq.(2.30) in eq.(2.27) and limiting r in the integration to [-FOV/2 ; FOV/2] yields

$$f(x,y)=\frac{1}{2}\int_0^{2\pi}\int_{-\mathrm{FOV}/2}^{+\mathrm{FOV}/2} p(r,\theta)\ q(x\cos\theta+y\sin\theta-r)\ dr\ d\theta. \tag{A.1}$$

The factor 1/2 compensates the modification of the integration limits from 0 to 2π. The transformation formulas 2.36 allow to switch to the fan-beam coordinates (α,β). The Jacobian of this transformation is

$$J=\begin{vmatrix} 1 & 1 \\ 0 & R\cos\alpha \end{vmatrix}=R\cos\alpha.$$

Because α is always in the interval $[-\pi/2,\pi/2]$, $|R\cos\alpha|=R\cos\alpha$. Introducing these new coordinates in eq.(A.1) yields

$$\begin{aligned} f(x,y)=\frac{1}{2}\int_0^{2\pi}\int_{-\frac{\Delta\alpha}{2}}^{+\frac{\Delta\alpha}{2}} \Big(&p(\alpha,\beta)\ q(x\cos(\alpha+\beta)+y\sin(\alpha+\beta)-R\sin\alpha) \\ &\cdot R\cdot\cos\alpha\ d\alpha\ d\beta\Big). \end{aligned} \tag{A.2}$$

Using the sum-equations

$$\begin{cases} \cos(\alpha+\beta) &= \cos\alpha\cos\beta-\sin\alpha\sin\beta \quad \text{(a)} \\ \sin(\alpha+\beta) &= \sin\alpha\cos\beta+\sin\beta\cos\alpha, \quad \text{(b)} \end{cases} \tag{A.3}$$

the argument of $q(.)$ in eq.(A.2) becomes

$$\arg\{q(.)\}=\cos\alpha\cdot[x\cos\beta+y\sin\beta]+\sin\alpha\cdot[-x\sin\beta+y\cos\beta-R]. \tag{A.4}$$

This equation looks very much like eq.(A.3) (b). Therefore, we define

$$\begin{cases} v\sin\gamma &= x\cos\beta+y\sin\beta \quad \text{(a)} \\ v\cos\gamma &= x\sin\beta-y\cos\beta+R. \quad \text{(b)} \end{cases} \tag{A.5}$$

We can then calculate γ and v as

$$\gamma = \arctan(\frac{(A.5\ a)}{(A.5\ b)}) = \arctan(\frac{x\cos\beta + y\sin\beta}{x\sin\beta - y\cos\beta + R})$$

$$v = \sqrt{(A.5\ a)^2 + (A.5\ b)^2} = \sqrt{(x\cos\beta + y\sin\beta)^2 + (x\sin\beta - y\cos\beta + R)^2}.$$

It can be seen that v represents the distance from the image point (x, y) to the top of the fan and γ is the value of α for the projection line through the image point (x, y). Substituting eq.(A.5) in eq.(A.4) yields

$$\begin{aligned}\arg\{q(.)\} &= v \cdot (\cos\alpha \cdot \sin\gamma - \sin\alpha \cdot \cos\gamma) \\ &= v \cdot \sin(\gamma - \alpha).\end{aligned}$$

Equation (A.2) then becomes

$$f(x,y) = \frac{1}{2}\int_0^{2\pi}\int_{-\frac{\Delta\alpha}{2}}^{+\frac{\Delta\alpha}{2}} p(\alpha,\beta)\ q(v\sin(\gamma-\alpha))\ R\cos\alpha\ d\alpha\ d\beta. \tag{A.6}$$

From eq.(2.31) we find

$$q(v\sin(\gamma-\alpha)) = \int_{-\infty}^{+\infty} |k|\ e^{i2\pi k v\sin(\gamma-\alpha)}\ dk. \tag{A.7}$$

If we define a new variable k' given by

$$\begin{aligned}k' &= k \cdot \frac{v\sin(\gamma-\alpha)}{\gamma-\alpha} \\ k &= k' \cdot \frac{\gamma-\alpha}{v\sin(\gamma-\alpha)} \\ dk &= dk' \cdot \frac{\gamma-\alpha}{v\sin(\gamma-\alpha)}\end{aligned}$$

and if we substitute it in eq.(A.7), we have

$$q(v\sin(\gamma-\alpha)) = \int_{-\infty}^{+\infty} |k'|\left(\frac{\gamma-\alpha}{v\sin(\gamma-\alpha)}\right)^2 e^{i2\pi k'(\gamma-\alpha)}\ dk'.$$

Finally, we have the following fan-beam reconstruction formula from eq.(A.6)

$$\begin{aligned}f(x,y) &= \frac{1}{2}\int_0^{2\pi}\frac{1}{v^2}\int_{-\frac{\Delta\alpha}{2}}^{+\frac{\Delta\alpha}{2}} [R\cos\alpha\ p(\alpha,\beta)](\frac{\gamma-\alpha}{\sin(\gamma-\alpha)})^2\ q(\gamma-\alpha)\ d\alpha\ d\beta \\ &= \int_0^{2\pi} W_1(x,y,\beta)\int_{-\frac{\Delta\alpha}{2}}^{+\frac{\Delta\alpha}{2}} [W_2(\alpha)\ p(\alpha,\beta)]\ g(\gamma-\alpha)\ d\alpha\ d\beta,\end{aligned}$$

where

$$W_1(x, y, \beta) = \frac{1}{v^2}$$

$$W_2(\alpha) = \frac{1}{2} R \cos\alpha$$

$$g(\alpha) = \left(\frac{\alpha}{\sin\alpha}\right)^2 \cdot q(\alpha).$$

A.3 Mathematical demonstration of the NLPV effect

The following derivation is adapted from [75]. The left side of eq.(3.9) can be written as:

$$\begin{aligned} -\ln\frac{\bar{I}}{I_0} &= -\ln\frac{\iint_R I_0 \cdot \exp(-p(\vec{r})) \cdot d\vec{r}}{I_0 \cdot \iint_R d\vec{r}} \\ &= -\ln\frac{\iint_R \exp(-\bar{p} - \Delta p(\vec{r})) \cdot d\vec{r}}{\iint_R d\vec{r}}, \end{aligned}$$

where

$$\Delta p(\vec{r}) = p(\vec{r}) - \bar{p}.$$

The term $\bar{p}$ is a constant and can be brought outside the logarithm:

$$\begin{aligned} & -\ln\frac{\bar{I}}{I_0} \\ &= \bar{p} - \ln\frac{\iint_R \exp(-\Delta p(\vec{r})) \cdot d\vec{r}}{\iint_R d\vec{r}} \\ &= \bar{p} - \ln\frac{\iint_R \left(1 - \Delta p(\vec{r}) + F(\Delta p(\vec{r}))\right) \cdot d\vec{r}}{\iint_R d\vec{r}}, \end{aligned}$$

where

$$F(x) = \exp(x) - 1 - x.$$

As the average of $\Delta p(\vec{r})$ is zero, we have

$$\begin{aligned} & -\ln\frac{\bar{I}}{I_0} \\ &= \bar{p} - \ln\left(1 - \frac{\iint_R F(\Delta p(\vec{r})) \cdot d\vec{r}}{\iint_R d\vec{r}}\right). \end{aligned}$$

Because $F(x) > 0$ if $x \neq 0$ and because

$$\text{sign}(\ln(1+x)) \;=\; \text{sign}(x),$$

we have

$$-\ln\frac{\bar{I}}{I_0} < \bar{p}$$

if $\Delta p(\vec{r})) \neq 0$ for at least some $\vec{r}$.

A.4 Derivation of IMPACT

From eq.(5.14) it follows that

$$\frac{\partial \hat{y}_i}{\partial \mu_j} = -l_{ij}\big(\phi'_j Y_i^{\Phi} + \theta'_j Y_i^{\Theta}\big),$$

and assuming $\phi''_j \equiv 0$ and $\theta''_j \equiv 0$ we have

$$\frac{\partial^2 \hat{y}_i}{\partial \mu_j \partial \mu_h} = -l_{ij} l_{ih}\big(\phi'_j \phi'_h Y_i^{\Phi\Phi} + \phi_j \theta'_h Y_i^{\Phi\Theta} + \theta_j \phi'_h Y_i^{\Phi\Theta} + \theta'_j \theta'_h Y_i^{\Theta\Theta}\big).$$

From eq.(4.8) it follows that

$$\frac{\partial L}{\partial \mu_j} = \sum_{i=1}^{I}(e_i)(-l_{ij})\big(\phi'_j Y_i^{\Phi} + \theta'_j Y_i^{\Theta}\big)$$

and

$$\frac{\partial^2 L}{\partial \mu_j \partial \mu_h} = -\sum_{i=1}^{I}(l_{ij})(l_{ih})\Big[e_i\big(\phi'_j \phi'_h Y_i^{\Phi\Phi} + \phi_j \theta'_h Y_i^{\Phi\Theta} + \theta_j \phi'_h Y_i^{\Phi\Theta} + \theta'_j \theta'_h Y_i^{\Theta\Theta}\big) - \frac{y_i}{\hat{y}_i^2}\big(\phi'_j Y_i^{\Phi} + \theta'_j Y_i^{\Theta}\big)\big(\phi'_h Y_i^{\Phi} + \theta'_h Y_i^{\Theta}\big)\Big].$$

Substituting this in eq.(4.15) and reordering the terms results in eq.(5.15).

A.5 Derivation of NLPV algorithm 3

Taking the first derivative of eq.(5.22) gives

$$\frac{\partial \hat{y}_i}{\partial \mu_j} = \sum_{s=1}^{S} -l_{ijs}\hat{y}_{is}.$$

Taking the first derivative of eq.(4.8) gives

$$\frac{\partial L}{\partial \mu_j} = \sum_{i=1}^{I}\sum_{s=1}^{S} l_{ijs} \cdot \hat{y}_{is} \cdot (1 - \frac{y_i}{\hat{y}_i}).$$

Summing the second derivative of eq.(4.8) and approximating $\sum_{h=1}^{J} l_{ihs}$ by $\sum_{h=1}^{J} l_{ih}$, results in

$$\sum_{h=1}^{J} \frac{\partial^2 L}{\partial \mu_j \partial \mu_h} = \sum_{i=1}^{I}\sum_{s=1}^{S} l_{ijs} \cdot (\sum_{h=1}^{J} l_{ih}) \cdot \hat{y}_{is}.$$

Substituting these results in eq.(4.15) and reordering the terms results in eq.(5.23).

A.6 Derivation of a global approach

From eq.(5.25) it follows that

$$\frac{\partial \hat{y}_i}{\partial \mu_j} = -\phi_j' \cdot \big(\sum_{s=1}^{S} l_{ijs} Y_{is}^{\Phi}\big) - \theta_j' \cdot \big(\sum_{s=1}^{S} l_{ijs} Y_{is}^{\Theta}\big),$$

and assuming $\phi_j'' \equiv 0$ and $\theta_j'' \equiv 0$ we have

$$\begin{aligned}
\frac{\partial Y_{is}^{\Phi}}{\partial \mu_h} &= -l_{ihs} \cdot \Big[\phi_h' \cdot Y_{is}^{\Phi\Phi} + \theta_h' \cdot Y_{is}^{\Phi\Theta}\Big] \\
\frac{\partial Y_{is}^{\Theta}}{\partial \mu_h} &= -l_{ihs} \cdot \Big[\phi_h' \cdot Y_{is}^{\Phi\Theta} + \theta_h' \cdot Y_{is}^{\Theta\Theta}\Big]
\end{aligned}$$

From eq.(4.8) it follows that

$$\frac{\partial L}{\partial \mu_j} = \phi_j' \sum_{i=1}^{I}\sum_{s=1}^{S} l_{ijs} Y_{is}^{\Phi} e_i + \theta_j' \sum_{i=1}^{I}\sum_{s=1}^{S} l_{ijs} Y_{is}^{\Theta} e_i$$

and

$$\begin{aligned}
\frac{\partial^2 L}{\partial \mu_j \partial \mu_h} = \phi_j' \cdot \sum_{i=1}^{I}\sum_{s=1}^{S} l_{ijs} \Big[&\big(-l_{ihs}\big)\big(\phi_h' Y_{is}^{\Phi\Phi} + \theta_h' Y_{is}^{\Phi\Theta}\big) e_i \\
&+ Y_{is}^{\Phi} \frac{y_i}{\hat{y}_i^2} \Big(-\phi_h' (\sum_{s'=1}^{S} l_{ihs'} Y_{is'}^{\Phi}) - \theta_h' (\sum_{s'=1}^{S} l_{ihs'} Y_{is'}^{\Theta}) \Big) \Big] \\
+\theta_j' \cdot \sum_{i=1}^{I}\sum_{s=1}^{S} l_{ijs} \Big[&\big(-l_{ihs}\big)\big(\phi_h' Y_{is}^{\Phi\Theta} + \theta_h' Y_{is}^{\Theta\Theta}\big) e_i \\
&+ Y_{is}^{\Theta} \frac{y_i}{\hat{y}_i^2} \Big(-\phi_h' (\sum_{s'=1}^{S} l_{ihs'} Y_{is'}^{\Phi}) - \theta_h' (\sum_{s'=1}^{S} l_{ihs'} Y_{is'}^{\Theta}) \Big) \Big]
\end{aligned}$$

Substituting this in eq.(4.15), approximating $\sum_{h=1}^{J} l_{ihs}\phi_h'$ by $\sum_{h=1}^{J} l_{ih}\phi_h'$ and $\sum_{h=1}^{J} l_{ihs}\theta_h'$ by $\sum_{h=1}^{J} l_{ih}\theta_h'$, and reordering the terms results in eq.(5.26).

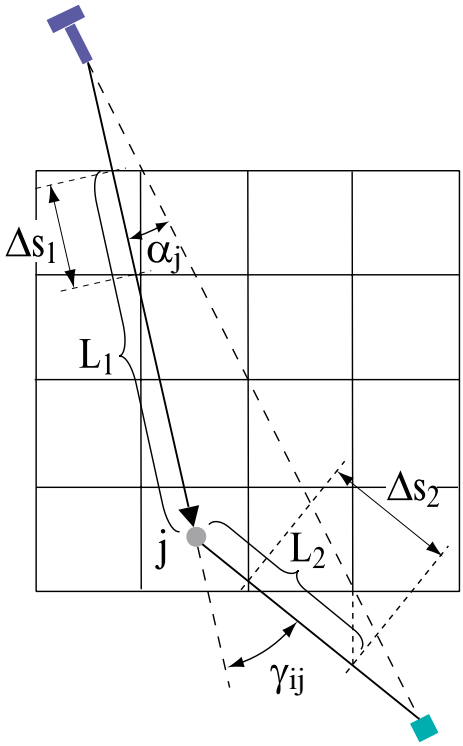

Figure A.1: Scatter simulator: for every sinogram pixel i the scatter contribution is calculated by summing the contributions over all image pixels j

A.7 Scatter simulator

The working of the scatter simulator is shown in figure A.1. For every sinogram pixel i, the scatter contribution is calculated by summing the contributions over all image pixels j. The scattered fraction depends on the scatter angle γ_{ij} and on μ_j. The scatter calculation is summarized by:

$$S_i \sim \sum_{j=1}^{J} f(\alpha_j) \cdot g(\gamma_{ij}) \cdot \mu_j \cdot \exp(-\sum_{h=1}^{J} l^1_{ijh}\mu_h) \cdot \exp(-\sum_{h=1}^{J} l^2_{ijh}\mu_h), \tag{A.8}$$

where $f(\alpha_j)$ represents the angular non-uniformity of the X-ray tube, and $g(\gamma_{ij})$ is the dependence of the scatter fraction on the scatter angle. l^1_{ijh} and l^2_{ijh} are the effective intersection lengths of lines L_1 and L_2 with pixel h, similar to l_{ij} defined in section 3.2:

$$\begin{aligned} l^1_{ijh} &= \Delta s_1 \cdot c^1_{ijh} \\ l^2_{ijh} &= \Delta s_2 \cdot c^2_{ijh}, \end{aligned} \tag{A.9}$$

where c^1_{ijh} and c^2_{ijh} are the interpolation coefficients of L_1 and L_2 with pixel h. l^1_{ijh} and l^2_{ijh} are zero at one side of pixel j (i.e. outside the intervals L_1 and L_2 in figure A.1).

Bibliography

[1] R E Alvarez and A Macovski. Energy-selective reconstructions in X-ray computerized tomography. *Phys Med Biol*, 21(5):733–744, 1976.

[2] D E Avrin, A Macovski, and L M Zatz. Clinical application of compton and photoelectric reconstruction in computed tomography: Preliminary results. *Investigative Radiology*, 13(3):217–222, May-June 1978.

[3] J Beier, R C Bittner, N Hosten, J Tröger, and R Felix. Reduktion von partialvolumenartefakten für eine verbesserte dreidimensionale visualisierung von CT-untersuchungen. *Radiologe*, 38(10):860–866, October 1998.

[4] R N Bracewell and A C Riddle. Inversion of fanbeam scans in radio astronomy. *Astrophys J*, 150:427–434, 1967.

[5] J A Brink. Technical aspects of helical (spiral) CT. *Radiologic Clinics of North America*, 33(5):825–841, September 1995.

[6] R A Brooks and G Di CHiro. Slice geometry in computer assisted tomography. *J Comput Assist Tomogr*, 1(2):191–199, 1977.

[7] R A Brooks and G di Chiro. Beam hardening in X-ray reconstructive tomography. *Phys Med Biol*, 21(3):390–398, 1976.

[8] R A Brooks, G H Glover, A J Talbert, R L Eisner, and F A DiBianca. Aliasing: A source of streaks in computed tomograms. *J Comput Assist Tomogr*, 3(4):511–518, August 1979.

[9] R A Brooks, G H Weiss, and A J Talbert. A new approach to interpolation in computed tomography. *J Comput Assist Tomogr*, 2:577–585, November 1978.

[10] J A Browne, J M Boone, and T J Holmes. Maximum-likelihood X-ray computed-tomography finite-beamwidth considerations. *Applied Optics*, 34(23):5199–5209, August 1995.

[11] J A Browne and A R De Pierro. A row-action alternative to the EM algorithm for maximizing likelihoods in emission tomography. *IEEE Trans Med Imaging*, 15(5):687–699, October 1996.

[12] B Busselen, W Bastiaens, B De Man, M Van Geet, J Nuyts, R Swennen, M Wevers, and J Carmeliet. Construction of a microfocus computer tomography (μCT) simulator for quantitative exploitation of μCT in material research. In *EUG XI Meeting, European Union of Geosciences, (Strasbourg, France, Apr.8-12, 2001)*, 2001.

[13] C L Byrne. Block-iterative methods for image reconstruction from projections. *IEEE Transactions on Image Processing*, 5(5):792–794, May 1996.

[14] C L Byrne. Convergent block-iterative algorithms for image reconstruction from inconsistent data. *IEEE Transactions on Image Processing*, 6(9):1296–1304, September 1997.

[15] C L Byrne. Accelerating the EMML algorithm and related iterative algorithms by rescaled block-iterative methods. *IEEE Transactions on Image Processing*, 7(1):100–109, January 1998.

[16] H P Chan and K Doi. Physical characteristics of scattered radiation in diagnostic radiology: Monte carlo simulation studies. *Medical Physics*, 12(2):152–165, Mar-Apr 1985.

[17] C-W Cheng, K W Taylor, and A F Holloway. The spectrum and angular distribution of x rays scattered from a water phantom. *Medical Physics*, 22(8):1235–1245, August 1995.

[18] Z H Cho, J P Jones, and M Singh. *Foundations of Medical Imaging*. John Wiley & Sons, New York, 1993.

[19] G Christ. Exact treatment of the dual-energy method in CT using polyenergetic X-ray spectra. *Phys Med Biol*, 29(12):1501–1510, 1984.

[20] A M Cormack. Representation of a function by its line integrals, with some radiological applications. *Journal of Applied Physics*, 34(9):2722–2727, September 1963.

[21] A M Cormack. Representation of a function by its line integrals, with some radiological applications. ii. *Journal of Applied Physics*, 35(10):2908–2913, October 1964.

[22] C R Crawford and A C Kak. Aliasing artifacts in computerized tomography. *Applied Optics*, 18(21):3704–3711, November 1979.

[23] C R Crawford and K F King. Computed tomography scanning with simultaneous patient translation. *Medical Physics*, 17(6):967–982, 1990.

[24] B De Man, J Nuyts, P Dupont, G Marchal, and P Suetens. Metal streak artifacts in X-ray computed tomography : a simulation study. *IEEE Trans Nucl Sci*, 46(3):691–696, 1999.

[25] B De Man, J Nuyts, P Dupont, G Marchal, and P Suetens. Reduction of metal streak artifacts in X-ray computed tomography using a transmission maximum a posteriori algorithm. *IEEE Trans Nucl Sci*, 47(3):977–981, 2000.

[26] B De Man, J Nuyts, P Dupont, G Marchal, and P Suetens. Iterative maximum-likelihood polychromatic algorithm for CT. *IEEE Trans Med Imaging*, (revision submitted).

[27] B De Man, J Nuyts, P Dupont, G Marchal, and P Suetens. Correction of the transaxial non-linear partial volume effect in CT. *Medical Physics*, (to be submitted).

[28] A R De Pierro. On the relation between the ISRA and the EM algorithm for positron emission tomography. *IEEE Trans Med Imaging*, 12(2):328–333, June 1993.

[29] A R De Pierro. A modified expectation maximization algorithm for penalized likelihood estimation in emission tomography. *IEEE Trans Med Imaging*, 14(1):132–137, March 1995.

[30] A P Dempster, N M Laird, and D B Rubin. Maximum-likelihood from incomplete data via the EM algorithm. *J Royal Statist Soc*, 39(1):1–38, 1977.

[31] G di Chiro, R A Brooks, L Dubal, and E Chew. The apical artifact: Elevated attenuation values toward the apex of the skull. *J Comput Assist Tomogr*, 2(1):65–70, January 1978.

[32] D J Drost and A Fenster. A xenon ionization detector for digital radiography. *Medical Physics*, 9(2):224–230, Mar-Apr 1982.

[33] A J Duerinckx and A Macovski. Polychromatic streak artifacts in computed tomography images. *J Comput Assist Tomogr*, 2(4):481–487, September 1978.

[34] A J Duerinckx and A Macovski. Nonlinear polychromatic and noise artifacts in X-ray computed tomography images. *J Comput Assist Tomogr*, 3(4):519–526, August 1979.

[35] F Earnest, E C McCullough, and D A Frank. Fact or artifact: An analysis of artifact in high-resolution computed tomographic scanning of the sella. *Radiology*, 140:109–113, July 1981.

[36] H Erdogan and J Fessler. Ordered subsets algorithms for transmission tomography. *Phys Med Biol*, 44(11):2835–2851, 1999.

[37] J A Fessler. Hybrid poisson/polynomial objective functions for tomographic image reconstruction from transmission scans. *IEEE Transactions on Image Processing*, 4(10):1439–1450, October 1995.

[38] J A Fessler, E P Ficaro, N H Clinthorne, and K Lange. Grouped-coordinate ascent algorithms for penalized-likelihood transmission image reconstruction. *IEEE Trans Med Imaging*, 16(2):166–175, April 1997.

[39] T O J Fuchs. *Strahlaufhärtungskorrekturen in der Computer-Tomographie*. PhD thesis, Friedrich-Alexander Universität Erlangen-Nürnberg, 1998.

[40] M Gado and M Phelps. The peripheral zone of increased density in cranial computed tomography. *Radiology*, 117:71–74, October 1975.

[41] R R Galigekere. Techniques to alleviate the effects of view aliasing artifacts in computed tomography. *Medical Physics*, 26(6):896–904, June 1999.

[42] S Geman and D E McClure. Statistical methods for tomographic image reconstruction. *Bull Int Stat Inst*, 52(4):5–21, 1987.

[43] G H Glover. Compton scatter effects in CT reconstructions. *Medical Physics*, 9(6):860–867, November-December 1982.

[44] G H Glover and R L Eisner. Theoretical resolution of computed tomography systems. *J Comput Assist Tomogr*, 3(1):85–91, February 1979.

[45] G H Glover and N J Pelc. Nonlinear partial volume artifacts in X-ray computed tomography. *Medical Physics*, 7(3):238–248, May-June 1980.

[46] G H Glover and N J Pelc. An algorithm for the reduction of metal clip artifacts in CT reconstructions. *Medical Physics*, 8(6):799–807, November-December 1981.

[47] D J Goodenough, K E Weaver, H Costaridou, H Eerdmans, and P Huysmans. A new software correction approach to volume averaging artifacts in CT. *Computerized Radiology*, 10(2/3):87–98, 1986.

[48] H Guan and R Gordon. Computed tomography using algebraic reconstruction techniques (ARTs) with different projection access schemes: a comparison study under practical situations. *Phys Med Biol*, 41(9):1727–1743, September 1996.

[49] T N Hangartner. Correction of scatter in computed tomography images of bone. *Medical Physics*, 14(3):335–340, May-June 1987.

[50] N Haramati, R B Staron, K Mazel-Sperling, K Freeman, E L Nickoloff, C Barax, and F Feldman. CT scans through metal scanning technique versus hardware composition. *Comput Med Imaging Graph*, 18(6):429–34, Nov-Dec 1994.

[51] T Hebert and R Leahy. A bayesian reconstruction algorithm for emission tomography using a markov random field prior. In *Medical Imaging III: Image Processing*, volume 1092, pages 458–466. SPIE, 1989.

[52] A Hemmingsson, B Jung, and C Ytterbergh. Dual energy computed tomography: Simulated monoenergetic and material-selective imaging. *J Comput Assist Tomogr*, 10(3):490–499, 1986.

[53] G Henrich. A simple computational method for reducing streak artifacts in CT images. *Computerized Tomography*, 4(1):67–71, 1980.

[54] G T Herman. Correction for beam hardening in computed tomography. *Phys Med Biol*, 24(1):81–106, 1979.

[55] G T Herman. Demonstration of beam hardening correction in computed tomography of the head. *J Comput Assist Tomogr*, 3(3):373–378, June 1979.

[56] G T Herman. *Fundamentals of Medical Imaging*. Academic Press, 1980.

[57] G T Herman, A V Lakshminarayanan, and A Naparstek. Convolution reconstruction techniques for divergent beams. *Computers in Biology and Medicine*, 6:259–271, 1976.

[58] G T Herman and H-P Lung. Reconstruction from divergent beams: a comparison of algorithms with and without rebinning. In *Proceedings of the 7th New England (Northeast) Bioengineering Conference*, pages 351–354, 1979.

[59] G T Herman and S S Trivedi. A comparative study of two postreconstruction beam hardening correction methods. *IEEE Trans Med Imaging*, 2(3):128–135, September 1983.

[60] D J Heuscher and M Vembar. Reduced partial volume artifacts using spiral computed tomography and an integrating interpolator. *Medical Physics*, 26(2):276–286, February 1999.

[61] T Hinderling, P Rüegsegger, M Anliker, and C Dietschi. Computed tomography reconstruction from hollow projections: An application to in vivo evaluation of artificial hip joints. *J Comput Assist Tomogr*, 3(1):52–57, February 1979.

[62] G N Hounsfield. Computerized transverse axial scanning (tomography): Part 1. description of system. *British Journal of Radiology*, 46:1016–1022, December 1973.

[63] J Hsieh. Adaptive streak artifact reduction in computed tomography resulting from excessive X-ray photon noise. *Medical Physics*, 25(11):2139–2147, 1998.

[64] J Hsieh. Nonlinear partial volume artifact correction in helical ct. *IEEE Trans Nucl Sci*, 46(3):743–747, June 1999.

[65] Y Hsieh, G T Gullberg, G L Zeng, and R H Huesman. Image reconstruction using a generalized natural pixel basis. *IEEE Trans Nucl Sci*, 43(4):2306–2319, August 1996.

[66] H Hu. Multi-slice helical CT: Scan and reconstruction. *Medical Physics*, 26(1):5–18, January 1999.

[67] H M Hudson and R S Larkin. Accelerated image reconstruction using ordered subsets of projection data. *IEEE Trans Med Imaging*, 13(4):601–609, 1994.

[68] ICRU. Report 44: Tissue substitutes in radiation dosimetry and measurement. Technical report, International Commission on Radiation Units and Measurements, Bethesda, MD, 1989.

[69] H E Johns and J R Cunningham, editors. *The Physics of Radiology*. Charles C Thomas, 1971 edition, 1971.

[70] P M Joseph. The influence of gantry geometry on aliasing and other geometry dependent errors. *IEEE Trans Nucl Sci*, 27(3):1104–1111, June 1980.

[71] P M Joseph. An improved algorithm for reprojecting rays through pixel images. *IEEE Trans Med Imaging*, 1(3):192–196, November 1983.

[72] P M Joseph and C Ruth. A method for simultaneous correction of spectrum hardening artifacts in CT images containing both bone and iodine. *Medical Physics*, 24(10):1629–1634, October 1997.

[73] P M Joseph and R A Schulz. View sampling requirements in fan beam computed tomography. *Medical Physics*, 7(6):692–702, November-December 1980.

[74] P M Joseph and R D Spital. A method for correcting bone induced artifacts in computed tomography scanners. *J Comput Assist Tomogr*, 2(1):100–108, January 1978.

[75] P M Joseph and R D Spital. The exponential edge-gradient effect in X-ray computed tomography. *Phys Med Biol*, 26(3):473–487, 1981.

[76] P M Joseph and R D Spital. The effects of scatter in X-ray computed tomography. *Medical Physics*, 9(4):464–472, July-August 1982.

[77] P M Joseph, R D Spital, and C D Stockham. The effects of sampling on CT images. *Computerized Tomography*, 4(3):189–206, 1980.

[78] M Kachelriess, S Schaller, and W A Kalender. Advanced single-slice rebinning in cone-beam spiral CT. *Medical Physics*, 27(4):754–772, April 2000.

[79] A C Kak and M Slaney. *Principles of Computerized Tomographic Imaging*. IEEE Press, New York, 1987.

[80] W A Kalender. Technical foundations of spiral CT. *Seminars in Ultrasound, CT and MRI*, 15(2):81–89, April 1994.

[81] W A Kalender and T O J Fuchs. Principles and performance of single- and multislice spiral CT. *RSNA Categorical Course in Diagnostic Radiology Physics: CT and US Cross-sectional Imaging 2000*, pages 127–142, 2000.

[82] W A Kalender, R Hebel, and J Ebersberger. Reduction of CT artifacts caused by metallic implants. *Radiology*, 164:576–577, August 1987.

[83] W A Kalender and A Polacin. Physical performance characteristics of spiral CT scanning. *Medical Physics*, 18(5):910–915, Sep-Oct 1991.

[84] W A Kalender, W Seissler, E Klotz, and P Vock. Spiral volumetric CT with single-breath-hold technique, continuous transport, and continuous scanner rotation. *Radiology*, 176:181–183, 1990.

[85] C Kamphuis and F J Beekman. Accelerated iterative transmission CT reconstruction using an ordered subsets convex algorithm. *IEEE Trans Med Imaging*, 17(6):1101–1105, December 1999.

[86] H Kanamori, N Nakamori, K Inoue, and E Takenaka. Effects of scattered X-rays on CT images. *Phys Med Biol*, 30(3):239–249, 1985.

[87] I Kaplan. *Nuclear Physics*. Addison-Wesley, Reading, 2nd edition, 1979.

[88] G J Kemerink, H H Kruize, R J S Lamers, and J M A van Engelshoven. Density resolution in quantitative computed tomography of foam and lung. *Medical Physics*, 23(10):1697–1708, 1996.

[89] P K Kijewski and B E Bjärngard. Correction for beam hardening in computed tomography. *Medical Physics*, 5(3):209–214, May-June 1978.

[90] K Klingenbeck-Regn, S Schaller, T Flohr, B Ohnesorge, A K Kopp, and U Baum. Subsecond multi-slice computed tomography: Basis and applications. *Eur Radiol*, 31(2):110–124, 1999.

[91] E Klotz, W Kalender, R Sokiranski, and D Felsenberg. Algorithms for the reduction of CT artefacts caused by metallic implants. In *Medical Imaging IV: PACS System Design and Evaluation (Newport Beach, California, 6-9 February 1990)*, volume 1234, pages 642–650. SPIE - The International Society for Optical Engineering, 1990.

[92] K Lange and R Carson. EM reconstruction algorithms for emission and transmission tomography. *J Comput Assist Tomogr*, 8(2):306–316, 1984.

[93] C J Leliveld. *A Fast Monte Carlo Simulator for Scattering in X-ray Computerized Tomography*. PhD thesis, Technische Universiteit Delft, 1996.

[94] R M Lewitt. Reconstruction algorithms: Transform methods. *Proceedings of the IEEE*, 71(3):390–408, March 1983.

[95] R M Lewitt. Alternatives to voxels for image representation in iterative reconstruction algorithms. *Phys Med Biol*, 37(3), 1992.

[96] R M Lewitt and R H T Bates. Image reconstruction from projections: Iii: Projection completion methods (theory). *Optik*, 50(3):189–204, 1978.

[97] J Llacer and E Veklerov. The maximum likelihood estimator method of image reconstruction: its fundamental characteristics and their origin. In *Information Processing in Medical Imaging (Utrecht, 1987)*, pages 201–215, 1988.

[98] C H McCollough and F E Zink. Performance evaluation of a multi-slice CT system. *Medical Physics*, 26(11):2223–2230, November 1999.

[99] W D McDavid, R G Waggener, W H Payne, and M J Denis. Correction for spectral artifacts in cross-sectional reconstruction from X-rays. *Medical Physics*, 4(1):54–57, 1977.

[100] J M Meagher, C D Mote, and H B Skinner. CT image correction for beam hardening using simulated projection data. *IEEE Trans Nucl Sci*, 37(4):1520–1524, August 1990.

[101] B P Medoff, W R Brody, M Nassi, and A Macovski. Iterative convolution backprojection algorithms for image reconstruction from limited data. *J Opt Society Am*, 73(11):1493–1500, November 1983.

[102] R L Morin and D E Raeside. A pattern recognition method for the removal of streaking artifact in computed tomography. *Radiology*, 141:229–233, October 1981.

[103] U Moström and C Ytterbergh. Artifacts in computed tomography of the posterior fossa: A comparative phantom study. *J Comput Assist Tomogr*, 10(4):560–566, July-August 1986.

[104] D J Mott, G Zheng, and B Eddleston. The removal of a cupping artefact from brain images produced by the EMI 7070 CT scanner. *British Journal of Radiology*, 58:873–880, September 1985.

[105] E Ü Mumcuoğlu, R Leahy, S R Cherry, and Z Zhou. Fast gradient-based methods for bayesian reconstruction of transmission and emission PET images. *IEEE Trans Med Imaging*, 13(4):687–701, December 1994.

[106] E Ü Mumcuoğlu, R M Leahy, and S R Cherry. Bayesian reconstruction of PET images: methodology and performance analysis. *Phys Med Biol*, 41(9):1777–1807, 1996.

[107] O Nalcioglu and R Y Lou. Post-reconstruction method for beam hardening in computerised tomography. *Phys Med Biol*, 24(2):330–340, 1979.

[108] T H Newton and D G Potts, editors. *Technical Aspects of Computed Tomography*. Radiology of the Skull and Brain. The C. V. Mosby Company, St Louis, 1981.

[109] J Nuyts, B De Man, P Dupont, M Defrise, P Suetens, and L Mortelmans. Iterative reconstruction for helical CT : a simulation study. *Phys Med Biol*, 43(4):729–737, April 1998.

[110] J Nuyts, P Dupont, and L Mortelmans. Iterative reconstruction of transmission sinograms with low signal to noise ratio. In *2nd IEEE Workshop CMP: can we beat the curse of dimensionality (Prague, Czech Republic, Aug.28-30, 1996)*, pages 237–248. Birkhäuser, 1997.

[111] J Nuyts, P Dupont, C Schiepers, and L Mortelmans. Efficient storage of the detection probability matrix for reconstruction in PET. *J Nucl Med*, 35:187, 1994.

[112] J Nuyts, P Dupont, S Stroobants, R Benninck, L Mortelmans, and P Suetens. Simultaneous maximum a-posteriori reconstruction of attenuation and activity distributions from emission sinograms only. *IEEE Trans Med Imaging*, 18(5):393–403, May 1999.

[113] J Nuyts, S Stroobants, P Dupont, S Vleugels, P Flamen, and L Mortelmans. A dedicated ML-algorithm for non-attenuation corrected PET whole body images. In *IEEE Nuclear science Symposium and Medical Imaging Conference (Lyon, France, Oct.15-20, 2000)*, 2001.

[114] J Nuyts, P Suetens, and L Mortelmans. Acceleration of maximum-likelihood reconstruction using frequency amplification and attenuation compensation. *IEEE Trans Med Imaging*, 12(4):643–652, December 1993.

[115] B Ohnesorge, T Flohr, and K Klingenbeck-Regn. Efficient object scatter correction algorithm for third and fourth generation CT scanners. *Eur Radiol*, 9:563–569, 1999.

[116] B Ohnesorge, T Flohr, and K Schwarz. Efficient correction for CT image artifacts caused by objects extending outside the scan field of view. *Medical Physics*, 27(1):39–46, January 2000.

[117] B E Oppenheim. Reconstruction tomography from incomplete projections. In M M Ter-Pogossian, M E Phelps, G L Brownell, J R Cox, D O Davis, and R G Evens, editors, *Reconstruction Tomography in Diagnostic Radiology and Nuclear Medicine*, pages 155–183. University Park Press, 1977.

[118] S C Pang and S Genna. Correction for X-ray polychromaticity effects on three-dimensional reconstruction. *IEEE Trans Nucl Sci*, 23(1):623–626, February 1976.

[119] T M Peters and R M Lewitt. Computed tomography with fan beam geometry. *J Comput Assist Tomogr*, 1(4):429–436, 1977.

[120] J Radon. Über die bestimmung von funktionen durch ihre integralwerte längs gewisser mannigfaltigkeiten. *Sächsischen Akademie der Wissenschaft, Leipzig, Berichte über die Verhandlugen*, 69:262–277, 1917. Translation: *IEEE Trans Med Imaging*, 5(4):170-176, December 1986.

[121] K Rajgopal, N Srinivasa, and K R Ramakrishnan. Image reconstruction from incomplete projection data: a linear prediction approach. In C T Leondes, editor, *Medical Imaging Systems Techniques and Applications Modalities*, pages 281–328. Gordon and Breach Science Publishers, 1997.

[122] P S Rao and R J Alfidi. The environmental density artifact: A beam-hardening effect in computed tomography. *Radiology*, 141:223–227, October 1981.

[123] C Riddell, B Bendriem, M Bourguignon, and J-P Kernevez. The approximate inverse and conjugate gradient: non-symmetrical algorithms for fast attenuation correction in SPECT. *Phys Med Biol*, 40(2):269–281, February 1995.

[124] D D Robertson and H K Huang. Quantitative bone measurements using X-ray computed tomography with second-order correction. *Medical Physics*, 13(4):474–479, 1986.

[125] D D Robertson, D Magid, R Poss, E K Fishman, A F Brooker, and C B Sledge. Enhanced computed tomographic techniques for the evaluation of total hip arthroplasty. *The Journal of Arthroplasty*, 4(3):271–276, September 1989.

[126] D D Robertson, P J Weiss, E K Fishman, D Magid, and P S Walker. Evaluation of CT techniques for reducing artifacts in the presence of metallic orthopedic implants. *J Comput Assist Tomogr*, 12(2):236–241, March-April 1988.

[127] D D Robertson, J Yuan, G Wang, and M W Vannier. Total hip prosthesis metal-artifact suppression using iterative deblurring reconstruction. *J Comput Assist Tomogr*, 21(2):293–298, 1997.

[128] A J Rockmore and A Macovski. A maximum likelihood approach to emission image reconstruction from projections. *IEEE Trans Nucl Sci*, 23(4):1428–1432, 1976.

[129] A J Rockmore and A Macovski. Maximum likelihood approach to transmission image-reconstruction from projections. *IEEE Trans Nucl Sci*, 24(3):1929–1935, 1977.

[130] P Rüegsegger, T Hangartner, H U Keller, and T Hinderling. Standardization of computed tomography images by means of a material-selective beam hardening correction. *J Comput Assist Tomogr*, 2(2):184–188, April 1978.

[131] E P Rührnschopf and W A Kalender. Artefacts provoqués par des volumes partiels non linéaires et des effets homogénéisateurs en tomodensitométrie. *Electromedica*, (2):96–105, 1981.

[132] C Ruth and P M Joseph. A comparison of beam-hardening artifacts in X-ray computerized tomography with gadolinium and iodine contrast agents. *Medical Physics*, 22(12):1977–1982, December 1995.

[133] K Scheffler. Tomographic imaging with nonuniform angular sampling. *J Comput Assist Tomogr*, 23(1):162–166, 1999.

[134] P Seitz and P Rüegsegger. Anchorage of femoral implants visualized by modified computed tomography. *Archives of Orthopaedic and Traumatic Surgery*, 100(4):261–266, 1982.

[135] P Seitz and P Rüegsegger. CT bone densitometry of the anchorage of artificial knee joints. *J Comput Assist Tomogr*, 9(3):621–622, 1985.

[136] L A Shepp and B F Logan. The fourier reconstruction of a head section. *IEEE Trans Nucl Sci*, 21:21–43, June 1974.

[137] L A Shepp and Y Vardi. Maximum likelihood reconstruction for emission tomography. *IEEE Trans Med Imaging*, 1(2):113–122, 1982.

[138] W T Sheridan, M R Keller, C M O'Connor, and R A Brooks. Evaluation of edge-induced streaking artifacts in CT scanners. *Medical Physics*, 7(2):108–111, 1980.

[139] D L Snyder and M I Miller. The use of sieves to stabilize images produced with the EM algorithm for emission tomography. *IEEE Trans Nucl Sci*, 32(5):3864–3872, 1985.

[140] D L Snyder, M I Miller, L J Thomas, and G Politte. Noise and edge artifacts in maximum-likelihood reconstructions for emission tomography. *IEEE Trans Med Imaging*, 6(3):228–238, 1987.

[141] H Soltanian-Zadeh, J P Windham, and J Soltanianzadeh. CT artifact correction: An image processing approach. In *Medical Imaging: Image Processing (Newport Beach, California, 12-15 February 1996)*, volume 2710, pages 477–485. SPIE - The International Society for Optical Engineering, 1996.

[142] C D Stockham. A simulation study of aliasing in computed tomography. *Radiology*, 132:721–726, September 1979.

[143] J P Stonestrom, R E Alvarez, and A Macovski. A framework for spectral artifact corrections in X-ray CT. *IEEE Trans Biomedical Engineering*, 28(2):128–141, 1981.

[144] P Suetens, B De Man, J D'hooge, F Maes, J Michiels, J Nuyts, J Van Cleynenbreugel, and K Vande Velde. *Fundamentals of Medical Imaging*. Cambridge University Press, 2001. (in press).

[145] M M Ter-Pogossian, M E Phelps, G L Brownell, J R Cox, D O Davis, and R G Evens, editors. *Reconstruction Tomography in Diagnostic Radiology and Nuclear Medicine*. University Park Press, Baltimore, 1977.

[146] H K Tuy. A post-processing algorithm to reduce metallic clip artifacts in CT images. *Eur Radiol*, 3:129–134, 1993.

[147] J A Veiga-Pires and M Kaiser. Artefacts in CT scanning. *British Journal of Radiology*, 52:156–157, 1979.

[148] G Wang, D L Snyder, J A O'Sullivan, and M W Vannier. Iterative deblurring for CT metal artifact reduction. *IEEE Trans Med Imaging*, 15(5):657–664, October 1996.

[149] G Wang and M W Vannier. Stair-step artifacts in three-dimensional helical CT: An experimental study. *Radiology*, 191:79–83, April 1994.

[150] G H Weiss, A J Talbert, and R A Brooks. The use of phantom views to reduce CT streaks due to insufficient angular sampling. *Phys Med Biol*, 27(9):1151–1162, 1982.

[151] C H Yan, R T Whalen, G S Beaupré, S Y Yen, and S Napel. Reconstruction algorithm for polychromatic CT imaging: Application to beam hardening correction. *IEEE Trans Med Imaging*, 19(1):1–11, January 2000.

[152] S W Young, H H Muller, and W H Marshall. Computed tomography: Beam hardening and environmental density artifact. *Radiology*, 148:279–283, July 1983.

[153] L M Zatz. The EMI scanner: Collimator design, polychromatic artifacts, and selective material imaging. In M M Ter-Pogossian, M E Phelps, G L Brownell, J R Cox, D O Davis, and R G Evens, editors, *Reconstruction Tomography in Diagnostic Radiology and Nuclear Medicine*, pages 245–266. University Park Press, Baltimore, 1977.

[154] L M Zatz and R E Alvarez. An inaccuracy in computed tomography: The energy dependence of CT values. *Radiology*, 124:91–97, July 1977.

List of publications

International Journal

1. **B. De Man**, J. Nuyts, P. Dupont, G. Marchal, and P. Suetens: "Correction of the Trans-axial Non-linear Partial Volume Effect in CT", *Medical Physics*, (to be submitted).

2. **B. De Man**, J. Nuyts, P. Dupont, G. Marchal, and P. Suetens: "An Iterative Maximum-likelihood Polychromatic Algorithm for CT", *IEEE Transactions on Medical Imaging*, (revision submitted).

3. **B. De Man**, J. Nuyts, P. Dupont, G. Marchal, and P. Suetens: "Reduction of metal streak artifacts in x-ray computed tomography using a transmission maximum a posteriori algorithm", *IEEE Transactions on Nuclear Science*, vol. 47, nr. 3, pp. 977-981, July 2000.

4. B. Bijnens, J. D'hooge, M. Schrooten, S. Pislaru, C. Pislaru, **B. De Man**, J. Nuyts, P. Suetens, F. Van de Werf, G. Sutherland, and M.-C. Herregods: "Are changes in Myocardial Integrated Backscatter restricted to the Ischemic Zone in acute induced ischemia? An in-vivo animal study comparing localized with widespread Ischemia", *J Am Soc Echo*, vol. 13, nr. 4, pp. 306-315, 2000.

5. **B. De Man**, J. Nuyts, P. Dupont, G. Marchal, and P. Suetens: "Metal Streak Artifacts in X-ray Computed Tomography: A Simulation Study", *IEEE Trans Nucl Sci*, vol. 46, nr. 3, pp. 691-696, July 1999.

6. J. Nuyts, **B. De Man**, P. Dupont, M. Defrise, P. Suetens, and L. Mortelmans: "Iterative reconstruction for helical CT: a simulation study", *Phys Med Biol*, vol. 43, pp. 729-737, March 1998.

7. J. D'hooge, J. Nuyts, B. Bijnens, **B. De Man**, P. Suetens, J. Thoen, M.-C. Herregods, and F. Van de Werf: "The calculation of the transient near- and farfield of a baffled piston using low sampling frequencies", *Journal of the Acoustical Society of America*, vol. 102, nr. 1, pp. 78-86, July 1997.

International Conference: Proceedings

1. **B. De Man**, J. Nuyts, P. Dupont, G. Marchal, and P. Suetens: "Reduction of metal streak artifacts in x-ray computed tomography using a transmission maximum a posteriori algorithm", Proceedings of IEEE Nuclear Science Symposium and Medical Imaging Conference 1999, Seattle, Washington, USA.
2. **B. De Man**, J. Nuyts, P. Dupont, G. Marchal, and P. Suetens: "Metal Streak Artifacts in X-ray Computed Tomography: A Simulation Study", Proceedings of IEEE Nuclear Science Symposium and Medical Imaging Conference 1998, Toronto, Ontario, Canada.
3. **B. De Man**, J. D'hooge, B. Bijnens, J. Nuyts, M.-C. Herregods, P. Suetens, F. Van de Werf: "Software Package for Echocardiographic Quantification Leuven (SPEQLE)", Proceedings of Computers in Cardiology 1996, Indianapolis, Indiana, USA.

International Abstract

1. B. Busselen, W. Bastiaens, **B. De Man**, M. Van Geet, J. Nuyts, R. Swennen, M. Wevers, J. Carmeliet: "Construction of a Microfocus Computer Tomography (μCT) Simulator for a Quantitative Exploitation of μCT in Material Research", EUG XI Meeting, European Union of Geosciences, April 8-12, 2001, Strasbourg, France.
2. J. D'hooge, J. Nuyts, B. Bijnens, **B. De Man**, M.-C. Herregods, J. Thoen, P. Suetens, and F. Van de Werf: "A method to accurately calculate reflected signals from tissues using low sampling frequencies", The 17th international conference book of abstracts of Ultrasonics International '97, July 2-4, 1997, Delft, The Netherlands.
3. J. D'hooge, J. Nuyts, B. Bijnens, **B. De Man**, M.-C. Herregods, J. Thoen, P. Suetens, F. Van de Werf: "A new method to accurately simulate ultrasonic images using low sampling frequencies", Ultrasonic Imaging 22nd symposium on Ultrasonic Imaging and Tissue Characterization, pp. 73, June 2-4, 1997, Arlington, Virginia, USA, January 1998.
4. C. Angermann, D. Noll, T. Lück, W. Freiberger, M.-C. Herregods, B. Bijnens, J. D'hooge, **B. De Man**, S. Pislaru, C. Pislaru, C. Moran, and T. Anderson: "Radiofrequency imaging in myocardial contrast echocardiography", International symposium on myocardial contrast echo - current status, pp. 15, April 17-18, 1997, München, Germany.
5. C. Angermann, D. Noll, T. Lück, W. Freiberger, M.-C. Herregods, B. Bijnens, J. D'hooge, **B. De Man**, S. Pislaru, C. Pislaru, C. Moran, G. Sutherland: "Factors influencing ultrasound contrast quality", Abstract book 2nd Thoraxcenter European symposium on ultrasound contrast imaging, pp. 36-38, January 23-24, 1997, Rotterdam, The Netherlands.

6. C. E. Angermann, D.S. Noll, M.-C. Herregods, B. Bijnens, J. D'hooge, **B. De Man**, S. Pislaru, C. Pislaru, T. Lück, C. Moran, and G.R. Sutherland: "Quantitative Kontrast-Echokardiographie nach intravenöser Gabe von BY 953: Ergebnisse mit einem neuen radiofrequenz-basierten System zur Echzeit-Daten-Akquisition und Bild-für-Bild-Analyse", Jahrestagung der deutschen Gesellschaft für Kardiologie- Herz- und Kreislaufforschung, 1997, Mannheim, Germany.

7. C. Angermann, D. Noll, M.-C. Herregods, B. Bijnens, J. D'hooge, **B. De Man**, S. Pislaru, C. Pislaru, T. Lück, R. Junge, C. Moran, T. Anderson, et al: "Repeat aortic root injections of by 963 for radiofrequency-based quantitative myocardial ultrasound contrast imaging: efficacy and safety", *Echocardiography*, vol. 14, nr. 6 part 2, pp. S97, 1997.

8. D. Noll, C. Angermann, M.-C. Herregods, B. Bijnens, J. D'hooge, **B. De Man**, S. Pislaru, C. Pislaru, T. Lück, C. Moran, T. Anderson, and G. Sutherland: "Cardiac contrast imaging with different doses of by 963: quantitative analysis with a new radiofrequency-based system", *Echocardiography*, vol. 14, nr. 6 part 2, pp. S83, 1997.

9. M.-C. Herregods, B. Bijnens, **B. De Man**, J. D'hooge, C. Pislaru, S. Pislaru, and F. Van de Werf: "Repetitive myocardial ischaemia and reperfusion can be detected by integrated backscatter", *European Heart Journal*, supplement 18, pp. 669, 1997.

10. C. Angermann, D. Noll, M.-C. Herregods, B. Bijnens, J. D'hooge, **B. De Man**, S. Pislaru, C. Pislaru, T. Lück, R. Junge, C. Moran, T. Anderson, et al: "Efficacy and safety of aortic root injections of by 963 for radio-frequency-based quantitative myocardial ultrasound contrast imaging", *European Heart Journal*, supplement 18, pp. 259, 1997.

11. C. Angermann, D. Noll, M.-C. Herregods, B. Bijnens, J. D'hooge, **B. De Man**, S. Pislaru, C. Pislaru, T. Lück, C. Moran, T. Anderson, and G. Sutherland: "A new system for radiofrequency based quantitative ultrasonic contrast imaging: effects of various doses of pervenous by 963", *European Heart Journal*, supplement 18, pp. 106, 1997.

12. J. D'hooge, M.-C. Herregods, B. Bijnens, **B. De Man**, S. Pislaru, C. Pislaru, D. Noll, T. Lück, T. Anderson, C. Moran, and G. Sutherland: "Radiofrequency data processing for use in quantitative contrast echocardiography: intercentre variability", *Circulation*, vol. 96, nr. 8, pp. 277, 1997.

Local Abstract

1. **B. De Man**, J. Nuyts, P. Dupont, G. Marchal, and P. Suetens: "Reduction of Metal Artifacts in X-ray Computed Tomography", 16th Symposium of the Belgian Hospital Physicists Association, 1-2 December 2000, Haasrode, Belgium.

2. J. Nuyts, **B. De Man**: "Iterative reconstruction from projections in emission and transmission tomography", 15th Symposium of the Belgian Hospital Physicists Association, 3-4 December 1999, Wilrijk, Belgium.

3. M.-C. Herregods, B. Bijnens, **B. De Man**, J. D'hooge, S. Pislaru, C. Pislaru, F. Van de Werf: "Detection of myocardial ischemia and reperfusion by integrated backscatter", *Acta Cardiologica Belgica*, vol. LI, nr. 6, pp. 599-600, 1996.

4. B. Bijnens, M.-C. Herregods, J. D'hooge, **B. De Man**, S. Pislaru, C. Pislaru, J. Nuyts, P. Suetens, F. Van de Werf: "Acquisition and analysis of radiofrequency echocardiographic contrast images", *Acta Cardiologica Belgica*, vol. LI, nr. 6, pp. 574, 1996.

Book chapter

1. P. Suetens, **B. De Man**, J. D'hooge, F. Maes, J. Michiels, J. Nuyts, J. Van Cleynenbreugel, and K. Vandevelde: "Fundamentals of medical imaging", chapter 5, Cambridge University Press, (in print).

Master's Thesis

1. **B. De Man** and P. De Bisschop: "Identification of Industrial Polymerization Processes", University of Leuven, Belgium, 1995.